Ref. Ares(2025)8494076 - 07/10/2025

Better Contrails Mitigation - BeCoM

D1.2

Humidity analysis and supersaturation values

Delivery Date:	30/09/2025 (M39)
Date of submission:	24/09/2025

LEAD BENEFICIARY FOR THIS DELIVERABLE			
Name:	CNRS		
Contact Person:	Philippe Keckhut		
E-mail:	Keckhut@latmos.ipsl.fr		
AUTHORS			
Participants:	CNRS		
Work Package:	WP 1		
Version:	1	Number of Pages:	

REVISION HISTORY			
VERSION	DATE	AUTHOR / REVIEWER	NOTES
1	14/03/2025	Dunya Alraddawi	Section 1,2
2	19/06/2025	Sidy Diara	Section 4
3	20/06/2025	Dunya Alraddawi	Section 3

REVIEWED AND SIGNED OFF BY			
ROLE	DATE	NAME	SIGNATURE

This project has received funding from the European Union's Horizon Europe Research and innovation program under Grant Agreement No 101056885

List of Figures

This project has received funding from the European Union's Horizon Europe Research and innovation program under Grant Agreement No 101056885

List of Tables

This project has received funding from the European Union's Horizon Europe Research and innovation program under Grant Agreement No 101056885

List of Photos

Abstract

The Deliverable D1.2 of the BeCoM project addresses key knowledge gaps in atmospheric humidity and contrail formation through complementary observational and modeling efforts. First, satellite-based humidity measurements and reanalysis products were evaluated against Raman lidar observations to quantify uncertainties at contrail-relevant altitudes.

Analysis of 11 years of coincident Aura MLS, ERA5, and lidar water vapor profiles reveals a systematic dry bias in both satellite and model datasets, with seasonal differences between wet and dry periods.

Further efforts are underway to validate ERA5 against Raman lidar measurements at midlatitudes, thereby extending the assessment to regions directly relevant for aviation traffic In addition to the tropical evaluation, with consistent results.

Building on these long-term comparisons and statistical analysis, the TRACIS intensive field campaign (12May–12June 2025) at the SIRTA observatory in the Parisian zone gathered an unprecedented multi-instrument dataset—including Raman lidar, a triple radiosounding system (Meteomodem M10, M20, Vaisala RS41) with both daytime and systematic nocturnal launches, GNSS, HATPRO, MiniSAOZ, and IR thermal imaging—all synergy to validate at real time scale advanced water vapor retrievals and characterize upper-tropospheric humidity in a region ideally located of frequent air traffic.

Finally, targeted case studies over Clermont-Ferrand combined lidar, all-sky imaging, ADS-B aircraft tracking, and ERA5 to document contrail formation and persistence under varying thermodynamic conditions. Results demonstrate that persistent contrails occur in ice-supersaturated layers (RHi > 105%) at 217–223 K, while non-persistent contrails form in drier, colder air. Contrail geometries and lifetimes were quantified, underscoring the role of ground-based remote sensing in contrail monitoring and mitigation research.

Together, these efforts advance understanding of humidity variability, measurement uncertainties, and supersaturation processes critical to contrail prediction and climate impact assessment.

This project has received funding from the European Union's Horizon Europe Research and innovation program under Grant Agreement No 101056885

Table of content

This project has received funding from the European Union's Horizon Europe
Research and innovation program under Grant Agreement No 101056885

This project has received funding from the European Union's Horizon Europe Research and innovation program under Grant Agreement No 101056885

1. Introduction

The main uncertainty in contrails forecasting is supersaturation humidity levels assimilation, which is complicated by the lack of accurate humidity data, most challenging to measure at cruise altitudes being affected by both large and small scale-dynamics as well as cloud processes. Satellite observations can provide important information about global upper tropospheric humidity, where measurements from other instruments are mostly sparse and rare; they could serve as an option in the absence of better information.

In the BeCoM project, we aim to assess the current uncertainties of satellite-based humidity measurements and operational forecast models using in-situ instruments. Our objective is to provide crucial humidity profiles at contrail-relevant altitudes to force contrails forecasting and mitigation efforts. We believe that addressing these challenges is essential for advancing our understanding of atmospheric dynamics and improving the accuracy of lidar-based water vapor measurements which present a pertinent reference to evaluate other upper tropospheric observations.

This deliverable includes three interconnected milestones of the BeCoM project, organized into three sections. **Section 2 (M6)** addresses long-term uncertainties in satellite, model-based, and radiosondes humidity datasets, assessed against Raman lidar observations. **Section 3 (M7)** builds on these results with the TRACIS intensive campaign, designed to provide high-resolution measurements and validate upper-tropospheric water vapor retrievals in a region of dense air traffic. **Section 4 (M9)** extends these efforts with targeted contrail case studies, combining ground-based and ancillary observations to directly investigate the link between humidity variability and contrail formation and persistence. Together, these three sections provide a coherent progression: from identifying uncertainties, to improving observational capabilities, to applying them in contrail research.

2. Satellites humidity observations uncertainty

2.1. Introduction

The accurate quantification of water vapor in the upper troposphere is essential for understanding, modeling and hence forecasting many atmospheric dynamics such as climate-impacting cloud formation like contrails and cirrus clouds.

Humidity content at ice supersaturated conditions is mostly challenging in atmospheric models. ERA5, the fifth generation of ECMWF re-analysis can provide global long-term information about atmospheric humidity at these altitudes. ERA5 humidity product uncertainty over the contrails-relevant altitudes has not been fully assessed. In BeCoM, we are evaluating ERA5-derived WVMR profiles over the Paris region (Alraddawi et al., 2025) and over the tropics (Alraddawi et al in preparation).

Satellite-based observations provide a valuable tool for monitoring water vapor at global scales. Among these, the Microwave Limb Sounder (MLS) on NASA's Aura satellite has emerged as a significant asset for retrieving water vapor mixing ratios in the upper troposphere and lower stratosphere. Despite its broad spatial coverage and long-term data availability, uncertainties in MLS water vapor measurements—particularly in regions of high humidity and dynamic atmospheric variability—pose challenges for accurate characterization. Comparing MLS data with other measurements offers a unique opportunity to assess the satellite's current capabilities in accurately describing upper tropospheric water vapor content.

To address these uncertainties, a limited number of instruments are able to accurately measure the vertical distribution of the water vapor in the Upper Troposphere (UT). Ground-based Raman lidars

This project has received funding from the European Union's Horizon Europe
Research and innovation program under Grant Agreement No 101056885

have proven to be a reliable validation instrument due to their high vertical resolution and ability to provide continuous profiles of water vapor mixing ratios. Some of the NDACC Raman lidars (all ground-based) are able to reach the UT/LS as the Table Mountain Facility (United States; (Leblanc et al., 2012)) and Tor Vergata system (Italy; Dionisi et al., 2010) lidars. Nevertheless, the altitude of the tropopause is lower in such mid-latitude areas than in the (sub)tropics.

Over the tropics, where ground-based observations are sparse, a powerful lidar is installed at Reunion island. This Raman lidar system is designed to simultaneously monitor the water vapor from the ground up to the lower stratosphere and the temperature in the stratosphere and the mesosphere. Since 2012, setup at the Maïdo facility located at 2160 m asl (Baray et al., 2013) , two measurement campaigns (Keckhut et al., 2015) (Dionisi et al., 2015) have demonstrated the ability of this lidar to measure WVMR quantities of only few ppmv in the UT/LS, and to reach tropical UT/LS altitudes via longer integration periods of measurements (Vérèmes et al., 2019).

This section focuses on evaluating the uncertainties associated with MLS water vapor retrievals by conducting a detailed comparison with Raman lidar observations over tropical regions. The primary objective is to assess the accuracy of MLS measurements, identify potential biases, and quantify their limitations in describing upper tropospheric water vapor. The outcomes of this study will provide critical insights into the reliability of satellite-based water vapor datasets and their application in climate research and atmospheric studies. Hereafter a brief description of this monthly approach, followed by the comparison results, discussion and conclusions.

2.2. Dataset

2.2.1. The Tropical Raman Lidar

Raman lidar water vapor mixing ratio is retrieved from the ratio of the Raman water vapor (Sherlock et al., 1999) and the Raman Nitrogen channels (Keckhut et al., 1990). Then, after calibration a direct measurement of the water vapor mixing ratio is obtained.

Located at the Maïdo observatory (Baray et al., 2013) at la Réunion island: 21°S, 55.4°E, lid1200 has a laser power of 400 mj/pulse. In order to get a water vapor mixing ratio profile, Raman backscattered signals returned respectively at 387 nm by Nitrogen and at 408 nm by atmospheric water vapor are used, corrected for background noise, accounting for the atmospheric differential transmission T(z) and scaled by the calibration coefficient C. Signals are measured by number of photons/bin/shot.

The tropical lidar lid1200 (Dionisi et al., 2015), is able to provide WVMR profiles that reach 15 km on a routine basis. As explained by (Vérèmes et al., 2019), longer temporal screening of the Raman signals would enhance the lidar SNR and hence allows higher WVMR profiles, for example 10 minutes integration periods would give a WVMR profile up to 14 km, while 40 minutes integrated signals would reach higher and so on (Figure 1). Following this concept we suggest a pseudo-monthly screening, by which Raman signals are summed over many night-hours during a few days within each month, resulting in an integration of at least 1920 minutes of Raman signals. This nearly monthly newly developed dataset would enable the comparison to satellites, having more overpasses per month (compared to shorter screening). We further enhance comparison quality by filtering out all lidar points where the error exceeds 30%, Hence, we could generate 100 pseudo-monthly WVMR profiles with different vertical ranges over the 2013 to 2023 period.

This project has received funding from the European Union's Horizon Europe Research and innovation program under Grant Agreement No 101056885

Figure 1. Mean Lidar WVMR profile (g/kg) integrated over (10 minutes, 40 minutes, 4 hours)*, credit: Vérèmes et al., 2019 .*

2.2.2. Microwave Limb Sounder MLS

The Earth Observing System EOS Aura Microwave Limb Sounder (MLS) standard product for water vapor (ML2H2O) is derived from radiances measured primarily by the 190 GHz radiometer (Lambert et al., 2015). Spatial coverage is near-global (-82 degrees to +82 degrees latitude), with each profile spaced 1.5 degrees or ~165 km along the orbit track (roughly 15 orbits per day). The recommended useful vertical range is between 316 and 0.00215 hPa, and the vertical resolution is about 1.5 km at 316 hPa increasing to 3.5 km to 4.64 hPa, and degrading to 15 km above 0.1 hPa.

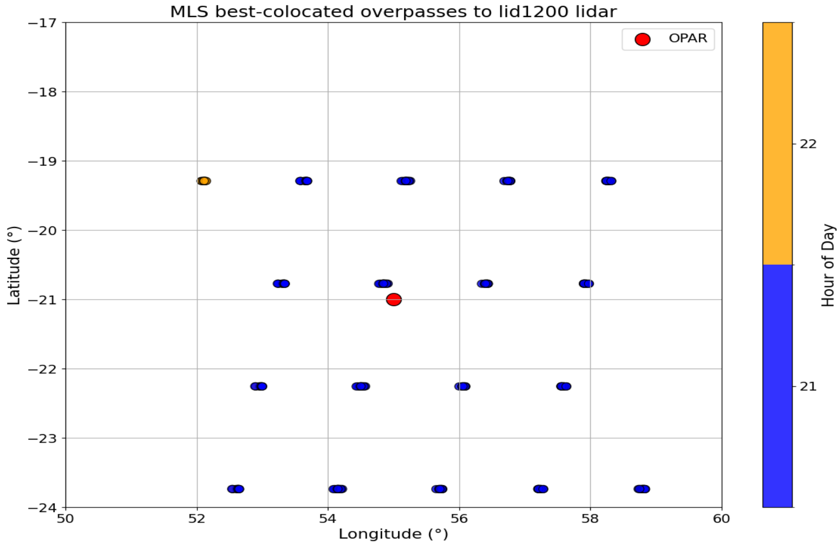

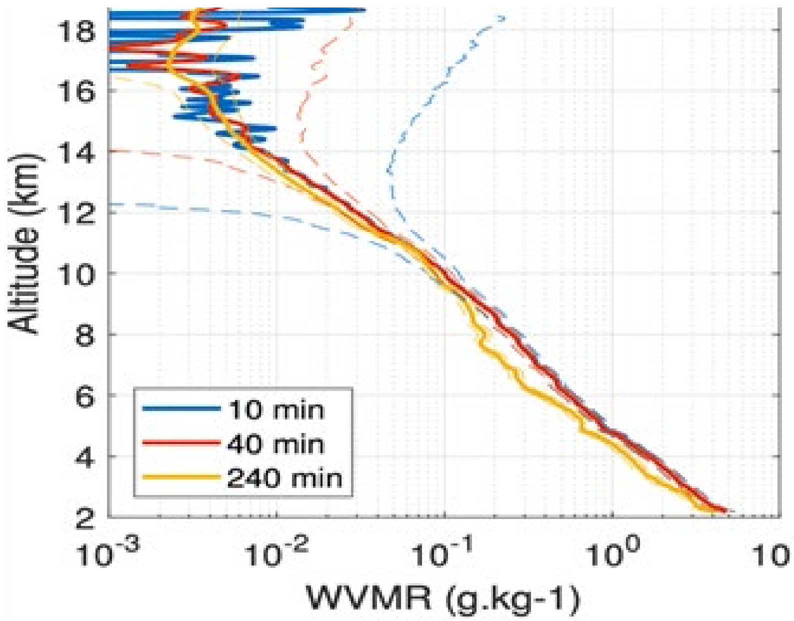

Figure 2. MLS overpasses locations w.r.t Lidar location (Maïdo observatory at the Reunion island which is represented by the red cercle).

In the current study, we are following the recommended useful vertical range of MLS dataset, hence we are evaluating WVMR product over altitudes between 10 and 16 km, with vertical resolution about 1.5 km, and a maximum spatial drift to Maïdo laboratory (Lidar location) about 4°. MLS overpasses collocated with the lidar location over the 2013-2023 period are shown on Figure 2, where MLS nocturnal passes were at 21h and 22h local time. Considering only best coincident overpasses at

This project has received funding from the European Union's Horizon Europe Research and innovation program under Grant Agreement No 101056885

temporal (to lidar coincident nights and hours) and spatial (up to 4° drift to lidar location) scales, 76 MLS pseudo-monthly WVMR profiles were obtained to be compared to coincident lidar ones, median profiles of both dataset are presented in Figure 3.

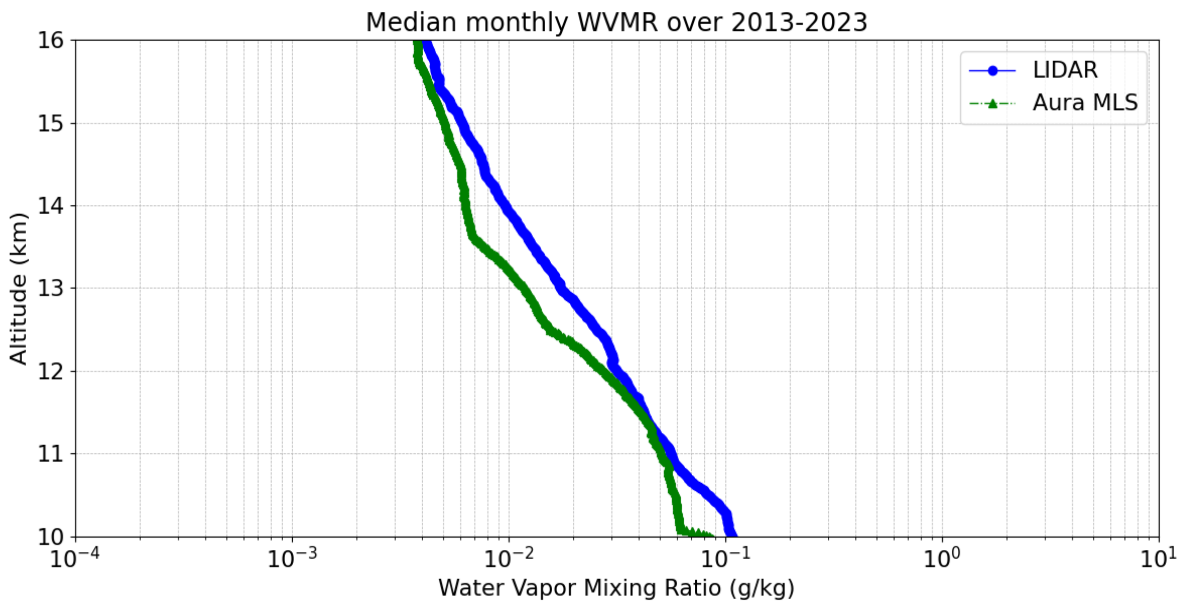

Figure 3. WVMR median pseudo monthly profile of the compared dataset (median of 76 profiles between 2013 and 2023): Lidar(blue), MLS (green), over the 10 to 16 km altitudes.

2.2.3. ERA5

ERA5 is the fifth generation of meteorological reanalysis produced by the European Centre for Medium-Range Weather Forecasts (ECMWF) Integrated Forecasting System (IFS). It is operational since 2016 (Hersbach et al., 2020). ERA5 benefits from a decade of developments in model physics, core dynamics and data assimilation to guide and readjust the outputs of interactive models. For the present study, we use the operational ERA5 product.

ERA5 used data set (Hersbach et al., 2023) has a significantly enhanced horizontal resolution of 31 km (0.25°), compared to 80 km for the previous reanalysis ERA-Interim, and hourly output over 37 pressure levels, and provides a publicly available detailed record of the global atmosphere from 1979 onward (and with less frequent data between 1950-1979). Uncertainty spread of tropospheric humidity samples, mainly random errors, decreases over time. Relative spread is lowest near the surface (5%), but around 15% for specific humidity at 300 h. Pa since 2015 (Hersbach et al., 2020).

WVMR is calculated using the specific humidity variable of the nearest pixel to the lidar location, i.e Maïdo observatory (La Réunion Island) location for the tropics analysis, and SIRTA observatory (20 km south of paris) for mid-latitude study. Data is screened with maximal spatial drift of 0.1° and the best temporal coincidence considering the same Lidar night and measurements hours. Over the Tropics, ERA5 pseudo monthly WVMR profiles are retrieved by averaging the coincident hours to lidar over each month. Hence, 100 ERA5 WVMR pseudo-monthly profiles were compared with Lidar ones,

This project has received funding from the European Union’s Horizon Europe Research and innovation program under Grant Agreement No 101056885

median profiles of both dataset are presented in Figure 4. Over the mid-latitudes, the original (operational) temporal and spatial screening is used (hourly dataset).

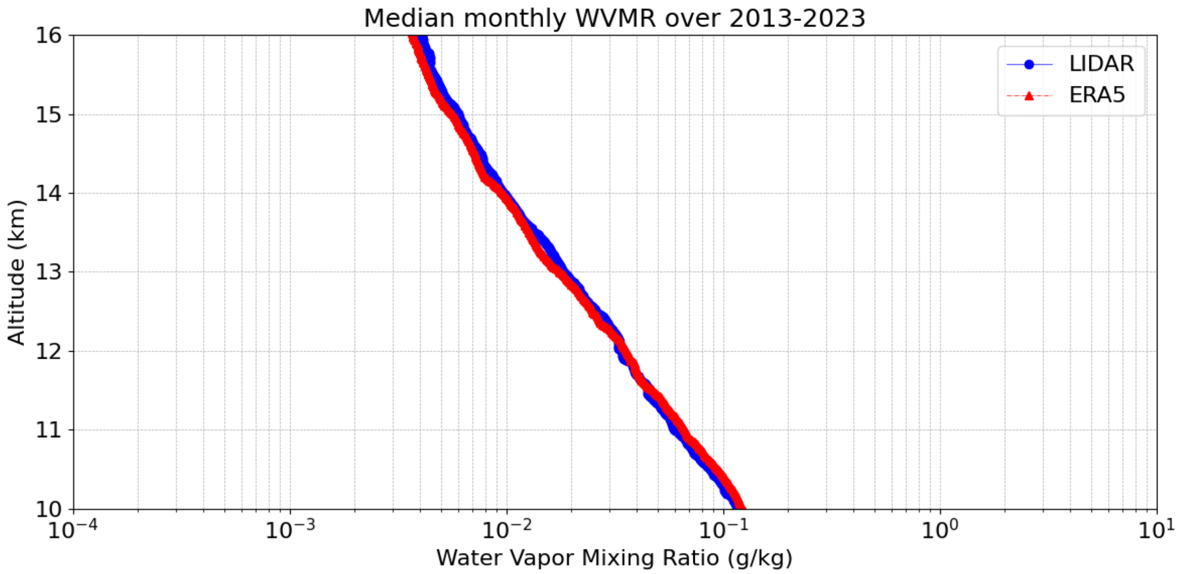

Figure 4. WVMR median pseudo monthly profile of the compared dataset (median of 100 profiles between 2013 and 2023): Lidar(blue), ERA5 (red), over the 10 to 16 km altitudes.

2.2.4. GRUAN Processed Meteomodem M10 Radiosondes

Balloon borne radiosondes are capable to describe the humidity profile over the site where they are launched. The nearest meteorological station to the SIRTA observatory (our mid-latitude study zone) is Trappes (Meteo France station id: 07145), at about 20 km, where regular Meteomodem Co., (located 70 km from Paris, France, at Ury 77760) M10 radiosonde launches are available at midnight and midday.

Being ready for simultaneous water vapour and cloud measurements, IPRAL Lidar has another plus-value performed by the GRUAN (Seidel et al., 2009) regular processing to obtain well calibrated water vapour measurements of the Meteomodem balloon launches. As a step to meet the (GRUAN) requirements (Seidel et al., 2009), few corrections were applied on the M10 radiosondes data set (Dupont et al., 2020). These corrections concerned the following: (1) the calibration correction; (2) a slow regime due to the slow diffusion of molecules through the sensor, especially at very high and very low relative humidity conditions; (3) the relative humidity sensor dependence on the gradient of temperature; and (4) the time lag at cold temperatures which affects measurements in regions of strong relative humidity gradients. GRUAN corrected relative humidity data set (Dupont et al., 2020), being available only since 2018, is used to retrieve the GRUAN WVMR data set, used in the current study, to be compared later (Section 2.3.4) with the Lidar WVMR profiles (Alraddawi et al., 2025) to assess their uncertainty over the Paris region. GRUAN processed Meteomodem M10 WVMR is retrieved using the corrected relative humidity RH (all corrections applied), the air temperature, and the pressure levels.

2.3. LIDAR comparison to other datasets

One of the main challenges towards the current study, is the very few lidar-like satellites overpasses to allow this comparison (Figure 2). Thus a pseudo-monthly lidar, MLS, and ERA5 WVMR datasets were generated to enable the maximum MLS overpasses and enhance the comparison into the upper troposphere making use of lidar special ability of getting higher profiles after summing longer Raman

This project has received funding from the European Union's Horizon Europe Research and innovation program under Grant Agreement No 101056885

signals. Pseudo-monthly Raman lidar WVMR profiles (Alraddawi et al., in preparation) are compared to MLS and ERA5 re-analysis ones at a tropical site. Also, Raman Lidar IPRAL WVMR (Alraddawi et al., 2025) were used to qualify ERA5 and Radisosondes UT humidity content over the mid-latitudes at their originate temporal screening (hour). This comparison will enable us to assess the uncertainties of these datasets at cruise altitudes. Hereafter, the comparison results are presented.

2.3.1. LIDAR Vs. MLS

The relative differences between WVMR profiles from the lidar and MLS satellite observations were analyzed over a pseudo-monthly scale. In this approach, MLS measurements that coincide with lidar night-time observations within a given month are averaged to create a representative monthly profile. The 2D temporal evolution of the relative differences (Lidar – MLS) from 2013 to 2023 is presented in Figure 5.

The useful altitude range for comparison is between 10 to 16 km, where both MLS and lidar exhibit reliable observations. Over the analyzed period, a total of 76 pseudo-monthly WVMR profiles were obtained for comparison. We report a systematic dry bias (red shading in Figure 5) in MLS relative to lidar, with relative differences frequently exceeding ±20%. Gaps in the data correspond to periods where coincident MLS overpasses to lidar observations were insufficient to generate a representative MLS monthly profile.

The median relative difference in water vapor mixing ratio (WVMR) between the lidar (lid1200) and MLS over the analyzed period, with a focus on the 10–16 km altitude range is also analyzed (Figure 6). The black dashed line represents the median profile of the relative differences, while the shaded blue area indicates the 95% confidence level of the variability of the differences, expressed as ±2 times the pseudo standard error normalized by the root of the number of participated profiles points each altitude bin. We observe altitude-dependent dry MLS bias, with a tendency for lidar WVMR values to be closer to MLS between 11 and 12 km but up to 30 % higher upwards. The spread of variability increases above ~14 km, likely reflecting the growing impact of reduced lidar sensitivity and MLS vertical resolution at higher altitudes.

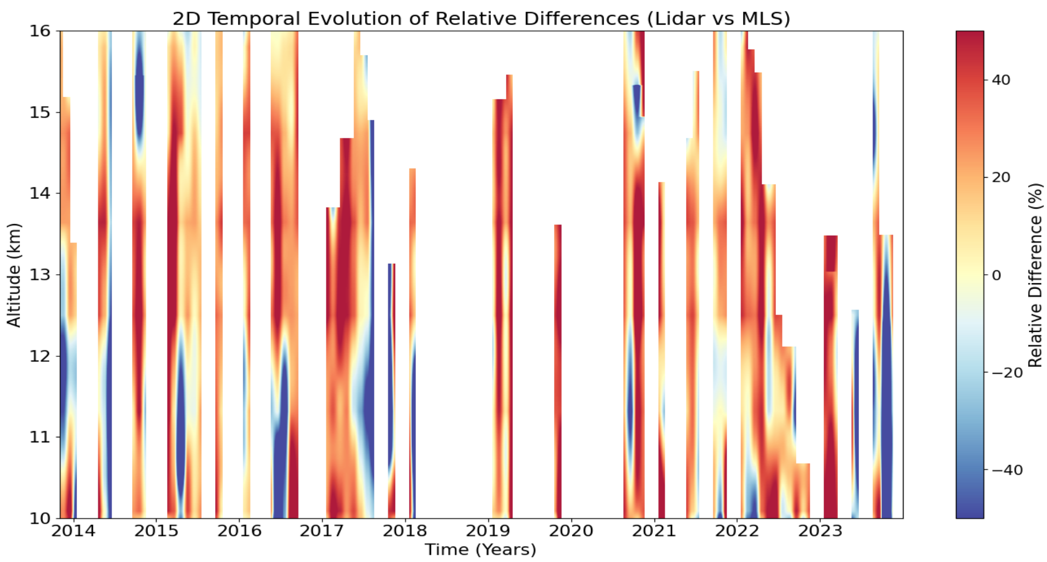

Figure 5. 2D temporal evolution of relative differences in water vapor mixing ratio (WVMR) between lidar and MLS (Lidar – MLS) from 2013 to 2023. Positive values (red) indicate that lidar reports higher WVMR than MLS, while negative values (blue) indicate a lower lidar WVMR. Gaps correspond to months with insufficient coincident data.

This project has received funding from the European Union's Horizon Europe Research and innovation program under Grant Agreement No 101056885

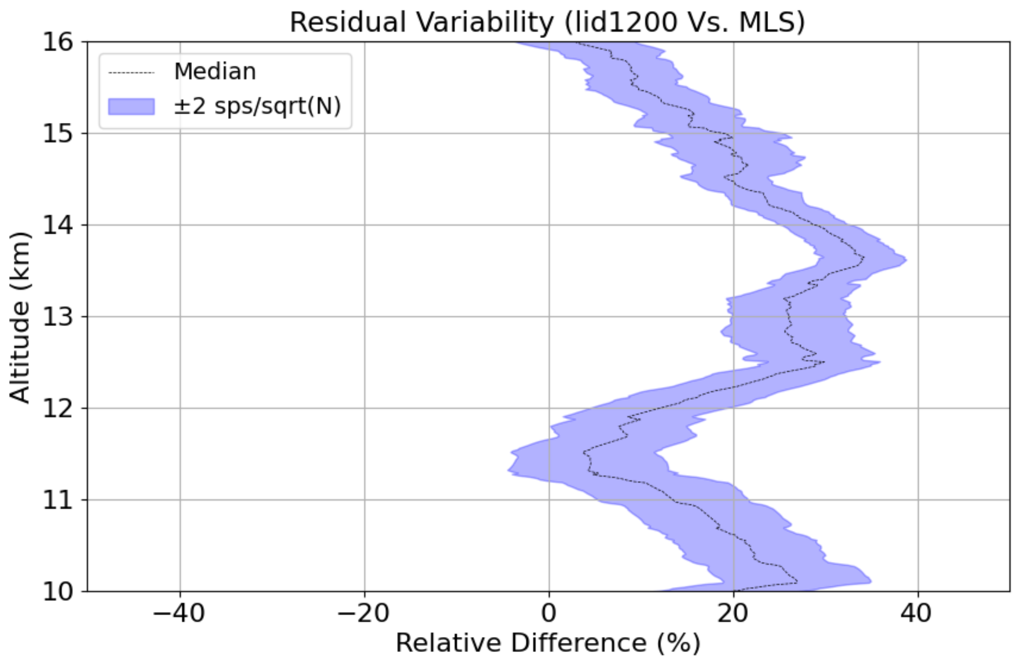

Figure 6. Median Lidar WVMR relative bias (%) w.r.t MLS, (over 76 compared profiles from 2013 to 2023) shaded zones refine the 95% confidence level of the relative error.

Breaking results into two main seasons over the tropical column, considering a dry season from May to September, and a wet one for other months. The analysis shows that the relative differences present a slightly different structure during the wet season, The variability is generally larger compared to the dry season, particularly below 12 km (Figure 7, left panel), which may reflect better lidar performance due to higher humidity, and hence this might be due to less lidar calibration issues which improve the lidar efficiency over the upper troposphere altitudes.

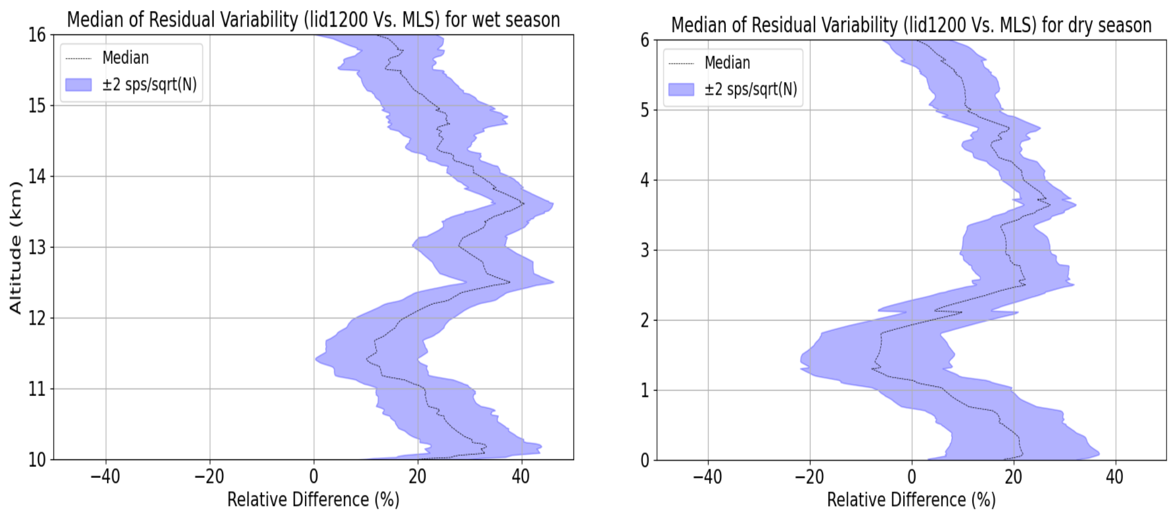

Figure 7. Median Lidar WVMR relative bias (%) w.r.t MLS during wet season months (left panel), and during dry season months (right panel) over the Tropical 2013 to 2023 study period. Shaded zones refine the 95% confidence level of the relative error.

This project has received funding from the European Union's Horizon Europe Research and innovation program under Grant Agreement No 101056885

2.3.2. LIDAR Vs. ERA5 over the Tropics

The relative differences between water vapor mixing ratio (WVMR) profiles from the lidar and the ERA5 reanalysis were also analyzed on a pseudo-monthly scale over the Tropics. In this approach, the ERA5 hourly dataset coinciding with lidar nighttime observations within a given month is averaged to create a representative monthly profile. For comparison, we focus on an altitude range of 10 to 16 km. Over the analyzed period (from 2013 to 2023), a total of 100 pseudo-monthly WVMR profiles were obtained. The relative differences profiles between lidar and ERA5 water vapor mixing ratio (WVMR) profiles are expressed as (Lidar – ERA5) in percentage is analyzed.

The temporal evolution of these differences (Figure 8) shows positive values (red shading) which indicate a dry bias in ERA5 relative to lidar, while negative values (blue shading) indicate a wet bias. The results show that, above 12 km, relative differences mostly remain within ±10%, with a consistent dry bias in ERA5. White gaps in the figure correspond to periods when lidar observations were unavailable (e.g., due to technical issues or the COVID-19 pandemic) or did not meet quality criteria (error > 30%). The Lidar Bias to ERA5 is considered as the median profile of all 100 relative difference profiles. We report a small dry bias in ERA5 relative to the lidar, with relative differences not exceeding ±10% at altitudes above 12 km. Small wet bias is also reported for lower altitudes (between 10 and 12 km).

The analysis separates the tropical column into two main seasons: the dry season (May to September) and the wet season (remaining months). The relative differences between lidar and ERA5 exhibit distinct patterns in each season (Figure 10).

During the wet season, the bias variability is generally larger, particularly below 12 km (Figure 10, left panel). This could be attributed to increased humidity, which enhances lidar backscatter signals and potentially reduces calibration uncertainties, leading to improved measurement efficiency in the upper troposphere. In contrast, during the dry season (Figure 10, right panel), the median relative difference (bias) appears more stable, with reduced variability throughout the profile. This could be linked to drier atmospheric conditions, which may limit lidar signal enhancement and introduce greater sensitivity to calibration uncertainties. The more consistent structure of the differences suggests that systematic biases, such as those related to instrumental calibration and model assumptions in ERA5, might be more dominant during this period.

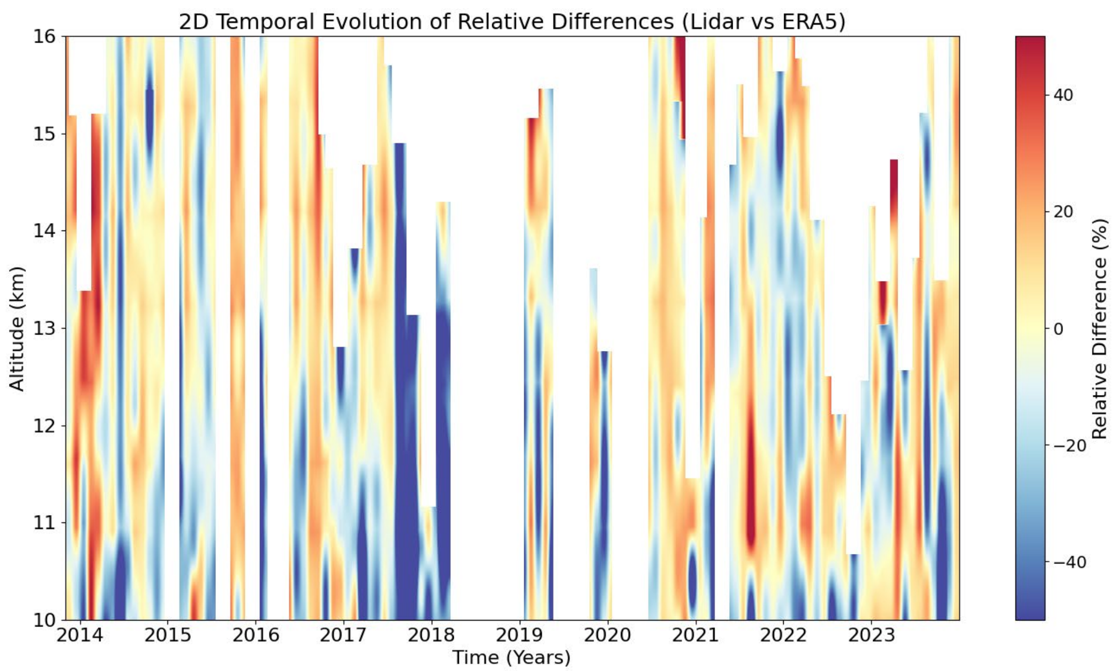

This project has received funding from the European Union's Horizon Europe Research and innovation program under Grant Agreement No 101056885

Figure 8. 2D temporal evolution of relative differences in water vapor mixing ratio (WVMR) between lidar and ERA5 (Lidar – ERA5) from 2013 to 2023. Positive values (red) indicate that lidar reports higher WVMR than ERA6, while negative values (blue) indicate a lower lidar WVMR. Gaps correspond to months with missed/insufficient lidar data.

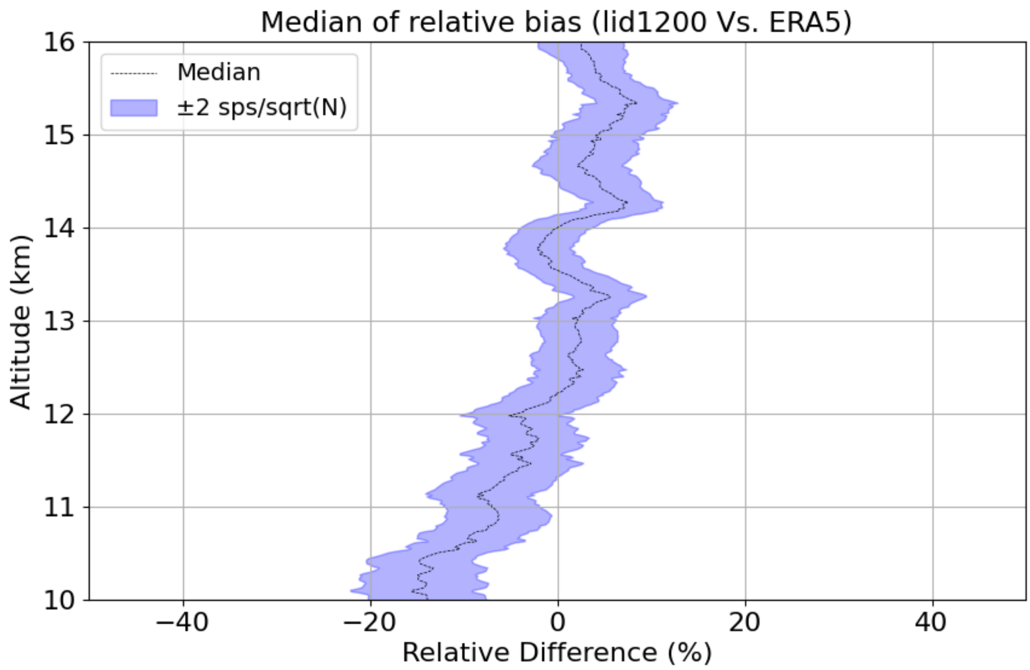

Figure 9. Median Lidar WVMR relative bias (%) w.r.t ERA5, (over 100 compared profiles from 2013 to 2023) shaded zones refine the 95% confidence level of the relative error.

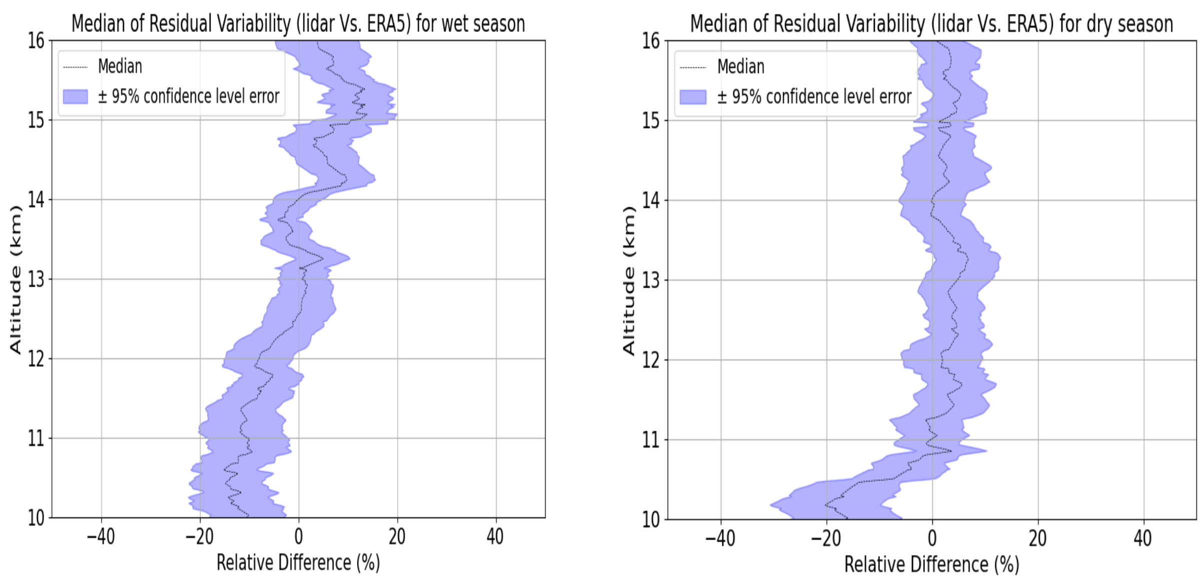

Figure 10. Median Lidar WVMR relative bias (%) w.r.t ERA5 during wet season months (left pannel), and during dry season months (right pannel) over the 2013 to 2023 study period. Shaded zones refine the 95% confidence level of the relative error.

This project has received funding from the European Union's Horizon Europe Research and innovation program under Grant Agreement No 101056885

2.3.3. LIDAR Vs. ERA5 over the mid-latitudes

We assess hereafter uncertainties of upper tropospheric ERA5 hourly-based dataset (Hersbach et al., 2023) via the comparison to Raman Lidar WVMR profiles (Alraddawi et al., 2025) over the Parisian region. For the present study, midnight hours IPRAL Lidar WVMR were compared to the operational ERA5 same hours profiles as well as a recent corrected ERA5 dataset to be detailed later in this section. The analysis spans the altitude range of 7000 m to 11,000 m, covering the upper troposphere (UT) bounded by aviation activity during 6 years (2018-2024). The comparison shows very good agreement with significant correlation (70–90%) mostly. However, we report ERA5 dry bias with respect to Lidar which increases with altitude at the UT region.

This ERA5 dry bias has been previously reported by (Hofer et al., 2024) who suggested a lookup table to correct operational ERA5 relative humidity values under ice supersaturation conditions, on bi-variate quantile mapping. The corrected data set was recently shared with the scientific community based on the 1995–2022 period IAGOS relative humidity measurements over multi-site; these flights aimed to check operational ERA5 RHi values (IAGOS is The European research infrastructure: In-Service Aircraft for a Global Observing system, previously called MOZAIC, IAGOS provides air composition measurements of several key variables with sensors onboard commercial aircraft). Hence, a corrective lookup table was kindly provided by the authors of the study (Hofer et al., 2024) in the framework of the BeCoM project, this table includes corrected RHi values, only for ice supersaturation events where air temperature below 250 k. Because of the water vapour variability, it is impossible to have an exact coincidence between IAGOS flight and IPRAL Lidar, so the current study is based on indirect comparisons. Thereby, IAGOS corrected ERA5 midnight hour WVMR data set, for dates coincident to Lidar and GRUAN processed M10 measurements, is generated and is also examined via the comparison to Lidar observations.

The median relative bias (%) of IPRAL Lidar WVMR compared to both ERA5: Operational in purple dashed line; and ERA5 corrected with IAGOS (lighter pink dashed line) data sets is displayed in Figure 11. The shaded regions represent variability around the median Lidar bias (at the 95% confidence level).

Upper troposphere Lidar WVMR comparison to ERA5 (including the IAGOS corrected data set) shows general agreement, but an obvious ERA5 dry bias is reported; enhancing with altitude, it seems that ERA5 gives smaller values in the upper troposphere (Figure 11). This might be due to ERA5 insufficient sensibility to detect extreme water vapour content during ice supersaturation events. Such behaviour is probably linked to reduced ERA5 RHi values due to the use of saturation adjustment in the micro-physics parametrization, or even some form of relaxation method as reported by (Gierens et al., 2020; Wolf et al., 2023; Thompson et al., 2024) for ERA5 and following (Reutter et al., 2020) for ERA-interim.

IAGOS-corrected ERA5 WVMR data set, adapted using corrected RHi (Hofer et al., 2024), shows significantly better agreement with Lidar, with smaller biases and reduced variability. Particularly noteworthy is the reduced bias when using the IAGOS-corrected ERA5 data set (Figure 11). This improvement validates the corrections applied to ERA5 by incorporating in situ aircraft measurements, which enhance the model's representation of upper tropospheric humidity. Such findings demonstrated that assimilating high-resolution aircraft data significantly reduces model biases in regions critical for contrail formation and ice supersaturation. However, the remaining persistent ERA5–IAGOS corrected dry bias (Figure 11) with respect to Lidar suggests that there might be other anomalous events affecting ERA5 capacities to detect the right humidity content particularly at upper tropospheric altitudes. Here, we are reporting a possible systematic ERA5 bias on altitudes above 8.5 km, might be linked to other problems than ERA5 model mishandled ice supersaturation events.

This project has received funding from the European Union's Horizon Europe Research and innovation program under Grant Agreement No 101056885

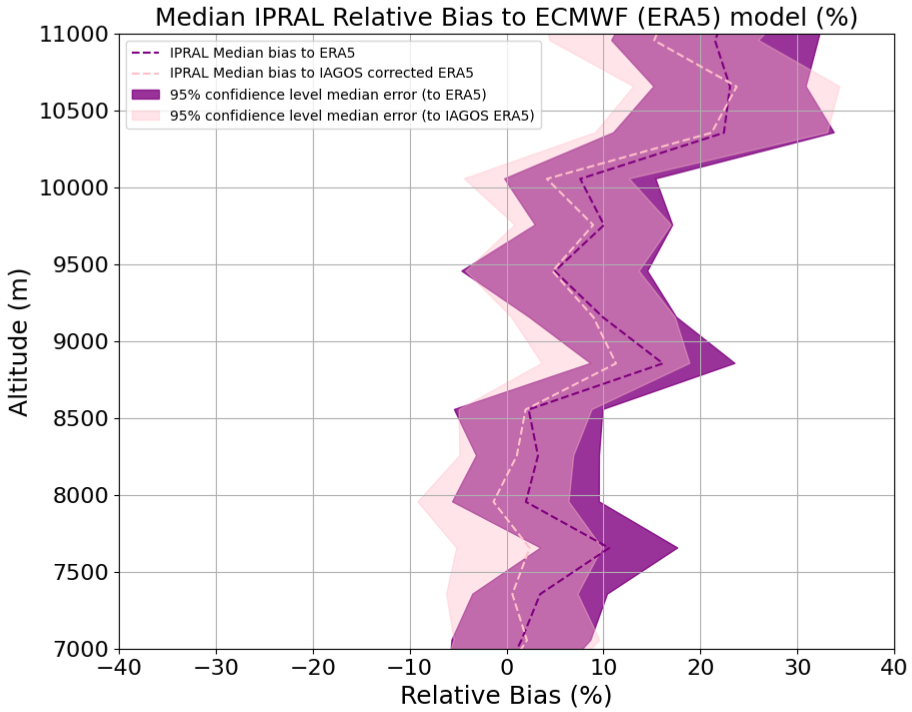

Figure 11. Median IPRAL WVMR relative bias (%) with respect to ERA5 (purple) and IAGOS corrected ERA5 (pink), shaded zones refine the 95% confidence level of the relative error (Alraddawi et al., 2025).

2.3.4. LIDAR Vs. GRUAN-processed Radiosondes

IPRAL calibrated WVMR profiles (Alraddawi et al., 2025) of mid-night hours are compared to available co-located midnight launches. WVMR profiles from GRUAN-processed M10 radiosondes datasets measured at the nearest meteorological station to SIRTA: Trappes (Dupont et al., 2020). This data set, produced since 2018, allowed the whole comparisons to be carried out over the 2018–2014 period to meet a commune temporal range of all compared data sets.

The median relative bias (%) of the Lidar WVMR to GRUAN processed M10 radiosondes is analysed over altitudes from 7000 m to 11,000 m. The biases range from −5% to +10%, with variations across different altitude levels (Figure 12). The comparison of co-located profiles shows excellent agreement with significant correlation about ~90% mostly.

Below 8000 m, the relative bias is slightly negative, indicating a more humid GRUAN radiosondes with respect to Lidar WVMR. This small negative bias at lower altitudes might suggest the need for further calibration efforts or retrieval refinement for Lidar. However, it might also be linked to radiosondes' possible shift far away from the zenith of the launch site. Both hypotheses will be further investigated during the later upcoming more extensive measurements campaign at SIRTA, in 2025, which will be detailed in section 3.

Upwards, the Lidar and GRUAN profiles have excellent agreement with median bias (around ±5%). This bias is transitioned to positive values for higher altitudes (>10 km), increasing with altitude up to +10%, suggesting a better Lidar sensibility to water vapour content in the upper troposphere, particularly at cruise altitudes (~10–11 km). At these levels, the troposphere often exhibits ice supersaturation events, where traditional radiosondes may struggle to fully capture the localised humidity variability, which is one evident reason behind the use of GRUAN analysed data set. The larger positive bias above 10,000 m emphasises the Lidar potential utility in capturing atmospheric conditions, particularly related to contrail formation mechanisms at cruise altitudes.

This project has received funding from the European Union's Horizon Europe Research and innovation program under Grant Agreement No 101056885

The 95% confidence level of the median value error is assessed by doubling the pseudo standard deviation error (of the relative differences) and normalising it considering the effective number of participated profiles of each altitude bin. This variability becomes more pronounced above 9500 m, where Lidar measurements are often more influenced by reduced signal-to-noise ratios and hence a smaller number of profiles attending 11 km. The overall good agreement between 8 and 10 km, with biases mostly within ±5%, highlights the Lidar reliable calibration and retrieval performance.

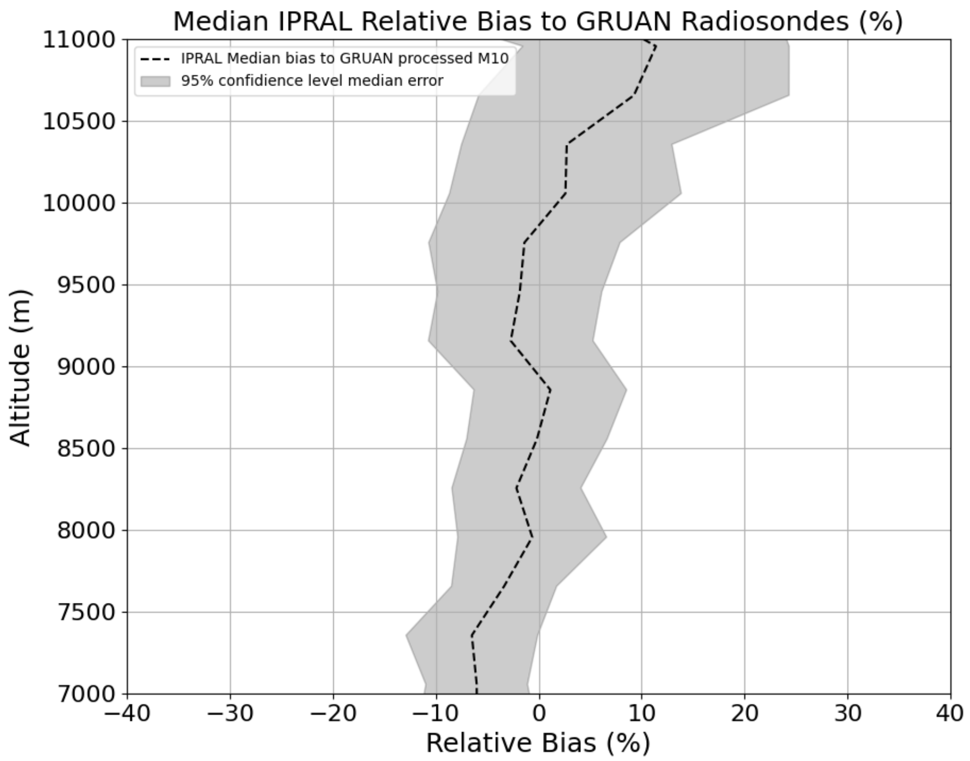

Figure 12. Median IPRAL WVMR relative bias (%) with respect to GRUAN processed M10 radiosondes. Shaded zones refine the 95% confidence level of the relative error (Alraddawi et al., 2025).

2.2.5. ERA5 VS GRUAN-Processed Radiosondes

This sub-section evaluates 3 years (2020 to 2022) of Meteomodem radiosondes (M10), which includes two datasets, one processed operationally by Météo France MF and the other using GRUAN standards, both are compared to ECMWF operational ERA5 relative humidity data acquired at the Trappes meteorological station in France, focusing on the upper troposphere (Diarra et al., 2026, in preparation). Meteomodem radiosondes RH values are on average higher than ERA5 ones, by about from 2 % at 800 hPa up to 10% at 200 hPa. The operational MF processing generally gives on average higher RH than the GRUAN processing, although GRUAN shows higher supersaturation. However, the largest differences appear in the 200–300 hPa layer (~9–12 km), a critical region for the formation of cirrus clouds and contrails.

Figure 13 presents vertical profiles of RH differences between radiosondes and ERA5, as a function of humidity regimes in the upper troposphere. First, each ERA5 and M10 profile is interpolated at the vertical resolution of the M10 radiosounding performed during the day of the 1st January 2020. Second, for each altitude, the ERA-5 values of all the profiles are divided into two groups : those with relative humidity (RH) above 90% and their corresponding M10 points (labeled RH>90% in Figure 13) and those with relative humidity (RH) below 90% and their corresponding M10 points (labeled RH<90% in Figure 13). This method yields getting two series of data couples. Third, for each couple, the RH difference ΔRH=M10-ERA5 has been calculated and all the relative humidity differences of each series

This project has received funding from the European Union’s Horizon Europe
Research and innovation program under Grant Agreement No 101056885

have been averaged. The number of RH differences averaged at each altitude for each series is indicated on Figure 13c. In addition to the mean, the 5th and 95th percentiles the percentiles 5 and 95% of the relative humidity differences have also been calculated and all are shown on Figure 13a for the GRUAN processing and on Figure 13b for the Météo-France processing.

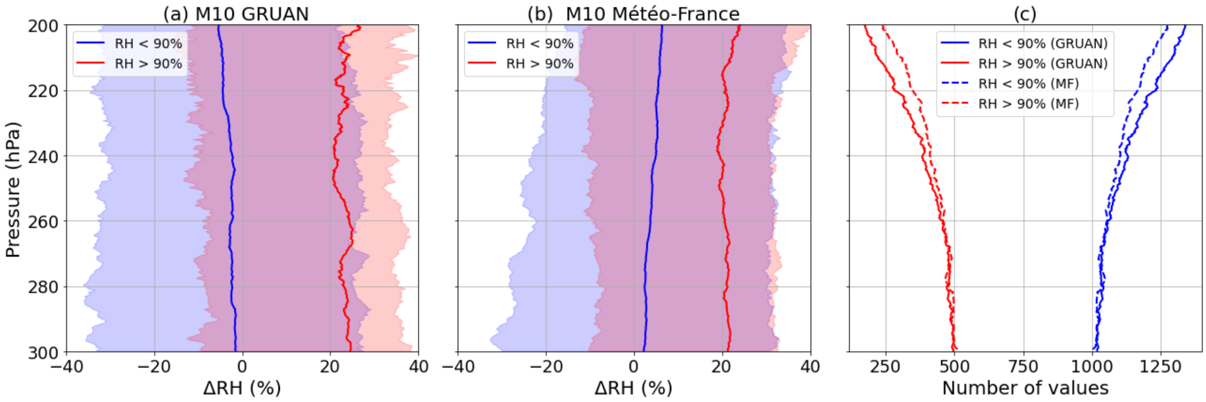

Figure 13. Vertical profiles of differences between (a) M10 GRUAN-analysed and ERA5, (b) M10 MF analysed and ERA5, according to humidity conditions: RH<90% in blue or RH>90% in red, data includes (2020 to 2022) in the 200-300 hpa range. The solid lines are the medians of the RH differences, and the shaded areas indicate the 5th and 95th percentiles range; (C) corresponding number of values used for each condition, GRUAN (solid lines) and MétéoFrance (dashed lines) (Diarra et al., to be submitted)

In wet conditions (RH > 90%), which represent less than 500 profiles of the 1555 profiles available at each level in the 200-300 hPa layer, discrepancies increase markedly. ΔRH medians range are between 19 and 26 % for both *M10GRUAN* and *M10MF* indicating that radiosondes often exhibit larger RH than ERA5 under moist conditions, even if it is not always the case as the 5th percentile is negative, reaching and can be down to -14%. The GRUAN processing retrieves slightly higher ΔRH than the MF processing. The variability of the ΔRH in wet conditions is lower than in dry conditions(RH < 90%) and is also not symmetric, with medians closer to the 95th percentiles than the 5th percentiles.

The impact of the radiosonde change from Meteomodem M10 to M20 was also investigated using Météo-France radiosonde data from Nîmes. M20 data (launched after 2021) appear to be closer to ERA5 than M10 data, particularly during daytime. However, since better agreement is also observed at Trappes (which has remained on M10), the improvement cannot be attributed solely and with certitude to the instrument change. Radiosondes from Nîmes show a higher occurrence of intermediate humidities (40–90 % RH) compared to ERA5, which is not the case at Trappes. This may be explained by the fact that Trappes soundings are assimilated into ERA5, unlike those from Nîmes. Overall, no marked discontinuity is detected between M10 and M20, which is important for long-term climate studies.

These results suggest that ERA5 appears to fail to capture possible supersaturation events that are often recorded by radiosondes. This may be related to the cloud parameterization in the ERA5 Integrated Forecasting System (IFS) model, which could trigger cloud formation too quickly, leading to an instantaneous reduction of water vapor to the saturation level upon nucleation (Tompkins et al., 2007).

2.4. Conclusions

Valuable information about humidity content at cruise altitudes over the Parisian region and the Tropics are possibly obtained by Satellites like MLS, re-analysis (ERA5) and Radiosondes. However, accurate UT WVMR measurements are challenging.

This project has received funding from the European Union's Horizon Europe
Research and innovation program under Grant Agreement No 101056885

In general, Lidar derived WVMR shows higher humidity content than the other compared data sets. This may reflect the Lidar sensitivity to detecting low water vapour concentrations. This capability is crucial for studying contrail formation mechanisms and complements the radiosonde and ERA5 data sets, which often underestimate humidity content at these altitudes.

Satellites MLS uncertainties can be assessed w.r.t Lidar by monthly screening comparisons; ERA5 bias can be assessed even at finer temporal resolutions (hourly).

The comparison efforts show:

- MLS exhibits dry bias w.r.t Lidar can reach 30% at the UT, particularly above 12 km and during the wet season. This dry MLS bias is consistent with findings reported in previous studies, such as Dionisi et al. (2015) and Yan et al. (2016) which also have observed a significant dry bias of MLS WVMR compared to lidar in the upper troposphere
- ERA5 seemed to under-estimate UT values, bias w.r.t lidar about 10-20%, more obvious on finer temporal scales. Similar ERA5 dry bias was also reported over midlatitudes upper troposphere (Wolf et al., 2023; Hofer et al., 2024),
    - Midlatitude: up to 20%, IAGOS-MOZAIC corrected ERA5 datasets has reduced biases and variability w.r.t lidar, validating its corrections and demonstrating the value of in situ data (Alraddawi et al., 2025)
    - Tropics: up to 10%, ERA5 UT WVMR dry bias is still present, but the monthly profiles bias has weaker amplitude (~10%), becomes more noticeable above 14 km and more obvious during the wet season. Nevertheless, ERA5 lower bias magnitude over the tropics may be attributed to the near-monthly screening applied.
    - ERA5 systematic dry bias: appears to be linked to ice supersaturation conditions that are mishandled by the model, but not exclusively, as the bias is reduced yet still persists even with IAGOS corrections
- GRUAN processed Radiosondes (M10) has the best agreement with Lidar (bias < 10%)
- GRUAN gives more humidity content than ERA5, especially under wet conditions (RH> 90%).

In conclusion, Raman Lidar demonstrates excellent agreement with GRUAN analysed radiosondes and improved ERA5 data sets. This supports the growing recognition of Raman Lidar as a valuable tool for numerical weather data assimilation in climate and atmospheric research. Lidar as a reliable and sensitive tool to measure humidity content at upper troposphere altitudes, and to further validate satellite and reanalysis, particularly under varying seasonal conditions in tropical regions.

The next section will introduce the intensive campaign runned out to further refine and extend the analysis to broader atmospheric conditions over the parisian region.

2.5. References

Alraddawi, D.; Keckhut, P.; Mandija, F.; Sarkissian, A.; Pietras, C.; Dupont, J.-C.; Farah, A.; Hauchecorne, A.; Porteneuve, J. Calibration of Upper Air Water Vapour Profiles Using the IPRAL Raman Lidar and ERA5 Model Results and Comparison to GRUAN Radiosonde Observations. Atmosphere 2025, 16, 351. https://doi.org/10.3390/atmos16030351

Baray, J.-L., Courcoux, Y., Keckhut, P., Portafaix, T., Tulet, P., Cammas, J.-P., Hauchecorne, A., Godin Beekmann, S., De Mazière, M., Hermans, C., Desmet, F., Sellegri, K., Colomb, A., Ramonet, M., Sciare, J., Vuillemin, C., Hoareau, C., Dionisi, D., Duflot, V., … Delmas, R. (2013). Maïdo observatory : A new high-altitude station facility at

This project has received funding from the European Union's Horizon Europe Research and innovation program under Grant Agreement No 101056885

Reunion Island (21° S, 55° E) for long-term atmospheric remote sensing and in situ measurements. *Atmospheric Measurement Techniques*, *6*(10), 2865-2877. https://doi.org/10.5194/amt-6-2865-2013

Dionisi, D., Congeduti, F., Liberti, G. L., & Cardillo, F. (2010). Calibration of a Multichannel Water Vapor Raman Lidar through Noncollocated Operational Soundings : Optimization and Characterization of Accuracy and Variability. *Journal of Atmospheric and Oceanic Technology*, *27*(1), 108-121. https://doi.org/10.1175/2009JTECHA1327.1

Dionisi, D., Keckhut, P., Courcoux, Y., Hauchecorne, A., Porteneuve, J., Baray, J.-L., Leclair de Bellevue, J., Vérèmes, H., Gabarrot, F., Payen, G., & others. (2015). Water vapor observations up to the lower stratosphere through the Raman lidar during the Maïdo Lidar Calibration Campaign. *Atmospheric Measurement Techniques*, *8*(3), 1425-1445.

Dupont, J.-C.; Haeffelin, M.; Badosa, J.; Clain, G.; Raux, C.; Vignelles, D. Characterizatio and corrections of relative humidity measurement from Meteomodem M10 radiosondes at midlatitude stations. J. Atmos. Ocean. Technol. 2020, 37, 857–871

Gierens, K.; Matthes, S.; Rohs, S. How well can persistent contrails be predicted? Aerospace 2020, 7, 169. [CrossRef]

Hersbach, H., Bell, B., Berrisford, P., Biavati, G., Horányi, A., Muñoz Sabater, J., Nicolas, J., Peubey, C., Radu, R., Rozum, I., & others. (2023). *ERA5-hourly data on model levels, ECMWF [data set]*.

Hersbach, H., Bell, B., Berrisford, P., Hirahara, S., Horányi, A., Muñoz-Sabater, J., Nicolas, J., Peubey, C., Radu, R., Schepers, D., & others. (2020). The ERA5 global reanalysis. *Quarterly Journal of the Royal Meteorological Society*, *146*(730), 1999-2049.

Hofer, S., Gierens, K., & Rohs, S. (2024). How well can persistent contrails be predicted? An update. *Atmospheric Chemistry and Physics*, *24*(13), 7911-7925. https://doi.org/10.5194/acp-24-7911-2024

Keckhut, P., Chanin, M.-L., & Hauchecorne, A. (1990). Stratosphere temperature measurement using Raman lidar. *Applied optics*, *29*(34), 5182-5186.

Keckhut, P., Courcoux, Y., Baray, J.-L., Porteneuve, J., Vérèmes, H., Hauchecorne, A., Dionisi, D., Posny, F., Cammas, J.-P., Payen, G., Gabarrot, F., Evan, S., Khaykin, S., Rüfenacht, R., Tschanz, B., Kämpfer, N. A., Ricaud, P., Abchiche, A., Leclair-de-Bellevue, J., & Duflot, V. (2015). Introduction to the Maïdo Lidar Calibration Campaign dedicated to the validation of upper air meteorological parameters. *Journal of Applied Remote Sensing*, *9*(1), 094099. https://doi.org/10.1117/1.JRS.9.094099

Lambert, A., Livesey, N., & Read, W. (2015). *MLS/Aura L2 Water Vapor (H2O) Mixing Ratio—Version 4* [Jeu de données]. NASA Goddard Earth Sciences Data and Information Services Center. https://doi.org/10.5067/AURA/MLS/DATA2009

Leblanc, T., McDermid, I., & Walsh, T. (2012). Ground-based water vapor Raman lidar measurements up to the upper troposphere and lower stratosphere for long-term monitoring. *Atmospheric Measurement Techniques*, *5*(1), 17-36.

Reutter, P.; Neis, P.; Rohs, S.; Sauvage, B. Ice supersaturated regions: Properties and validation of ERA-Interim reanalysis with IAGOS in situ water vapour measurements. Atmos. Chem. Phys. 2020, 20, 787–804

Seidel, D.J.; Berger, F.H.; Diamond, H.J.; Dykema, J.; Goodrich, D.; Immler, F.; Murray, W.; Peterson, T.; Sisterson, D.; Sommer, M.;et al. Reference Upper-Air Observations for Climate: Rationale, Progress, and Plans. Bull. Am. Meteorol. Soc. 2009, 90, 361–369.

Sherlock, V., Garnier, A., Hauchecorne, A., & Keckhut, P. (1999). Implementation and validation of a Raman lidar measurement of middle and upper tropospheric water vapor. *Applied Optics*, *38*(27), 5838-5850.

This project has received funding from the European Union's Horizon Europe Research and innovation program under Grant Agreement No 101056885

Thompson, G.; Scholzen, C.; O'Donoghue, S.; Haughton, M.; Jones, R.L.; Durant, A.; Farrington, C. On the fidelity of high-resolution numerical weather forecasts of contrail-favorable conditions. Atmos. Res. 2024, 311, 107663.

Vérèmes, H., Payen, G., Keckhut, P., Duflot, V., Baray, J.-L., Cammas, J.-P., Evan, S., Posny, F., Körner, S., & Bosser, P. (2019). Validation of the water vapor profiles of the raman lidar at the maïdo observatory (Reunion Island) calibrated with global navigation satellite system integrated water vapor. *Atmosphere*, *10*(11), 713.

Wolf, K., Bellouin, N., Boucher, O., Rohs, S., & Li, Y. (2023). Correction of temperature and relative humidity biases in ERA5 by bivariate quantile mapping : Implications for contrail classification. *EGUsphere*, *2023*, 1-38.

Yan, X., Wright, J. S., Zheng, X., Livesey, N. J., Vömel, H., & Zhou, X. (2016). Validation of Aura MLS retrievals of temperature, water vapour and ozone in the upper troposphere and lower–middle stratosphere over the Tibetan Plateau during boreal summer. *Atmospheric Measurement Techniques*, *9*(8), 3547-3566. https://doi.org/10.5194/amt-9-3547-2016

3. A Lidar validation campagne over SIRTA (TRACIS)

3.1. Introduction

Contrails and cirrus clouds are known to significantly affect the Earth's radiation budget, especially in regions of high air traffic density. However, the processes governing their formation and persistence remain insufficiently constrained, largely due to the lack of high-resolution water vapor measurements in the upper troposphere. Improving the characterization of water vapor in this region is therefore essential for better quantifying contrail radiative forcing and reducing associated uncertainties in climate models.

The TRACIS (Tropospheric Research campaign on Air humidity Content by IPRAL lidar at SIRTA) campaign was designed in this context. It was conducted at the SIRTA atmospheric observatory (Palaiseau, France), a site particularly well-suited for such a study due to its proximity to the heavily trafficked southern Parisian airspace, where contrail formation is frequent. Additionally, SIRTA is a GRUAN certified site where GRUAN treatments are applied. The campaign took place from 12 May to 12 June 2025 and was embedded in the BeCoM project, which aims to support sustainable aviation strategies through improved observation and modeling of contrail formation mechanisms.

TRACIS mobilized an unprecedented combination of observation systems, including the IPRAL Raman lidar, a suite of multi-payload radiosondes (M10, M20, and RS41), GNSS-based integrated water vapor retrievals, the HATPRO microwave radiometer, the MiniSAOZ UV-visible spectrometer, and thermal infrared (IR) imaging for nighttime cloud detection. A particular focus was given to nighttime operations to better capture the radiative impact of contrails under conditions where they are expected to have a stronger climate effect.

TRACIS campaign places special emphasis on the validation of the IPRAL water vapor algorithm (Alraddawi et al., 2025), the inter-comparison of radiosonde types under GRUAN protocols (Seidel at al., 2009) , and selected case studies of contrail events observed during the campaign. However any TRACIS results and scientific findings will be published in other separate reporting/publications but not in the current milestone. This document acknowledge the scientific collaboration and partners, then describes the instrumentation setup, and remind the associated scientific objectives, and end up with further administrative and scientific requirements.

This project has received funding from the European Union's Horizon Europe Research and innovation program under Grant Agreement No 101056885

3.2. Partners and Collaborations

The TRACIS campaign brought together a multidisciplinary team from French national research institutions, operational meteorological services, and private partners. It was coordinated by **LATMOS** and the **SIRTA atmospheric observatory**, with contributions structured around complementary expertise in remote sensing, radio-sounding, instrumentation, and contrail detection.

Strong coordination among the following partners ensured the successful deployment of a broad range of observational systems and enhanced the scientific impact of the TRACIS campaign—particularly in support of BeCoM's contrail-focused research goals

3.2.1. LATMOS

Leads: P. Keckhut, D. Alraddawi

LATMOS (CNRS-UVSQ-Sorbonne University) was responsible for the scientific coordination of the campaign and the processing of water vapor profiles from the IPRAL Raman lidar. The team also handled data from infrared cameras and the MiniSAOZ UV-visible spectrometer to support analyses of water vapor columns and cloud detection, according to the following scientitique issues:

- **IPRAL Raman lidar water vapor processing** (D. Alraddawi): Application and validation of Raman lidar WVMR retrievals (Alraddawi et al., 2025) on nighttime measurements.
- **IPRAL Elastic channel analysis** (F. Mandija, S. Khaykin): Retrieval of scattering ratio profiles from elastic signals to detect and characterize the vertical structure of clouds and contrails.
- **Thermal IR imaging** (A. Irbah): Processing of fisheye IR images to detect cirrus and contrail case studies
- **TCWV analyse** (A. Pazmino)**:** Analysis of MiniSAOZ total column water vapor observations, with comparison to GNSS-derived IWV over SIRTA during the TRACIS period.

3.2.2. SIRTA

Leads: J.-C. Dupont

The SIRTA observatory (IPSL) provided campaign logistics, ensured operational safety, managed data flow, and hosted the instruments. Three SIRTA teams contributed:

- **IPRAL Lidar Operation Team** (F. Lapouge, P .Delville)**:** Operated and maintained continuous nighttime and daytime lidar measurements for water vapor and cloud scene detection.
- **GRUAN team** (J.-C. Dupont. Et al.,): Managed multi-payload radiosonde launches (M10, M20, RS41), and applied the GRUAN correction chain (Dupont et al., 2020) to raw radiosonde data.
- **Data infrastructure team** (M. Drouin, A. Faucheux): Ensured centralized storage and partner access to campaign datasets.

3.2.3. Météo-France /CNRM

Lead: J. Capo

Provided technical support for RS41 radio-soundings, conducted training sessions for launch operations including the prior checks, contributed to the RS41 processing chain.

This project has received funding from the European Union's Horizon Europe
Research and innovation program under Grant Agreement No 101056885

3.2.4. Meteomodem private Co.

Leads: A. Farah, A. Poignard

Supplied M10 and M20 radiosondes, parachutes, and launch accessories. Meteomodem led multi-payload balloon launches and contributed to scientific analysis air temperature and relative humidity profiles and other sounding data. The campaign also supported GRUAN certification efforts for the M20 sonde, linked to A. Poignard's doctoral work.

3.2.5. Gordien Strato privat Co.

Leads: A. Hauchecorne, M. Martic, J . Porteneuve

Provided lidar expertise, oversaw hardware maintenance, and verified system performance throughout the campaign.

3.2.6. Réuniwatt private Co.

Leads: J. Hie, O. Liandrat

Delivered and supported fisheye infrared thermal camera (8–14 µm), enabling nighttime contrail detection via continuous sky temperature imaging. Camera installation and images storage and post-processing were performed in collaboration with LATMOS

3.3. Instrumentation setup

The TRACIS campaign deployed a comprehensive suite of active and passive instruments for high-resolution observations of water vapor and contrail-related parameters in the upper troposphere. The synergy between these ground-based remote sensing tools and in-situ measurements provided a robust framework for multi-variable analyses and cross-validation. Hereafter a brief reminder of them. We want just to highlight here that Radiosondes choice is based on availability of models which was sensitively limited by regional and political contexts (CFH radiosondes (Vomel et al., 2009) was not possible to use).

3.3.1. Lidar (IPRAL)

The IPRAL system is a multi-channel Raman lidar operated continuously at SIRTA (Photo 1). It retrieves profiles of water vapor mixing ratio (calibrated using the retrieval of Alraddawi et al., 2025), aerosol backscatter, and cloud presence from the boundary layer to the upper troposphere. For

This project has received funding from the European Union's Horizon Europe Research and innovation program under Grant Agreement No 101056885

TRACIS, the lidar operated both day and night, with nocturnal sessions specifically designed to capture contrail formation and evolution under radiatively active conditions.

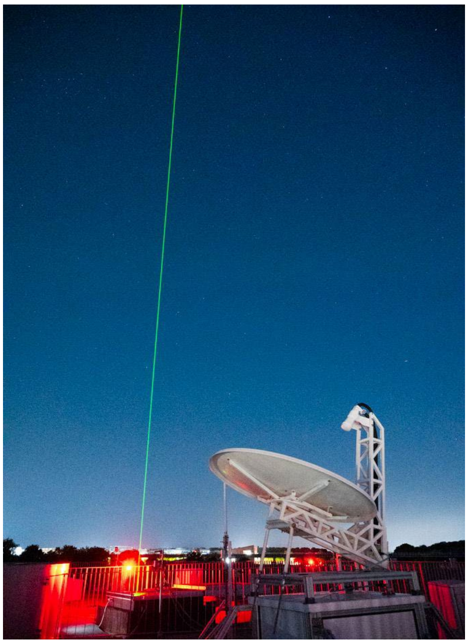

Photo 1. IPRAL Lidar at the SIRTA observatory during night observations.

3.3.2. Multi-Payload Radiosondes

Daily and nightly balloon launches were performed using three types of radiosondes:

- **M10 and M20** (Meteomodem): M20 sondes (Photo) were tested under TRACIS as part of their GRUAN certification process.
- **RS41** (Vaisala): Provided temperature, humidity, and pressure profiles with high vertical resolution. To be additionally treated using GRUAN processing

Each launch combined up to three sondes on a single balloon (Figure 1), enabling inter-comparison and redundancy. We ended up having about 20 collocated profiles of atmospheric variables (including wind information, air temperature, relative humidity at two launch hour: day time: 9h30 and night time: 21h30 UT, Table 1 is summarizing the launch dates, which belong to: M10, M20, RS41, M10 GRUAN treated (SIRTA site), along with the coincident ERA5 profile of the same radiosondes launch hour (Hersbach et al., 2023), in addition to few coincidence to M10 GRUAN treated (Trappes site: TRP) .Data were processed and archived on the Meso Center platform.

This project has received funding from the European Union's Horizon Europe Research and innovation program under Grant Agreement No 101056885

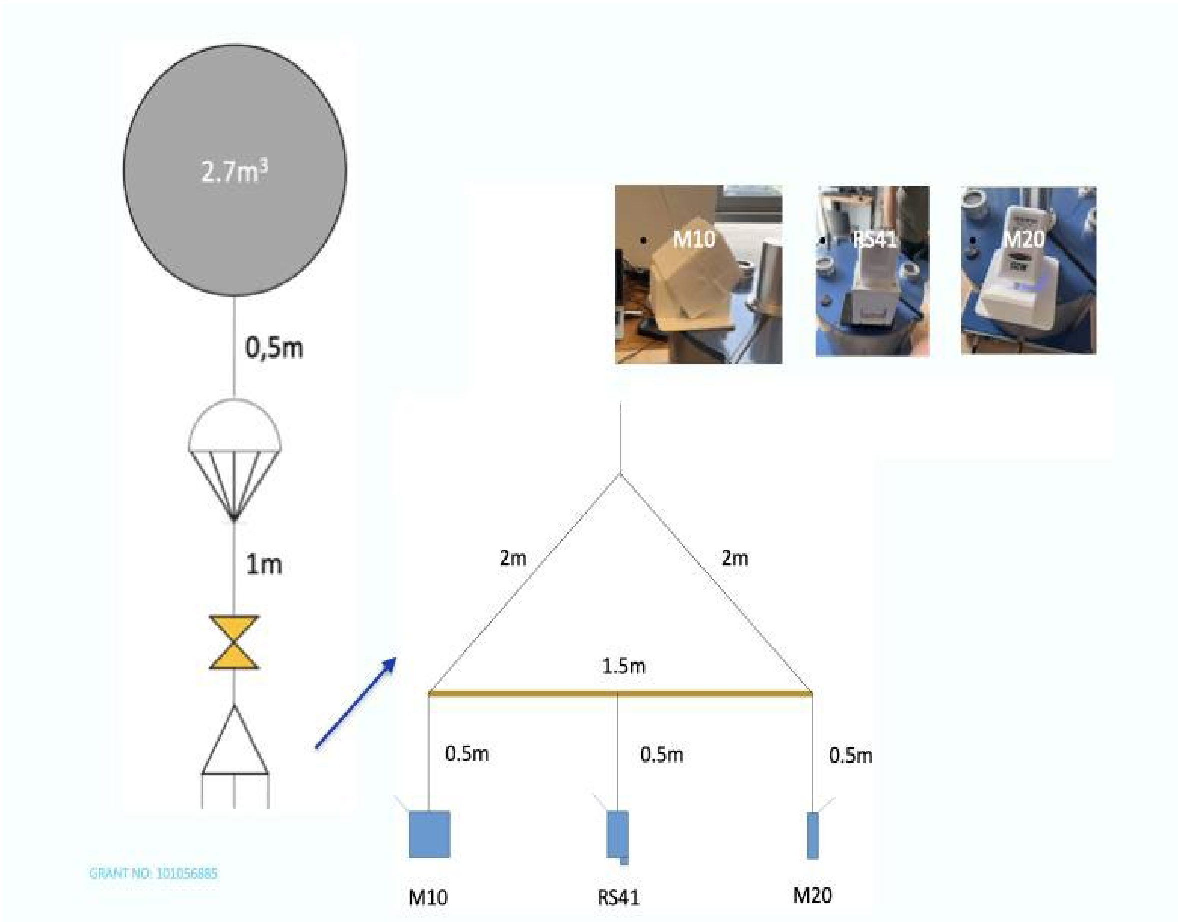

Table 1: Effective dates and hours of radiosondes flights during TRACIS campaign

Observation dates	Uinversal Time	Lidar coincidence
14/05	(12h00/21h00)	Yes
15/05	(12h00/21h00)	Yes
16/05	(21h00)	Yes
19/05	(09h30)	-
20/05	(09h30)	-
22/05	(9h30/21h00)	Yes
23/05	(9h30/21h00)	Yes
26/05	(17h30)	-
28/05	(9h30/21h30)	Yes
02/06	(21h30)	Yes
03/06	(21h30)	Yes
05/06	(9h30)	-
11/06	(9h30/21h30)	Yes

This project has received funding from the European Union's Horizon Europe Research and innovation program under Grant Agreement No 101056885

Observation dates	Uinversal Time	Lidar coincidence
12/06	(21h15)	Yes

Figure 14. Schematic representation of flight with triple payload configuration (M10, M20, and RS41), carried on a stratospheric helium ballon, equipped with parachute for safer descending.

3.3.3. GNSS Receiver

A ground-based GNSS station operated at SIRTA provided continuous integrated water vapor (IWV) measurements (Bock et al., 2013), supporting the validation of lidar and radiosonde humidity retrievals.

3.3.4. Microwave Radiometer (HATPRO)

The HATPRO (Humidity And Temperature PROfiler) is a passive microwave radiometer, operated at SIRTA since 2010, delivered IWV, along with humidity and temperature profiles. These measurements were used to monitor the atmospheric background state during lidar operations. Enabling real-time monitoring of temperature and humidity fields, as well as water vapor and liquid water content.

3.3.5. MiniSAOZ UV-VIS Spectrometer

MiniSAOZ measured total column water vapor and ozone using zenith-sky observations. It provided independent integrated humidity estimates, especially useful for cross-validating lidar and GNSS retrievals under clear-sky conditions (Bock et al., 2013; Tulet et al., 2024)

3.3.6. Infrared Thermal Camera

Additional fisheye IR thermal camera (8–14 µm) from Réuniwatt co. is installed to monitor sky temperatures and detect thermal signatures of cirrus and contrails, especially at night. Images were acquired continuously with 1-minute temporal resolution, to be post-processed for contrail tracking.

3.4. TRACIS Scientific Objectives

The TRACIS campaign was designed to address key scientific challenges related to water vapor variability and its role in contrail and cirrus cloud formation in the upper troposphere. The campaign's scientific objectives were aligned with the goals of the 1st work package WP1 of the BeCoM project: to improve our understanding of the microphysical and radiative processes governing contrail formation and evolution; and to enhance the quality of upper-tropospheric humidity measurements essential for contrail-aware aviation policy and modeling. TRACIS focused on the following priorities:

I. Validation of Raman Lidar Water Vapor Profiles

Apply and validate the recently developed IPRAL Raman lidar retrieval algorithm for water vapor mixing ratio (WVMR) under nocturnal conditions (Alraddawi et al., 2025). particularly in the upper troposphere (above 8 km), w.r.t radiosonde and ERA5 model data. Figure 15 shows an example of cruise altitude part (between 7 and 11 km) of water vapor profiles recorded by the different sources during one night radiosondes

launch on 28/05/2025. This example can show clearly how close the observations by radiosondes, Lidar and ERA5 are, and how challenging is to evaluate and to enhance the current ability to describe fairly the humidity at these altitudes, Lidar seems to detect more humid content than all other

This project has received funding from the European Union's Horizon Europe Research and innovation program under Grant Agreement No 101056885

instruments, all this is well consistent with our very first statistical inter comparison (Alraddawi et al., 2025). More statistical results are to be communicated over upcoming publications.

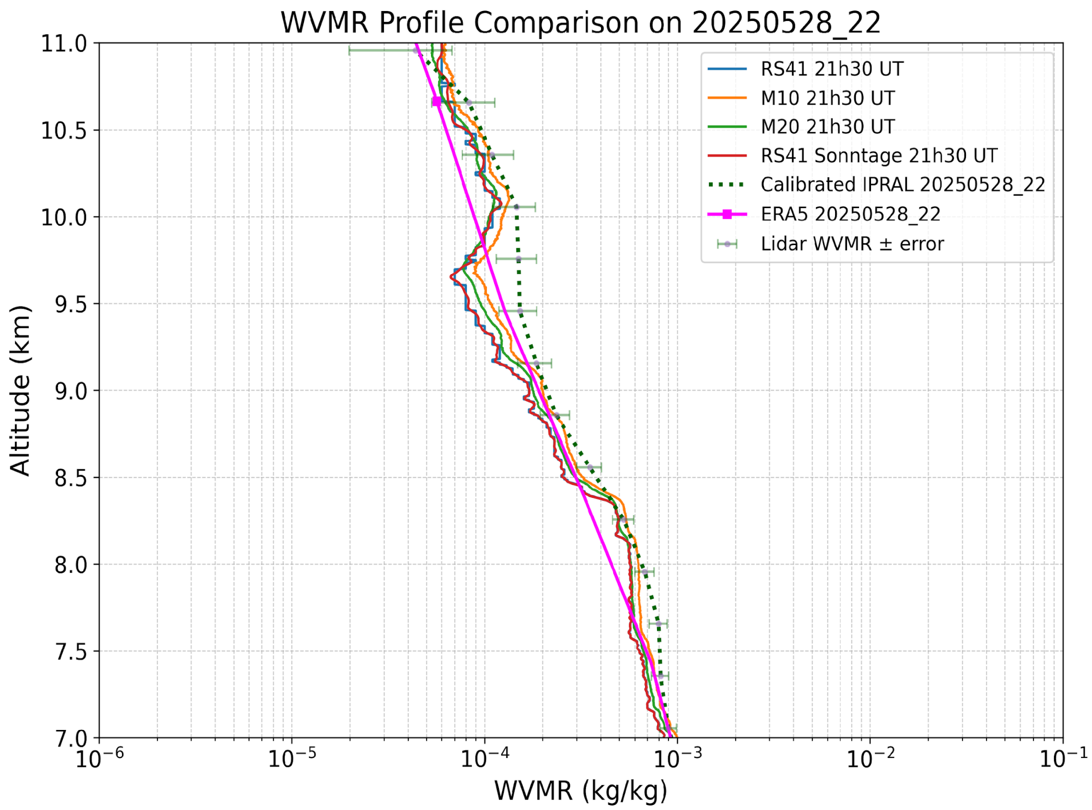

Figure 15. Example of Raman lidar WVMR profile (noted green, and horizontal lines are the associated error) along with radiosondes ones (M10: orange, M20: green, RS41 operational: blue and Sonntag calculated: red) during the night radiosondes launch of 28/05/2025, ERA5 WVMR profile for the same launch hour is marked in

3.4.1. Lidar VS ERA5

The atmospheric re-analysis ERA5 WVMR hourly product (Hersbach et al., 2023) profiles coincident to Radiosondes launch hours during TRACIS are analysed w.r.t Lidar same hours, we finally got 10 nocturnal hours to be analysed. Our results report a clear ERA5 dry bias w.r.t Lidar, more pronounced since 8.5 km and upwards, with median relative bias which reaches about 30% for altitudes < 10 km and up to 40% upwards (Figure 16).

3.4.2. Lidar VS M10

The atmospheric M10 radiosonde WVMR profiles coincident to lidar operation hours during TRACIS are analysed, we finally got 9 nocturnal hours to be compared. Our results report a small dry bias w.r.t Lidar, more pronounced since 9 km and upwards, with median relative bias which reaches about 20% (Figure 17).

This project has received funding from the European Union's Horizon Europe Research and innovation program under Grant Agreement No 101056885

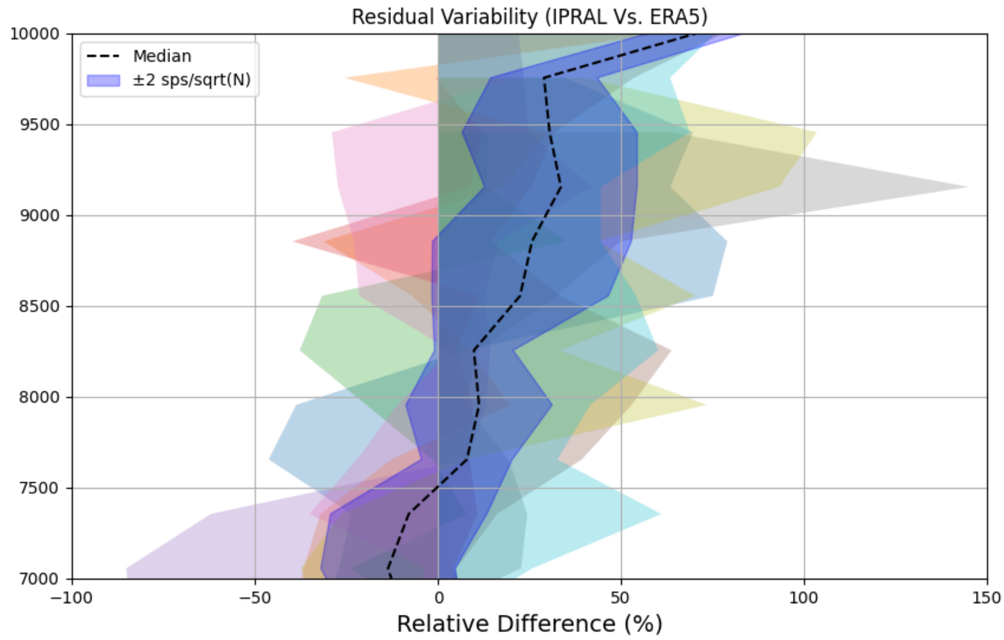

Figure 16. Residual Variability of ERA5 & Lidar hours WVMR profiles coincident TRACIS Radiosondes launches, Median LIDAR Bias w.r.t ERA5 is shown in dashed black line, shaded purple is the 2 pseudo standard deviation error of this bias which refers to the 95% error confidence level, study is carried out over 10 profiles distinguished by colorful shades..

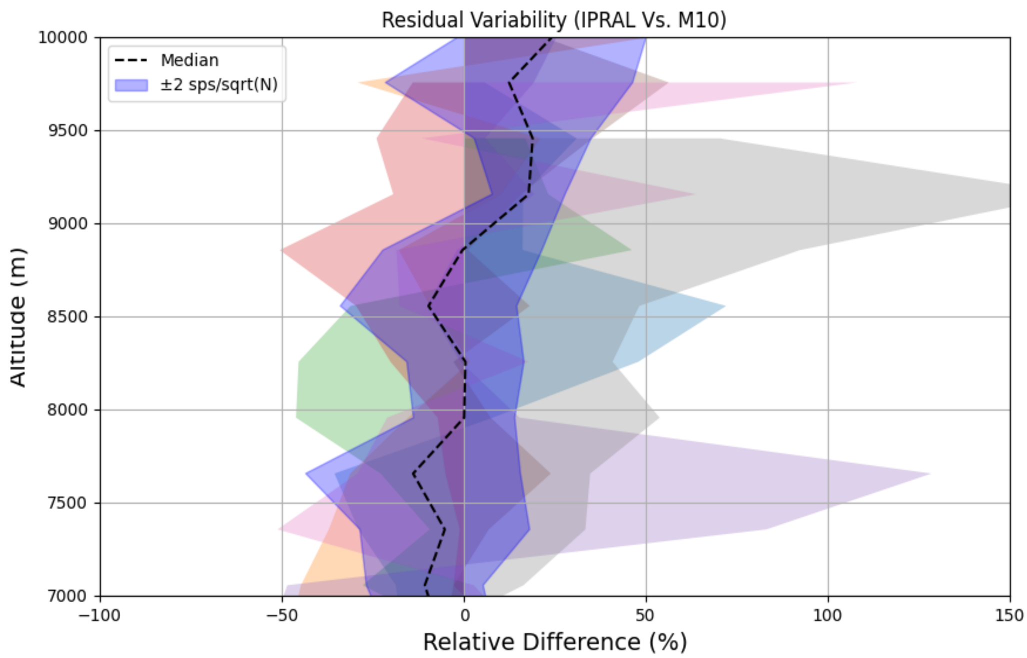

Figure 17. Residual Variability of M10 radiosonde & Lidar hours WVMR profiles coincident TRACIS Radiosondes launches, Median LIDAR Bias w.r.t M10 is shown in dashed black line, shaded purple is the 2 pseudo standard deviation error of this bias which refers to the 95% error confidence level, study is carried out over 9 profiles distinguished by colorful shades.

3.4.3. Lidar VS M20

This project has received funding from the European Union's Horizon Europe Research and innovation program under Grant Agreement No 101056885

The atmospheric M20 radiosonde WVMR profiles coincident to lidar operation hours during TRACIS are analysed, we finally got 9 nocturnal hours to be compared. M20 is the new version of M10 radiosondes to be qualified during this campaign and upcoming one, in the objective to get the GRUAN certification for this dataset. Our results report a small dry bias w.r.t Lidar, more pronounced since 8.5 km and upwards, with median relative bias which reaches about 30% (Figure 18).

3.4.4 Lidar VS RS41

The atmospheric (Vaisala co.) RS41 radiosonde WVMR profiles coincident to lidar operation hours during TRACIS are analysed, we finally got 10 nocturnal hours to be compared. RS41 is the most recent version of Vaisala radiosondes to be qualified during this campaign and upcoming one, it was also analyzed within the SHC (wet room GRUAN test) in the objective to get GRUAN treatment for this dataset, upcoming reports /articles will analyse the GRUAN processed dataset of RS41 but the following results concern the RS41 without GRUAN treatment. We report a small dry bias w.r.t Lidar, more pronounced since 8.5 km and upwards, with median relative bias which reaches about 30% (Figure 19).

II. Characterization of Total Integrated Humidity Content TCWV

As a second validation to lidar measurements: Compare total column water vapor (TCWV) derived from MiniSAOZ and GNSS with integrated Radiosondes/lidar profiles. As a first investigation SAOZ and GNSS integrated water vapor (IWV=TCWV) qualities (which are available

This project has received funding from the European Union's Horizon Europe Research and innovation program under Grant Agreement No 101056885

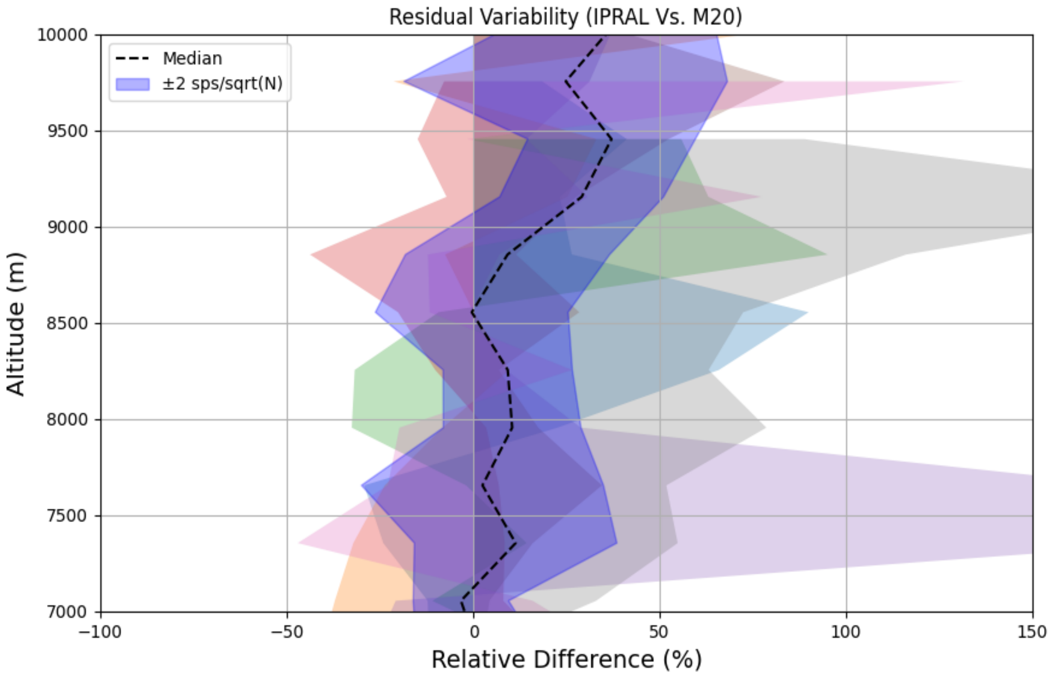

Figure 18. Residual Variability of M20 radiosonde & Lidar hours WVMR profiles coincident TRACIS Radiosondes launches, Median LIDAR Bias w.r.t M20 is shown in dashed black line, shaded purple is the 2 pseudo standard deviation error of this bias which refers to the 95% error confidence level, study is carried

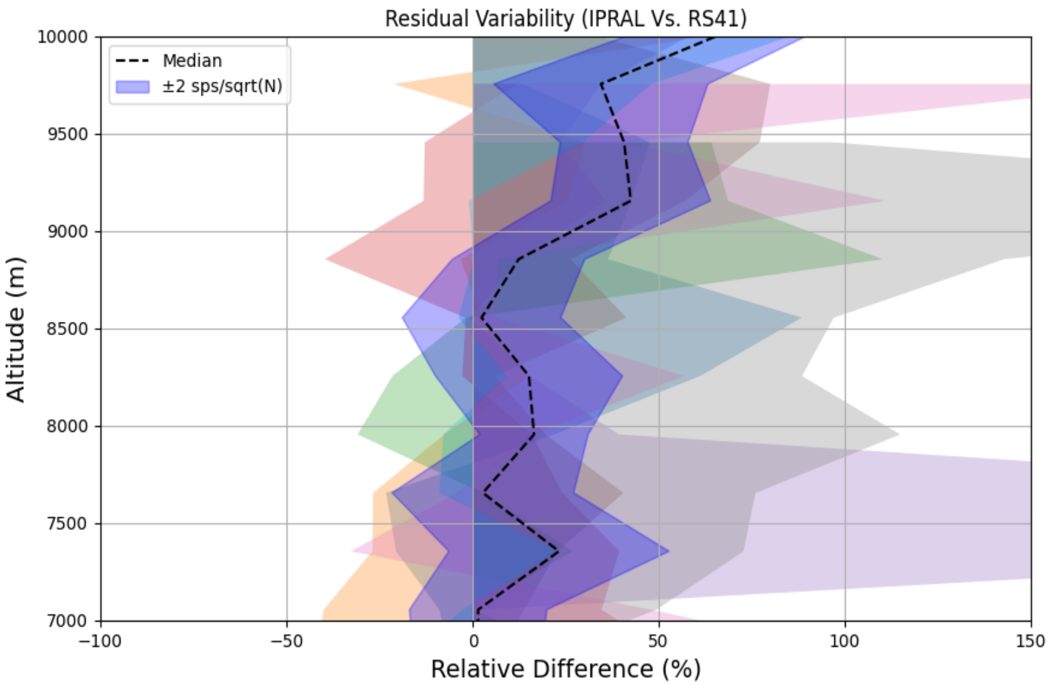

Figure 19. Residual Variability of RS41 radiosonde & Lidar hours WVMR profiles coincident TRACIS Radiosondes launches, Median LIDAR Bias w.r.t M20 is shown in dashed black line, shaded purple is the 2 pseudo standard deviation error of this bias which refers to the 95% error confidence level, study is carried out over 10 profiles distinguished by colorful shades.

with some delay post treatment) were compared over the first 20 days of TRACIS and show well

This project has received funding from the European Union's Horizon Europe Research and innovation program under Grant Agreement No 101056885

consistency (Figure 20). The next step will be to obtain Lidar-derived TCWV for comparison with these datasets.

III. Contrails and Cirrus Detection and Analysis

The synergistic use of remote sensed and in-situ observations, enabled to:

- Build a high-resolution, multi-dimensional picture of water vapor and cloud properties during contrail events. and hence to detect and document contrail day/night events (assured by thermal infrared sky imaging + IPRAL Lidar (using backscattered Raman signals / Rayleigh scattering ratio) + ADS-B system for aviation information + GNSS and radiosonde datasets. And hence to supply future assimilation of UT altitudes humidity measurements into new atmospheric and climate models. All this. Is possible using IR imager which allows to follow the visual evolution of the contrails (its displacement and horizontal extension) while the ADS-B system allows to associate the identification of the contrail, the aircraft having induce the contrails, and its characteristics like the cruise altitude, the trajectory and the type of the plane.
- Investigate the vertical structure, persistence, and radiative characteristics of contrails, with a focus on nighttime events when radiative effects are more pronounced.

This objective results will not be introduced within the current deliverable. But to be published at

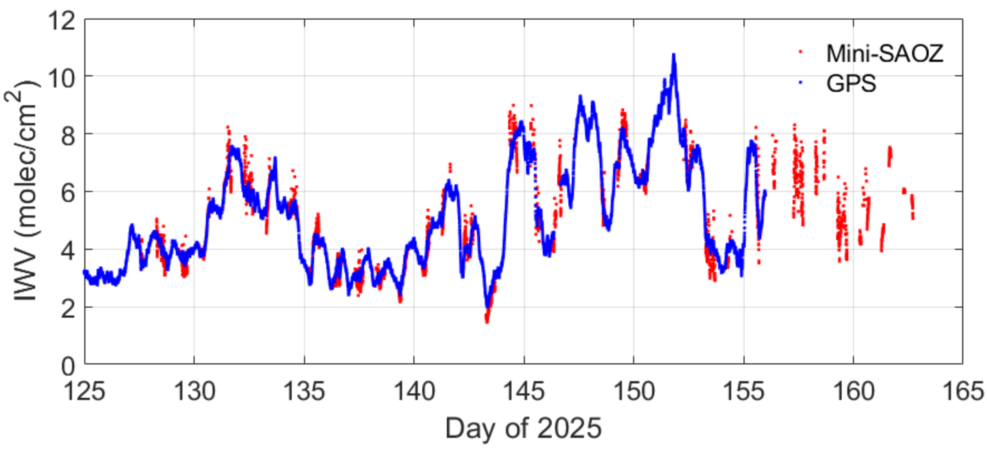

Figure 20. Integrated Water Vapor column density (molec/cm^2) over SIRTA during TRACIS, the recent GPS data

the upcoming article which summarize the whole TRACIS campaign results.

IV. Evaluation and Inter-comparison of Radiosonde Systems

- Perform multi-payload balloon launches (M10, M20, RS41) to inter-compare sensor performance under controlled conditions. The examined variables are: Air temperature, relative humidity %. Most analyses show that M10 has a wet bias w.r.t both M20 & RS41. Figure 21 shows an example of Air temperature profiles (left) and Relative humidity ones (right) by M10, M20, RS41 in green, orange, blue respectively.
- Support the GRUAN certification process for the M20 sonde through statistical analysis and cross-validation with lidar and GNSS data (under analyse now).

This objective results are analyzed by the Ph.D student Alexis Poignard, which is running the statistical comparisons now.

This project has received funding from the European Union's Horizon Europe Research and innovation program under Grant Agreement No 101056885

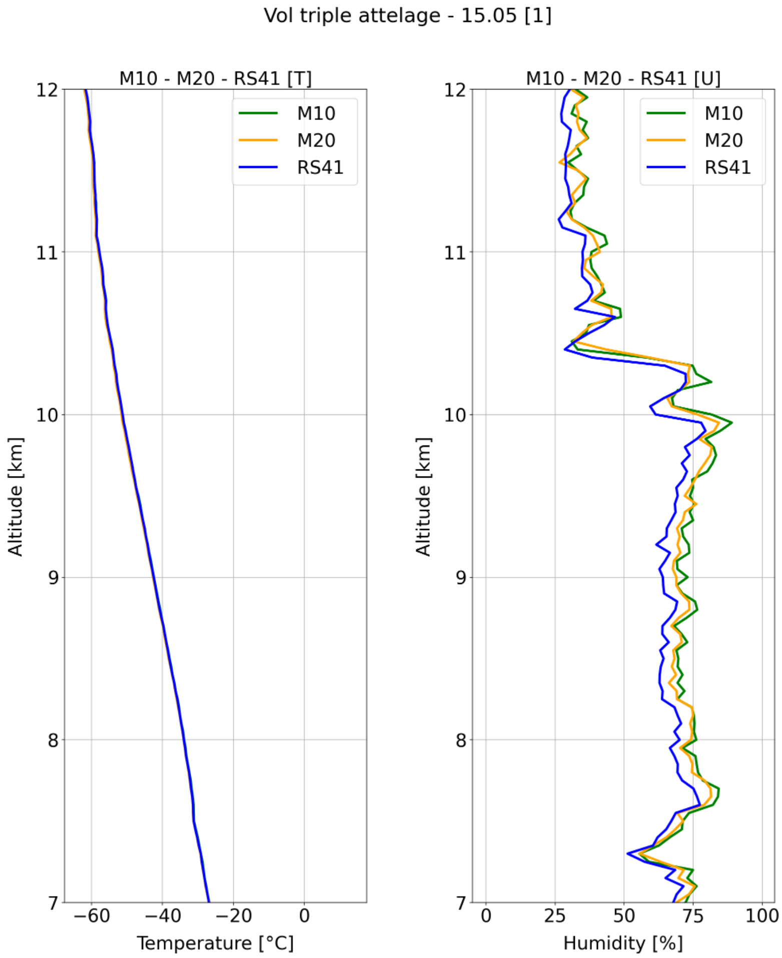

Figure 21. Vertical profiles of M10, M20, RS41 air temperature °c (left) and relative humidity % (right) for the nocturnal launch of 15/05/2025.

3.5. Radiosondes Quality Check

3.5.1. Sensor Conditioning and GRUAN humidity room Check

To ensure traceability and high data quality in line with the GRUAN (GCOS Reference Upper-Air Network) guidelines, all radiosondes launched during TRACIS underwent systematic pre-launch procedures. To meet GRUAN standards, each radiosonde is placed in a **humidified and ventilated chamber** before launch. This procedure uses sterilized water to create a **homogeneous environment** where the relative humidity reaches 100%. It allows verification of the sensor's responsiveness to **saturation conditions**, This step helped detecting potential sensor contamination or slow response

This project has received funding from the European Union's Horizon Europe Research and innovation program under Grant Agreement No 101056885

time, and hence ensuring reliable measurements of upper-tropospheric humidity (Dupont et al.,

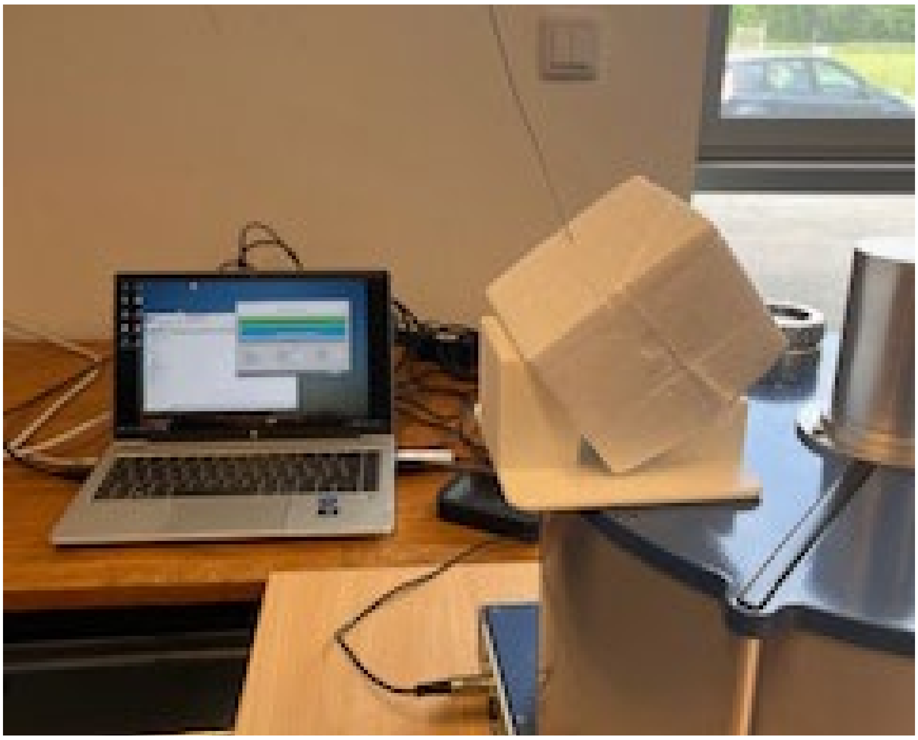

Photo 2. GRUAN humid room check along with the connected logiciel to record examined sounding data.

2020), it has to be done few hours before the flight.

3.5.2. Before Launch procedures

Radiosondes were activated and ventilated for a minimum of 30 minutes before launch to stabilize temperature and pressure readings and avoid lag errors. Procedure includes Power on the radiosonde, verify the transmission frequency, perform the ground-check, place the sonde outdoors, and confirm proper communication.
All sondes were individually labeled and associated with metadata including type (M10, M20, RS41), calibration status, and launch time. Data was stored following GRUAN metadata protocols for future reprocessing and certification.
Multi-payload balloon configuration is adopted (M10+M20+RS41) to enable equal conditions and to help avoid systematic biases. All to contribute to the validation and GRUAN certification of the newer sonde (M20 model).

These practices, compliant with GRUAN requirements, enhanced the reliability and traceability of the radiosonde dataset collected during the TRACIS campaign.

3.6. Administrative issues

3.6.1. Air Traffic Safety procedures

Given SIRTA's location in controlled airspace, each balloon launch requires:

- **Prior authorization** from the French Civil Aviation Authority (DSAC-Nord), including flight details and payload description (Planned launch dates and times (UTC), Launch site

This project has received funding from the European Union's Horizon Europe
Research and innovation program under Grant Agreement No 101056885

coordinates, Contact details of the responsible person, Payload description, Maximum balloon altitude, ascent/descent rates, and recovery procedure)

- **Pre-launch notifications** to nearby airports and military airspace controllers, both at least one working day in advance and shortly before launch.

These steps ensure compliance with **air traffic regulations** and secure flight conditions. Here after the effective flight dates according to the meteorological and administrative feasibility.

3.6.2. Staff acknowledgments

This campaign benefited from the access to the National Instrument Moyens Mobiles which is part of research infrastructure « ACTRIS-FR ». We would like to thank SIRTA observatory staff (Photo 3), and Meteomodem co. staff to be actively available during this campaign, especially during the night

Photo 3: Snapshots of in place daytime/nighttime ballon sounds launches with the amazing staff.

shifts, special thanks to A. Faucheux, MA. Drouin, and A. Poignard

3.7. Conclusions and perspectives

The TRACIS (Tropospheric Research campaign on Air humidity Content by IPRAL lidar at SIRTA) intensive field campaign took place at SIRTA (43.9°N 2.2°E). Its primary objective was to improve water vapor profiling in the upper troposphere, a key region for ice cloud formation and contrail development. Referenced to be part of NDACC observation sites, SIRTA was strategically chosen due to its location in the densely trafficked southern Parisian airspace, where frequent aviation activity increases the likelihood of contrail and cirrus cloud formation. Since the radiative impact of contrails is expected to be more pronounced at night, the

This project has received funding from the European Union's Horizon Europe Research and innovation program under Grant Agreement No 101056885

campaign included both daytime and systematic nocturnal measurements. Conducted within the framework of the European BeCoM project, TRACIS brought together a comprehensive set of ground-based remote sensing and in situ observations of thermodynamic conditions: Raman lidar (IPRAL), multiple-payload radiosondes (M10, M20, RS41), GNSS, HATPRO, MiniSAOZ, and infrared (IR) thermal imaging. It makes use also of the ADS-B aircraft tracking in identifying Contrails events. A central goal was to validate the IPRAL Raman lidar water vapor retrieval algorithm developed in the framework of BeCOM project and published (Alraddawi et al. 2025). The campaign also contributed to GRUAN and national observation programs. Within the current section, we tried to outline the campaign organization issues: including the collaborations, the instrumental setup, the
scientific objectives, requirements and few first results. Our results confirm that LiDAR instruments provide a more accurate characterization of upper troposphere humidity than any other available technique. All Radiosondes showed a dry bias w.r.t Lidar ranged from 10 % to 30% at the UT altitudes. The TRACIS campaign also confirmed the ERA5 dry bias previously reported by the WP1 (Alraddawi et al., 2025) and other partners staffs.
The contrails nocturnal cases studies of TRACIS and other final results are to be reported within an upcoming paper.
However, the next section will introduce a preliminary evaluation of contrail super-saturation coefficients using ground-based instruments, it was performed via simultaneous observations over Clermont-Ferrand, France; one of the sites involved in the BeCoM project. In this site we were able to be deployed simultaneously daytime ground-based LIDAR, an all-sky camera, the ADS-B aircraft tracking, and the ECMWF-ERA5 reanalysis. We were able to identify one period on June 2nd, 2023, when all the instruments operate nominally, without low clouds that would have masked the potential contrails.
The cases analyzed are described in the following section based on a publication that has now been accepted and published (Diarra et al., 2026). This study was conducted within the framework of Sidy Diarra's PhD thesis, funded by the BeCoM project.

3.8. References

Alraddawi, D.; Keckhut, P.; Mandija, F.; Sarkissian, A.; Pietras, C.; Dupont, J.-C.; Farah, A.; Hauchecorne, A.; Porteneuve, J. Calibration of Upper Air Water Vapour Profiles Using the IPRAL Raman Lidar and ERA5 Model Results and Comparison to GRUAN Radiosonde Observations. Atmosphere 2025, 16, 351. https://doi.org/10.3390/atmos16030351

Seidel, D.J.; Berger, F.H.; Diamond, H.J.; Dykema, J.; Goodrich, D.; Immler, F.; Murray, W.; Peterson, T.; Sisterson, D.; Sommer, M.; et al. Reference Upper-Air Observations for Climate: Rationale, Progress, and Plans. Bull. Am. Meteorol. Soc. 2009, 90, 361–369.

Dupont, J.-C.; Haeffelin, M.; Badosa, J.; Clain, G.; Raux, C.; Vignelles, D. Characterization and corrections of relative humidity measurement from Meteomodem M10 radiosondes at midlatitude stations. J. Atmos. Ocean. Technol. 2020, 37, 857–871.

Vömel, H.; David, D.E.; Smith, K. Accuracy of tropospheric and stratospheric water vapor measurements by the cryogenic frost point hygrometer: Instrumental details and observations. *J. Geophys. Res. Atmos.* **2007**, *112*. ⟨10.1029/2007JD008698⟩.

Hersbach, H., Bell, B., Berrisford, P., Biavati, G., Horányi, A., Muñoz Sabater, J., Nicolas, J., Peubey, C., Radu, R., Rozum, I., Schepers, D., Simmons, A., Soci, C., Dee, D., Thépaut, J-N. (2023): ERA5 hourly data on pressure levels from 1940 to present. Copernicus Climate Change Service (C3S) Climate Data Store (CDS), (Accessed on DD-MMM-YYYY). ⟨ 10.24381/cds.bd0915c6⟩

Bock, O., Bosser, P., Bourcy, T., David, L., Goutail, F., Hoareau, C., Keckhut, P., Legain, D., Pazmino, A., Pelon, J., Pipis, K., Poujol, G., Sarkissian, A., Thom, C., Tournois, G., and Tzanos, D.: Accuracy assessment of water vapour measurements from in situ and remote sensing techniques during the DEMEVAP 2011 campaign at OHP, Atmos. Meas. Tech., 6, 2777–2802, https://doi.org/10.5194/amt-6-2777-2013, 2013.

Tulet, P., Van Baelen, J., Bosser, P., Brioude, J., Colomb, A., Goloub, P., Pazmino, A., Portafaix, T., Ramonet, M., Sellegri, K., Thyssen, M., Gest, L., Marquestaut, N., Mékiès, D., Metzger, J.-M., Athier, G., Blarel, L., Delmotte, M., Desprairies, G., Dournaux, M., Dubois, G., Duflot, V., Lamy, K., Gardes, L., Guillemot, J.-F., Gros, V., Kolasinski, J., Lopez, M., Magand, O., Noury, E., Nunes-Pinharanda, M., Payen, G., Pianezze, J., Picard, D., Picard, O., Prunier, S., Rigaud-Louise, F., Sicard, M., and Torres, B.: MAP-IO: an atmospheric and marine observatory program on board *Marion Dufresne* over the Southern Ocean, Earth Syst. Sci. Data, 16, 3821–3849, httpsinstallées sur la bateau Marion Dufresne://doi.org/10.5194/essd-16-3821-2024, 2024.

Diarra, S., J.-L. Baray, N. Montoux, P. Fréville, F. Peyrin, P. Cacault, W. Boucher, P. Keckhut, Combining LIDAR, all-sky camera, and ECMWF-ERA5 reanalysis to investigate contrail formation and evolution over Clermont-Ferrand, France on June 2, 2023, Atmospheric Research, Volume 329, 108500, https://doi.org/10.1016/j.atmosres.2025.108500, 2026

4. Combining LIDAR, all-sky camera, and ECMWF-ERA5 reanalysis to investigate contrail formation and evolution over Clermont-Ferrand on June 2, 2023

Sidy Diarra[1,2], Jean-Luc Baray[1,3], Nadège Montoux[1], Patrick Fréville[3], Frédéric Peyrin[3], Philippe Cacault[3], William Boucher[1], Philippe Keckhut[2]

[1]LaMP, UMR6016, CNRS, Université Clermont Auvergne, Clermont-Ferrand, 63100, France
[2]LaTMOS, UMR8190, CNRS, Université Versailles St Quentin, Guyancourt, 78280, France
[3]OPGC, UAR833, CNRS, Université Clermont Auvergne, Clermont-Ferrand, 63100, France

Correspondence to: Sidy Diarra (sidy.diarra2@doctorant.uca.fr) and Jean-Luc Baray (J.L.Baray@opgc.fr)

Abstract. Contrails formed by aircrafts in the upper troposphere contribute to anthropogenic climate forcing. However, the conditions driving their formation and persistence remain incompletely understood. This study combines an ACTRIS/EARLINET ground-based LIDAR, all-sky camera imagery, ADS-B aircraft tracking, and ECMWF-ERA5 reanalysis to analyse contrails formation and evolution over Clermont-Ferrand, France, on June 2, 2023. Twelve contrails are documented throughout the day, including persistent and non-persistent contrails. Persistent contrails are observed under ice-supersaturated conditions (relative humidity with respect to ice, RHi > 105 %) and at temperatures between 217–223 K, as well as different aircraft type and engine configuration. Non-persistent contrails are associated with lower RHi mostly below 90 %, and colder temperatures (near 214 K). The horizontal contrail widths range from 0.53 ± 0.10 to 1.60 ±0.44 km (all-sky camera estimation) and 0.35 ±0.14 to 1.90 ±0.32 km (LIDAR estimation), and vertical extents varied from 340 ±10 to 440 ±20 m. The maximum contrail observation duration by camera is 180 minutes. The study highlights the potential of ground-

based remote sensing for contrail monitoring and the need for further research on mitigation strategies.

4.1. Introduction

Aircraft can induce the formation of ice clouds in the upper troposphere, typically between 8 and 13 km in altitude, known as contrails (condensation trails). Following their formation, they may develop into visually resembling natural cirrus clouds with comparable microphysical properties (Heymsfield et al., 2010). The temperature, humidity, and wind patterns have an impact on this process. Contrails reflect daytime solar radiation and also trap outgoing terrestrial radiation. On average, the warming effect is dominant to the cooling effect, resulting in a positive contribution to global warming (Lee et al., 2021). In addition, contrails affect the global increase in cloud cover (Kärcher, 2018; Sanogo et al., 2024) constituting an additional anthropogenic effect impacting the radiative balance of the Earth (Kärcher, 2018; Lee et al., 2021; Schumann et al., 2021).
The net radiative forcing of contrails depends on factors such as atmospheric conditions, but also as age and optical properties of the contrails. The mean estimate of their effect on global climate remains uncertain. In 2018, the radiative forcing of contrails was estimated in a range between 17 and 98 mW m^{-2} (Lee et al., 2021). In the future, an increase in radiative forcing is expected. It could reach 160 mW m^{-2} by 2050 (Singh et al., 2024). The non-CO_2 radiative forcing attributed to aviation exceed that of CO_2 emissions, which is estimated between 31 and 38 mW m^{-2} (Lee et al., 2021). Another study estimates that the global annual mean radiative forcing attributable to contrail cirrus is three times larger than the radiative forcing from aviation's cumulative CO_2 emissions (Teoh et al., 2024). The discrepancy between these various estimates of the direct and indirect impacts is due to the different approaches and assumptions adopted in the respective studies.
This topic is currently of interest to the scientific community because of the urgent need to understand and mitigate the climate impacts of aviation. Several recent and current international projects aim to study and predict contrail formation, and to develop mitigation strategies to reduce their climatic impact. Notable examples of these initiatives include:

- BECOM (Better Contrail Mitigation): This project proposes to develop strategies to mitigate the formation and impact of contrails. By combining advanced atmospheric modelling with real-world flight data, it aims to identify optimal flight paths and operational practices that minimize contrail formation (https://becom-project.eu/).
- CICONIA (Cracking the non-CO_2 conundrum): This project proposes to quantify the climate impact of the non-CO_2 emissions and develop mitigation strategies that can be integrated into air traffic management systems (https://www.sesarju.eu/news/ciconia).
- CONTRAILS: Led by the German Meteorological Service (DWD), this project focuses on improving the scientific understanding of contrail formation and their climate effects (https://www.dwd.de/EN/research/projects/contrails/contrails_node.html).
- CLIMAVIATION: This French initiative brings together researchers, industry experts, and policymakers to tackle the climate challenges posed by aviation. The project Climaviation focuses on developing strategies that address both CO_2 and non-CO_2 emissions, including contrails to achieve a more sustainable aviation sector (https://climaviation.fr/en/).

The contrail formation is intrinsically linked to the emission of water vapor and aerosols by aircraft engines. Atmospheric conditions also play a significant role: for instance, contrails are more likely to form in the upper troposphere in cold and humid air. Meanwhile, aircraft-

This project has received funding from the European Union's Horizon Europe
Research and innovation program under Grant Agreement No 101056885

specific factors, such as the type of fuel used and the efficiency of the engine, also influence contrail formation. Engines that emit more water vapor and particles, or those that are less efficient, are more likely to produce contrails. This phenomenon is governed by the Schmidt-Appleman criterion, which outlines the specific conditions required for contrail formation. This criterion considers both atmospheric and aircraft-specific parameters (Heymsfield et al., 2010) and can be used in theoretical contrail formation prediction models (Sun and Roosenbrand, 2023).

For contrails to persist beyond the initial vortex phase, during which wake turbulence and vortices disturb the newly formed contrail, the ambient environment must be supersaturated with respect to ice (RHi > 100%) (Iwabuchi et al., 2012). A contrail is generally classified as persistent if it remains visible for more than 10 minutes (Kärcher, 2018).

In most cases, contrails dissipate quickly due to adiabatic heating, which induces sublimation of ice particles (Lewellen and Lewellen, 2001; Unterstrasser et al., 2017). This process typically occurs when the surrounding air is not sufficiently humid to maintain the ice crystals.

However, under certain atmospheric conditions, contrails can persist and even spread to form extensive cirrus-like clouds. This occurs when the atmosphere is supersaturated with respect to ice (RHi > 100%), (Jensen et al., 1998). The statistical analyses of cirrus clouds observed by lidar revealed different clusters based on their morphological behavior (Keckhut et al., 2006; Mandija et al., 2024). In addition to standard thick clouds (2-3 km), some thinner clouds (< 1 km) are detected quite frequently, with an occurrence of 30%, including potentially contrails and cirrus. Although research on the microphysical properties of young contrails remains limited, several airborne measurement campaigns have nonetheless provided valuable initial insights into their macroscopic characteristics:

- FIRE (First ISCCP Regional Experiment): Conducted in Kansas, USA, during the fall of 1991, this campaign focused on studying cloud properties and provided early data on contrail formation and evolution (Han et al., 1995).
- ARM (Atmospheric Radiation Measurement): Held in Oklahoma, USA, in April 1994, this campaign included in situ measurements and contrail spatial dimensions (Sassen, 1997).
- CONCERT (Contrail and Clouds Experiment): Two campaigns conducted in the fall of 2008 and 2011 provided further data on contrail characteristics, including detailed measurements of microphysical properties (Chauvigné et al., 2018; Voigt et al., 2010).
- ML-CIRRUS (Midlatitude Cirrus experiment): Conducted over southern Germany in March and April 2014, this campaign was among the first scientific missions to utilize the HALO Research Aircraft. It aimed to achieve six main objectives, including the investigation of differences between anthropogenic and natural cirrus (Voigt et al., 2017).

These campaigns have contributed to our understanding of contrail formation and persistence by offering in situ measurements that complement satellite observations. Additionally, ground-based instruments, such as LIDAR and sky-camera, are used for the validation of contrail models (Mannstein et al., 2010; Rosenow et al., 2023; Schumann et al., 2013).

In particular, ground-based cameras offer a low-cost alternative to satellites. They provide high temporal and spatial resolution, enabling continuous monitoring of the formation and evolution of young contrails. These cameras are also capable of detecting optically thin contrails, which can be missed by other observation methods (Mannstein et al., 2010).

The present study part of the work package Operational and new measurements and characterization of the European project BECOM. Its aim is to document the observation and formation conditions of contrails on June 2, 2023, over Clermont-Ferrand, France. To achieve

This project has received funding from the European Union's Horizon Europe
Research and innovation program under Grant Agreement No 101056885

this, we integrate a suite of co-located and complementary observations, including an all-sky camera, a LIDAR (Baray et al., 2020), an aircraft passage information from the ADS-B system (Peyrin et al., 2023), and meteorological, thermodynamic, and dynamic data from ECMWF-ERA5 reanalysis (Hersbach et al., 2020). This comprehensive approach allows us to analyse, in a preliminary sampling set, the atmospheric conditions governing contrail formation and persistence, as well as to examine aircraft passages both with and without contrail formation, over the course of a full day.
More specifically, the study has the following objectives:

1. Investigate the level of supersaturation necessary for contrail formation, taking into account the nonlinear relationships between temperature (T) and water vapor concentration (H_2O).
2. Establish the atmospheric conditions required for contrails to persist beyond a few minutes, providing insights into the factors that contribute to their longevity.
3. Exploit LIDAR and camera data to assess the vertical and horizontal extent of the contrails observed on this day, offering a detailed spatial analysis of their distribution and impact.

This paper is structured as follows: Section 2 describes the dataset used in the study. Section 3 outlines the methodology employed. Section 4 presents the observed contrail cases, highlighting key findings and patterns identified during the study. Section 5 focuses on the parameters influencing contrail formation and persistence. Finally, Section 6 summarizes the main conclusions and discussions of the future planes for further investigation in this topic.

4.2. Instruments and data

4.2.1 All-sky camera

An EKO SFR-02 all-sky camera has been in operation in Clermont-Ferrand since 2015. It is based on a compact Canon camera equipped with an added 180° fisheye lens. It captures images at a resolution of 1024 × 768 pixels every two minutes, with an adjustable acquisition frequency according to user requirements. The system includes a pump with a drying cartridge integrated to prevent condensation under the protective dome. The camera is connected to the network via an Ethernet interface, enabling automated image recording and real-time data transmission.
Since the camera is not equipped with an infrared sensor, it is configured to take images only between sunrise and sunset. In addition, the absence of a solar mask in the system may impact the quality of photos taken during intense sun radiation. The captured images are processed using the code ELIFAN (Lothon et al., 2019) to calculate cloud fraction.

4.2.2. LIDAR COPLid

A LIDAR system has been in operation in Clermont-Ferrand since 2008. Initially, it was a single-wavelength (355 nm) Raymetrics LIDAR equipped with a Quantel CFR-400 laser emitting at 355 nm. This system provided continuous vertical profiles of Rayleigh-Mie backscattering in the troposphere and lower stratosphere, along with a tropospheric water vapor Raman channel (Fréville et al., 2015).
In 2022, the LIDAR system was upgraded to include a three-wavelength configuration (355, 532 and 1064 nm), being then referred to as COPLid. This upgrade includes a more powerful Spectra Physics INDI laser emitting with a pulse repetition rate of 10 Hz. The signal reception is handled by a 40 cm diameter Cassegrain telescope with a 4 m focal length. The wavelength

This project has received funding from the European Union's Horizon Europe
Research and innovation program under Grant Agreement No 101056885

and polarization separation unit (WSU) was redesigned to incorporate the new channels, notably the addition of parallel and perpendicular polarization separation at 532 nm and a dedicated 1064 nm channel. In accordance with the ACTRIS Research Infrastructure's quality assurance standards, the WSU is positioned on a rotating stage to aid in the polarization calibration (Wandinger et al., 2020).

The system operation is now fully automated, incorporating rain and wind meteorological sensors, infrared barriers to detect human intrusions, and an ADS-B system to monitor air traffic which stops the operation if an aircraft passes overhead as described below in Section 2.4 (Peyrin et al., 2023). The operation is supervised by software developed at the OPGC observatory using LabVIEW, which autonomously manages all LIDAR measurement processes without the need for human intervention. The data provided by the LIDAR has a vertical resolution of 7.5 m and an integration time set to 1 minute (600 laser shots).

4.2.3. ACTRIS/EARLINET Single Calculus Chain (SCC) LIDAR data processing

The European Aerosol Research LIDAR Network (EARLINET) is a European research initiative dedicated to the LIDAR observation of atmospheric aerosols across the European continent (Pappalardo et al., 2014). To ensure a standardized processing of raw LIDAR data collected from various stations, EARLINET has developed the Single Calculus Chain (SCC), a community code designed for uniform data inversion procedures (Papagiannopoulos et al., 2020).

The SCC has two dedicated modules to produce optical parameters (Level 2) from raw data (Level 0):

1. ELPP (EARLINET LIDAR Pre-Processor): This module performs the pre-processing of raw LIDAR signals, applying essential corrections such as dead-time adjustment, trigger-delay correction, and background noise subtraction on the raw signals before calibration (D'Amico et al., 2016).
2. ELDA (EARLINET LIDAR Data Analyzer): This module generates vertical profiles of aerosol optical properties, including extinction and backscatter coefficients (Mattis et al., 2016).

The SCC incorporates an error analysis which provides the absolute statistical uncertainty of all variables using the standard error propagation (Taylor, 1997), and Monte Carlo simulations assuming Gaussian distributions for analog signals and Poisson distributions for photon-counting signals. Additionally, the SCC optimizes the vertical and temporal resolutions of LIDAR products while maintaining rigorous detection of low-level clouds.

In this study, we use the products generated by the SCC to determine the scattering ratio of persistent contrail signals. Specifically, the ELPP module provides the following variables:

1. Calculated molecular extinction at the emission wavelength (m^{-1}) which represents the attenuation of the laser beam due to molecular scattering and absorption along its path.
2. Calculated molecular LIDAR ratio at the emission wavelength (sr) which is the ratio between the molecular extinction and the molecular backscatter coefficients.

Additionally, the ELDA module calculates the following variables:

1. Aerosol backscatter coefficient ($m^{-1}\ sr^{-1}$) which quantifies the amount of laser light backscattered by aerosol particles in the atmosphere per unit distance and per unit solid angle.
2. Volume linear depolarization ratio (dimensionless units) which is the ratio of the cross-polarized to co-polarized backscattered signals. This parameter indicates changes in the polarization state of the laser beam after being scattered by atmospheric molecules and particles.

This project has received funding from the European Union's Horizon Europe Research and innovation program under Grant Agreement No 101056885

3. Particle linear depolarization ratio (dimensionless units) which is similar to the volume linear depolarization ratio but limited to the diffusion by aerosol and cloud particles, excluding the molecule contributions. It is a key indicator of particle non-sphericity and phase.

In this study, we assume an aerosol extinction-to-backscatter LIDAR ratio of 25 sr, a value commonly adopted for contrails and thin cirrus clouds (Iwabuchi et al., 2012). The scattering ratio is calculated as the ratio of the total (aerosol and molecular) backscatter coefficient to the molecular backscatter coefficient, where the molecular backscatter coefficient is defined as the ratio of the molecular extinction at the emission wavelength to the molecular LIDAR ratio at the same wavelength.

4.2.4. Automatic Dependent Surveillance–Broadcast (ADS-B) System

ADS-B is a surveillance technology used in aviation to track and share real time information such as the position, speed, and other flight parameters of aircrafts. Airplanes and helicopters are equipped with transponders that transmit data to ground-based receivers, such as the one integrated into the LIDAR COPLid acquisition system. This ADS-B system was installed on COPLid in 2019 to ensure compliance with aviation safety requirements by automatically halting laser emission when an aircraft is detected in proximity. The system is designed to ensure minimal disruption in data acquisition, facilitating the most continuous possible monitoring of the atmosphere, with particular attention to the effects of aviation on atmospheric composition. Full technical details of the installation are provided in Peyrin et al. (2023).

For this study, we use ADS-B records of aircraft with a specific configuration capable of detecting aircraft within a 100 km radius. The data included parameters such as latitude, longitude, altitude, distance from the LIDAR, distance between the aircraft and the camera, and aircraft type. This information is used to correlate observed contrails with the aircraft responsible for their formation. In addition to the aircraft type, the real time cruise altitude is a critical useful parameter to inform about the altitude of gas exhaust.

4.2.5. ECMWF-ERA5 reanalysis

Atmospheric reanalyses are a reliable source of meteorological parameters. ERA5 is the fifth-generation atmospheric reanalysis produced by the European Centre for Medium-Range Weather Forecasts (ECMWF). This global model provides detailed estimates of past and present atmospheric conditions at the global scale. ERA5 is generated using a numerical atmospheric model that assimilates a wide range of real-time meteorological observations, including satellite, airborne, and terrestrial data such as radiosondes and dropsondes (Hersbach et al., 2020).

This study is based on thermodynamic and dynamic parameters (temperature, air density, horizontal and vertical wind), and water vapor content (relative and specific humidity). The data are extracted at a horizontal resolution of 0.25° and a temporal resolution of one hour. To ensure maximum vertical resolution, we used the 137 native model levels rather than the interpolation on pressure levels. This requires recalculating relative humidity based on saturation vapor pressure and specific humidity, following the formula used in ECMWF-ERA5 reanalysis. Relative humidity is related to both ice and liquid water, depending on the temperature:

1. For $T < -23$ °C, the relative humidity is calculated with respect to ice (RHi).
2. For $T > 0$ °C, the relative humidity is calculated with respect to liquid water (RH).

This project has received funding from the European Union's Horizon Europe Research and innovation program under Grant Agreement No 101056885

3. For −23°C < T < 0 °C, a linear combination of the two is used.

4.3. Methodology

4.3.1. General approach

The systems used to investigate contrails provide a complementary information set. In the case of few water clouds, the full sky camera can identify white crystal ice contrails signatures around the lidar, due to wave matter interaction with the solar light. The ADS-B system provides information about aircraft types, their individual pathway and mainly their cruise altitude that cannot be deduced easily by the camera images. The real time lidar observations during the contrail formation is not expected to occur while the lidar field of view is rather small and the probability to have cruise pathway above the lidar is small and impossible for security reasons. However, the already formed contrails advected horizontally by the wind are often crossing the laser beam of the lidar allowing to observe vertical extends and horizontal spreading of the clouds using wind information. The thermodynamic information is provided by the meteorological analyses ECMWF-ERA5.
More specifically, the methodology employed to document contrails in this study consists of the following steps:

1. Identification of persistent and non-persistent contrails using images captured by the all-sky camera.
2. Determination of the aircraft responsible for the contrails and associated information about its position by analysing data from the ADS-B system.
3. Analysis of contrail signatures in COPLid LIDAR signals to infer their optical properties and their geometrical extension. Comparison with horizontal extents estimated with the camera.
4. Documentation of atmospheric conditions influencing the formation and persistence of contrails, including thermodynamic and dynamic parameters.

June 2, 2023 has been selected as a case study due to favourable observational conditions. The instruments (LIDAR and camera) were fully operational, and the sky was free of low clouds that could have disrupted the observations. On this day, a total of 12 contrails were observed as illustrated in Figure 1. In the rest of this paper, these 12 contrails are identified as C1 to C12.

This project has received funding from the European Union's Horizon Europe
Research and innovation program under Grant Agreement No 101056885

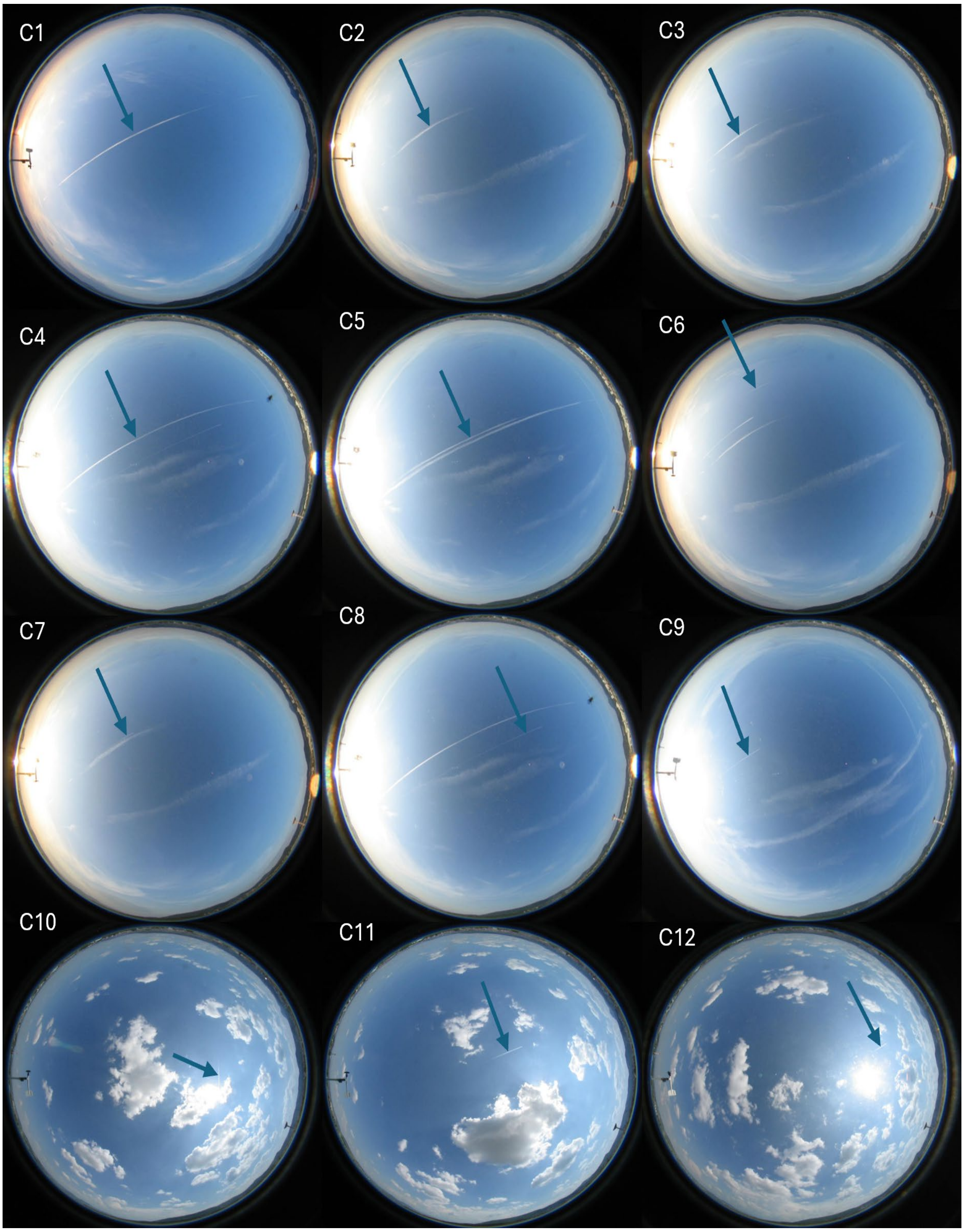

Figure 22. Observations of different contrails photographed at the moment of their formation by the all-sky camera above Clermont-Ferrand on June 2, 2023. The annotations C1 to C12 refer to the different contrails described in section 4. The times of passage of the aircraft that formed these contrails are: C1 4:20, C2 4:50, C3 5:04, C4 5:30, C5 5:34, C6 4:54 , C7 4:59 , C8 5:34 , C9 6:04, C10 13:35, C11 13:43, C12 14:32 UT.

4.3.2. Contrail horizontal extent estimation

In this study, the contrail width has been estimated using two distinct and independent approaches: (1) full-sky camera imagery and (2) lidar measurements combined with horizontal wind from the ECMWF ERA5 reanalysis.

The image-based method is based on optical calculations under Gaussian conditions. This means that the magnification does not change as a function of the field angle. Consequently,

This project has received funding from the European Union's Horizon Europe Research and innovation program under Grant Agreement No 101056885

the effects of distortion do not require correction. The method involves several processing steps and its application to contrails C1 to C5 is shown in Figure 2:

1. Camera calibration: The effective focal length of the double-lens full-sky camera is determined using a calibration target composed of squares, positioned at a distance of 2.77 meters. The effective focal length is thus estimated to be 1.20 ± 0.05 mm.
2. Selection of measurement region: The estimated field of view with negligible distortion is ± 27°. It is only in this area that contrail width calculations will be made. The contrail width is measured near the centre of the image to coincide with the lidar field of view used in the second method.
3. Contrail direction determination: The main axis of the contrail and the orthogonal cross-sectional axis (white lines on Figure 2), which allow to determine the contrail width are manually identified.
4. Width estimation: The contrail width, in terms of pixel count, is finally visually estimated on image in the red channel by analysing the pixel value on the orthogonal cross-sectional axis. We distinguish the length where the contrail is identified with certainty (black segments on Figure 2), from the length where the signature is less clear (grey segments on Figure 2) due to contrail dissipation and/or lack of image sharpness or resolution. The contrail width is estimated by the mean of these two lengths in pixel number. The conversion from a pixel number n to a physical distance w (in m) accounts for the altitude of the aircraft z (in km), the equivalent focal length f (mm) and the size of an image pixel x (**µ**m) according to Equation (1).

$$w = \frac{z \times x \times n}{f}, \quad (1)$$

5. Incertitude analysis: The error estimation on the contrail width Δw was conducted through error propagation according Equation (2).

$$\Delta w = w\sqrt{\left(\frac{\Delta z}{z}\right)^2 + \left(\frac{\Delta n}{n}\right)^2 + \left(\frac{\Delta f}{f}\right)^2}, \quad (2)$$

where the uncertainty on the altitude Δz is taken as the absolute difference between the aircraft altitude provided by the ADS-B system and the bottom altitude of the contrail observed by the lidar. The uncertainty on the number of pixels Δn is estimated from half the difference between the grey and black segments pixel numbers and the uncertainty on the focal length Δf has been estimated experimentally to 0.05 mm. No uncertainty is taken for the size of a pixel image deduced from the manufacturer data however to derive it we have considered that all the pixels of the CCD camera are used to record the image.

This project has received funding from the European Union's Horizon Europe Research and innovation program under Grant Agreement No 101056885

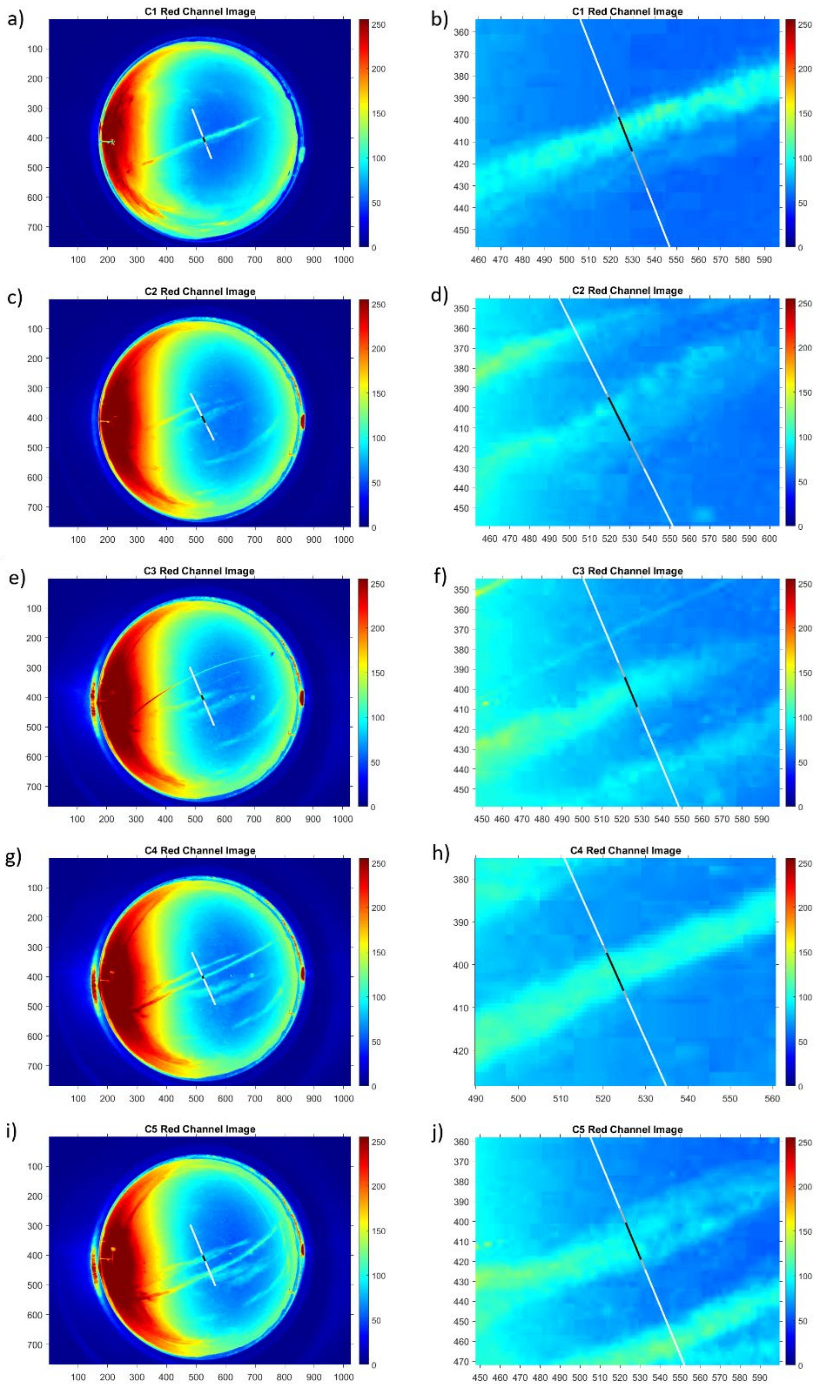

Figure 23. Red channel pixel values (ranging from 0 to 255) in full-sky camera images, showing a transect crossing contrails C1 to C5, captured when each contrail is near the image centre and close to the lidar vertical. Panels (a) to (i) show the full images, while panels (b) to (j) present a zoomed view of the transects. The white line marks the full transect, with black and gray segments indicating, respectively, the sections where the contrail is clearly identified and where its presence is less distinct. The times of passage of the contrails at the LIDAR vertical are : C1 4:34, C2 5:16, C3 5:28, C4 5:42, C5 5:48.

The Lidar based method (2) estimates the contrail width by multiplying the horizontal wind speed (V in meter per second) by the time t during which the contrail remains within the lidar field of view and by a geometrical correction factor. This factor is due to the fact that the lidar doesn’t record the contrail according to the width direction because of the wind. The duration during which a contrail remains within the lidar field of view is estimated based on the lidar signal profiles that present a detectable contrail signature. Given that the temporal resolution

This project has received funding from the European Union’s Horizon Europe Research and innovation program under Grant Agreement No 101056885

of the lidar system is one minute, and that a contrail intersecting the lidar beam only partially during the integration period may still produce a detectable signature on the lidar signal, the total integration time t is estimated by subtracting one minute from the observed lidar detection interval provided in Table 1. This one-minute subtraction accounts for the possibility of partial detection and is subsequently considered as the uncertainty Δt associated with the integration time.

Finally, the contrail width L can be written as:

$$L = V \times t \times cos(\delta - \theta)\ , \tag{3}$$

with

$$\theta = tan^{-1} \frac{|v|}{|u|}$$

And

$$V = \sqrt{u^2 + v^2}$$

where:

θ is the angle between the West and the wind direction,

u is the zonal wind component (m s-1, positive from west to east),

v is the meridional wind component (m s-1, positive from south to north),

δ is the angle between the contrail width direction (given by the black segment on Figure 2) and the East direction.

The uncertainty on the width is estimated by applying error propagation to equation (3) and give equation (4) :

$$\Delta L = \sqrt{(V \times cos(\delta - \theta) \times \Delta t)^2 + (V \times t \times sin(\delta - \theta) \times \Delta\delta)^2 + \left(t \times \left(\frac{|u|}{V} \times cos(\delta - \theta) - \frac{|v| \times sin(\delta-\theta)}{V}\right) \times \Delta u\right)^2 + \left(t \times \left(\frac{|v|}{V} \times cos(\delta - \theta) + \frac{|u| \times sin(\delta-\theta)}{V}\right) \times \Delta v\right)^2} \tag{4}$$

with

6. Δu and Δv the uncertainties on the wind components u, v obtained from the ECMWF ERA5 ensemble spread which is the standard deviation of a set of forecasts generated using a probabilistic ensemble approach, which includes multiple perturbed members along with an unperturbed forecast known as the control member.

7. Δt the uncertainty on the lidar integration time t.

8. $\Delta\delta$ the uncertainty on the angle $\boldsymbol{\delta}$ representative of contrail width direction. This uncertainty is estimated to be 1°.

4.4. Contrail observations, aircraft identification and LIDAR signatures

The all-sky camera began recording usable images on June 2, 2023, at approximately 03:30 UTC. The first images of the day show a clear sky, free of low cumulus clouds or high cirrus clouds. Around 04:08 UTC, a few thin cirrus clouds appear at the edge of the camera image. These clouds are visible in Figure 1 (C1 to C9), which displays the contrails observed by the camera on June 2, 2023. The sky remains mostly clear in the morning between 04:00 and 06:30 UTC, allowing for a good observation of the contrails. In the afternoon, between 13:00 and 17:00 UTC, a few low cumulus clouds develop, slightly hindering the contrail observations (C10 to C12).

This project has received funding from the European Union's Horizon Europe Research and innovation program under Grant Agreement No 101056885

Among the contrails formed in the morning, C1 to C5 are persistent, whereas C6 to C9 are not. Similarly, the contrails observed in the afternoon (C10 to C12) are non-persistent. To link the observed contrails to the aircraft that generated them, we used the ADS-B module in conjunction with the camera. Figure 3 illustrates the flight paths of the aircraft responsible for the contrails shown in Figure 1, and Table 1 provides technical details, including aircraft types, positions, and passage times.

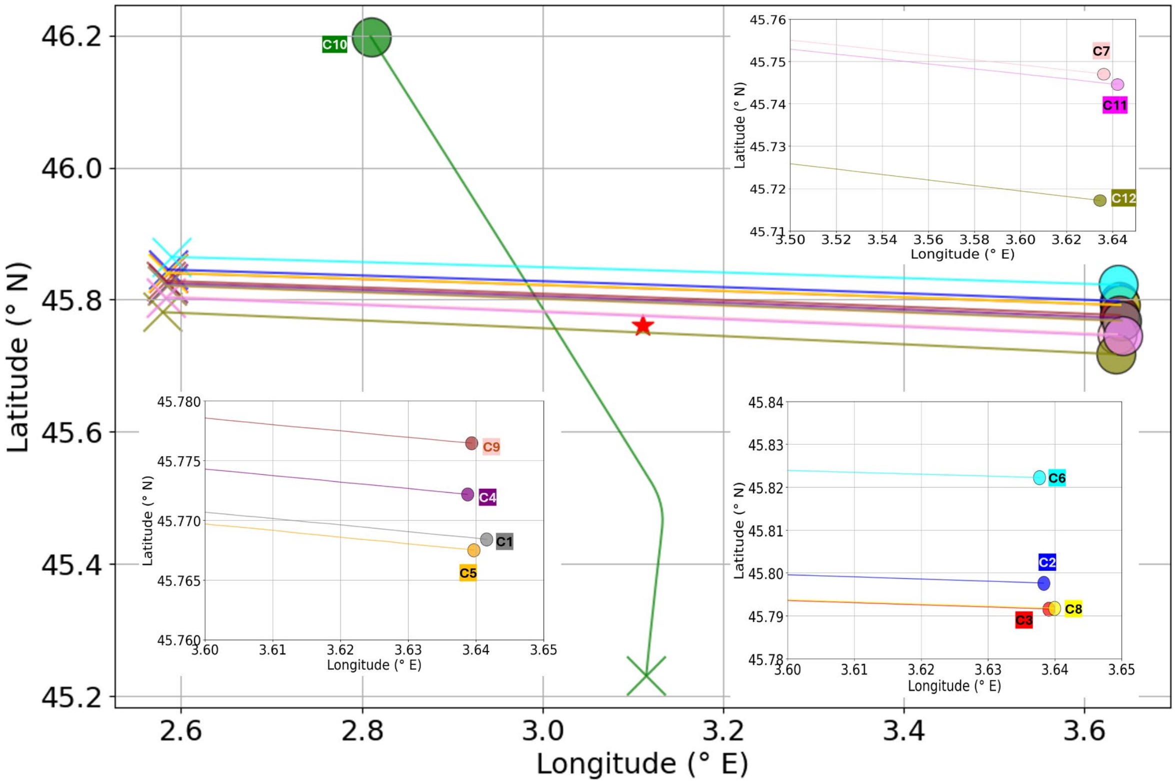

Figure 24. Trajectories of the 12 aircrafts that formed contrails above Clermont-Ferrand on June 2, 2023, from ADS-B data. The direction of each flight is from the circle to the cross. The colours are the following : C1 grey , C2 blue, C3 red, C4 purple, C5 light orange, C6 cyan, C7 pink, C8 yellow, C9 orange, C10 green, C11 dark pink and C12 dark green. The red star indicates the position of the LIDAR.

The aircrafts responsible for contrails C1 to C12 are flying over the full-sky camera at altitudes between 9.75 km and 11.58 km, the exact altitudes of each flight being given in Table 1. Table 1 indicates also that persistent contrails are associated with aircraft of the same type and equipped with the same engines (Boeing 777, twin-engine). Conversely, non-persistent contrails are linked to different aircraft types with various engine configurations. However, it should be noted that these conclusions reflect only the observations made on the studied day and should not be considered as a general rule. As depicted in Figure 3, all aircraft followed a similar east-to-west trajectory, except for the one responsible for contrail C10, which travelled north to south.

Table 2. Summary of main aircraft characteristics and all sky camera observations of contrails on June 2, 2023.

This project has received funding from the European Union's Horizon Europe Research and innovation program under Grant Agreement No 101056885

Contrail	Observation duration camera (min)	Aircraft type	Aircraft motor	Aircraft altitude (km)	Time of aircraft passage in the camera field of view (UTC - H:MM)	Time of LIDAR signature (UTC - H:MM:SS)
C1	160	Boeing 777-224	2 engine	10.36	4:16-4:20	4:33:15 4:44:21
C2	124	Boeing 777-2DZLR	2 engine	10.36	4:46-4:50	5:15:40 5:24:45
C3	132	Boeing 777-36NER	2 engine	10.36	5:00-5:04	5:27:31 5:35:00
C4	166	Boeing 777-31HER-35597	2 engine	9.75	5:26-5:30	5:41:04 5:45:06
C5	106	Boeing 777-31HER-35575	2 engine	10.36	5:30-5:34	5:47:08 5:56:13
C6	<1	Airbus A380-842-236	4 engine	11.58	4:50-4:54	None
C7	<1	Airbus A350-1041	2 engine	11.58	4:55-4:59	None
C8	<3	Airbus A380-842	4 engine	10.97	5:30-5:34	None
C9	<3	Boeing 787-9 DRL-39657	2 engine	10.97	6:00-6:04	None
C10	<3	Airbus A320-214	2 engine	10.66	13:31-13:35	None
C11	<1	Airbus A330-343	2 engine	11.58	13:39-13:43	None
C12	<3	Boeing 777-333(ER)	2 engine	10.36	14:28-14:32	None

Figure 4 presents the backscatter profile measurements recorded by the LIDAR COPLid during contrail observations during the morning of June 2, 2023. The signatures of five persistent contrails (C1 to C5) can be identified between 04:30 UTC and 05:45 UTC.
Additionally, Figure 4 shows strong backscatter signals after 06:00 UTC, corresponding to cirrus clouds given their altitude and thickness. The signature of C1 appears on the LIDAR profiles at 04:34 UTC, 20 minutes after the contrail formation. This contrail remains visible on the camera image for 2 hours and 40 minutes before exiting from the image frame.

This project has received funding from the European Union's Horizon Europe Research and innovation program under Grant Agreement No 101056885

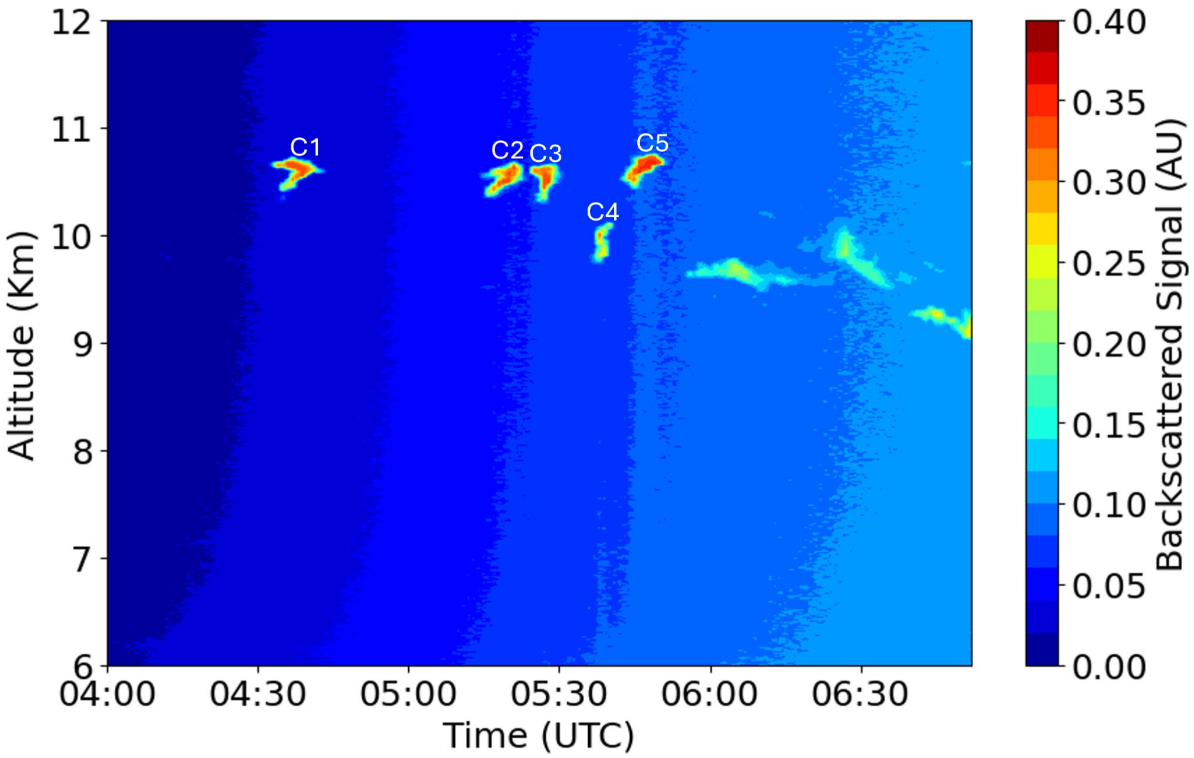

Figure 25. 355 nm photocounting perpendicular polarization backscatter coefficient profiles measured by the LIDAR COPLid on June 2, 2023 between 4:00 and 6:50 UTC with signatures of contrails C1 to C5.

The signature of C2 appears on the LIDAR profiles at 05:16 UTC, 32 minutes after its formation. It remains on the camera image for 2 hours and 4 minutes before exiting, while still developing. However, only a small part persisted, with most of it dissipating a few seconds after the aircraft's passage. Meanwhile, C1 and C2 are still visible on the camera image. C3 remains visible for over 2 hours and 12 minutes.

While only a small part of C3 persists a few minutes after its formation, C4 remains visible on the camera image. The other contrails also continue to evolve within the image frame. After 14 minutes of development, the signature of C4 appears on the LIDAR data at 05:42 UTC. C4 has the longest visibility duration among the contrails, remaining in the field of view for 1 hour and 38 minutes before exiting at 07:20 UTC.

C5 appears on the camera image at around 05:30 UTC, with the corresponding aircraft flying at an average altitude of 10.36 km. Its signature becomes visible on LIDAR profiles 20 minutes after formation, around 05:48 UTC. It then drifts to the edge of the camera image and merges with other contrails at 07:16 UTC.

The other contrails observed on Figure 1 on June 2, 2023 (C6 to C12) are non-persistent and no signature is identifiable on the LIDAR data.

C6 has been generated by a four-engine Airbus A380-842 at 04:50 UTC at an altitude of 11.58 km, but the associated contrail dissipates almost immediately. A few minutes later, at 04:58 UTC, a twin-engine Airbus A350-1041 flying at the same altitude did not generate any persistent contrail (C7). Around 05:30 UTC, a four-engine Airbus A380-842 generates C8, which is more visible than C6 and C7 and persists a little longer before dissipating. This aircraft is flying at an altitude of 10.97 km. About thirty minutes later, at 06:00 UTC, a twin-engine Boeing 787-9 generates a non-persistent contrail (C9), at the same altitude, 10.97 km. In the afternoon, between 13:00 and 17:00 UTC, several aircraft are observed, but among the contrails observed (C10 at 13:31 UTC, twin-engine Airbus A320-214, altitude 10.66 km; C11 at

This project has received funding from the European Union's Horizon Europe
Research and innovation program under Grant Agreement No 101056885

13:39, twin-engine Airbus A330-343 altitude 11.58 km; C12, twin-engine Boeing 777-333(ER) at 14:26 UTC and 14:28 UTC, altitude 10.36 km), none are persistent. These results are generally consistent with Meijer et al. (2024), who estimated contrail altitudes using CALIOP and GOES-16 data and a convolutional neural network approach. They demonstrated that contrails are typically observed between 8 and 15 km in altitude, with a peak occurring between 12 and 14 km. Contrails form at slightly higher altitudes in summer and lower in winter, with an average altitude of approximately 11.1 km in winter and 11.8 km in summer. On June 2, 2023, two factors distinguish aircraft forming persistent contrails from those that did not : altitude and time. The aircraft producing persistent contrails flew at lower altitudes (below 10.36 km) and were observed in the morning. We therefore propose to investigate the differences in meteorological conditions between the two.

4.5. Analysis of atmospheric conditions and estimation of contrail extensions

4.5.1. Characterization of water vapor supersaturation zones

In this section, we analyse the relationship between humidity, temperature, and wind patterns with contrail observation and persistence. The values of these parameters, obtained from the ECMWF-ERA5 reanalysis at the 250 hPa pressure level close to typical aircraft cruising altitudes and contrail formation heights, are presented in Figure 5.

The maps at 05:00 and 14:00 UTC are representative of the atmospheric conditions encountered by aircraft in the morning and afternoon, respectively. In the morning, relative humidity fields reveal a moist layer with relative humidity values exceeding 118%, covering the entire central region of France (Figure 5a). In the afternoon, this moist layer is not strongly advected and becomes drier, with values decreasing below 100 % (Figure 5b). The temperature between 217 and 221 K above France at this pressure level follows an inverse trend, slightly increasing by 0.12 K between 05:00 and 14:00 UTC (Figure 5c, d).

Figure 5 (e,f) shows that the intensity of horizontal winds is relatively strong (29 m s^{-1}) over northern and southern France but remains weak in the contrail observation area (6 m s^{-1}). This is consistent with the limited advection of the high-humidity region observed in the morning (Fig. 4a). Additionally, at a large scale, the vertical wind remains slightly upward in the morning and downward in the afternoon. Although the magnitudes are very low (less than 0.1 Pa s^{-1}, Fig. 4f), this is in agreement with observations presented by Gierens and Brinkop (2012), showing that upward wind and divergent airflow are favourable conditions for the formation of ice supersaturation, and ice supersaturation is rare in regions with downward or convergent flow.

This project has received funding from the European Union's Horizon Europe
Research and innovation program under Grant Agreement No 101056885

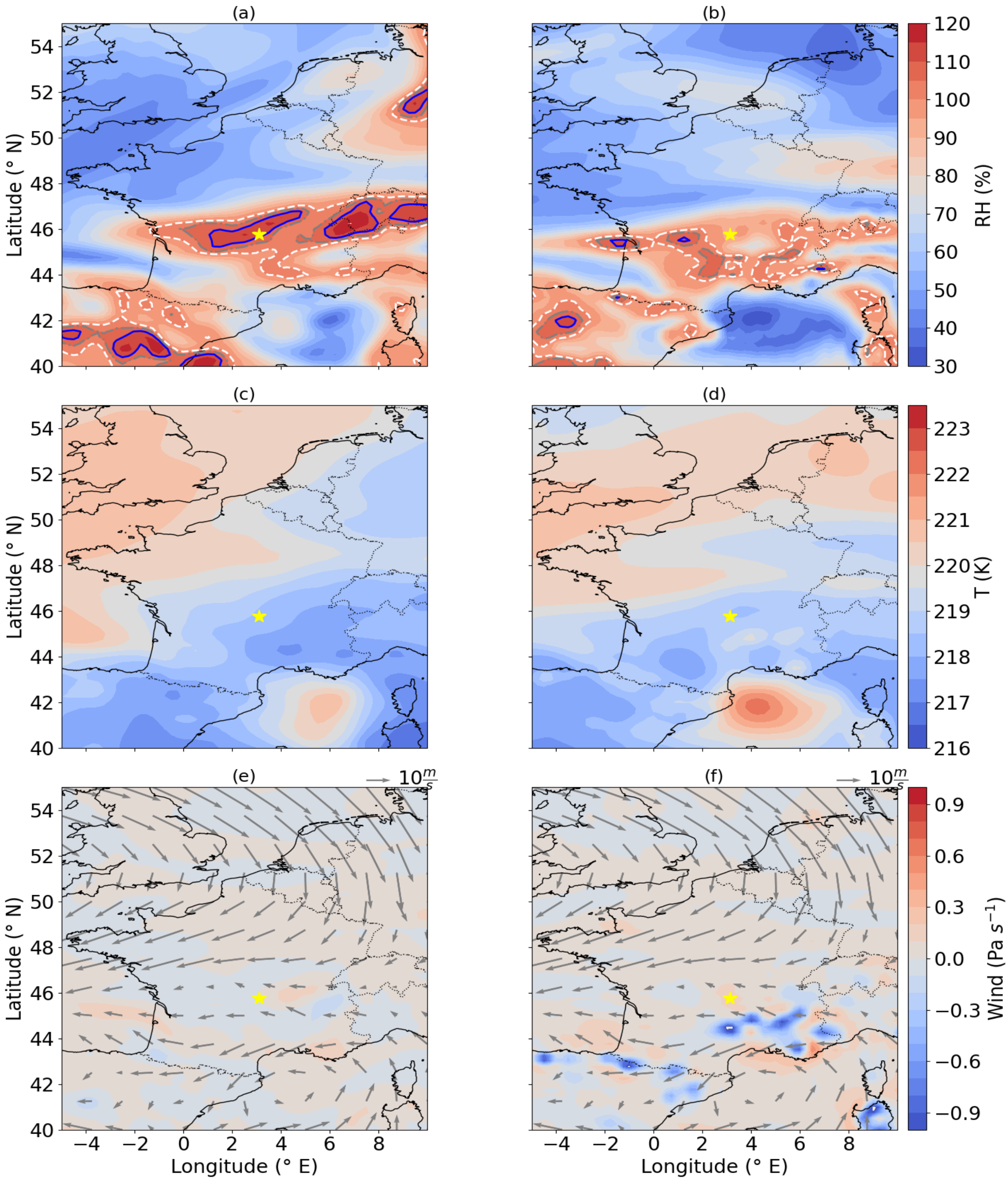

Figure 26. Horizontal maps of relative humidity (a,b), temperature (c,d) and the 3 components of the wind (e,f) on the 250 hPa pressure level on June 2, 2023, at 05:00 UTC (a,c,e) and 14:00 UTC (b,d,f). The relative humidity isocontours 100, 105 and 110 % are marked by white dotted lines, grey and blue solid lines respectively (a,b). The horizontal wind direction is indicated by arrows whose size indicates the horizontal wind intensity (e,f). The position of the observation point is indicated by a yellow star.

ECMWF-ERA5 have thus enabled the characterization of the evolution of relative humidity, temperature, and wind distributions between morning and afternoon of June 2, 2023, on a large horizontal scale near the aircraft cruising altitudes. We now focus on the temporal and vertical evolution of supersaturation zones directly above the contrail observation area. To this end, Figure 6 presents the temporal evolution of the vertical relative humidity profile during June 2, 2023.

This project has received funding from the European Union's Horizon Europe Research and innovation program under Grant Agreement No 101056885

Between 00:00 and 01:00 UTC, the entire troposphere remains undersaturated (RH < 100 %). Between 02:00 and 13:00 UTC, the region between 8.9 and 11.1 km becomes supersaturated up to 118%, before becoming undersaturated again until 17:00 UTC. After 17:00 UTC, supersaturation re-establishes, but with relative humidity values below 105 %.
Persistent contrails (C1 to C5) formed within the supersaturated zone (RH > 105 %), whereas non-persistent contrails (C6 to C12) developed in an undersaturated environment (RH < 100 %).

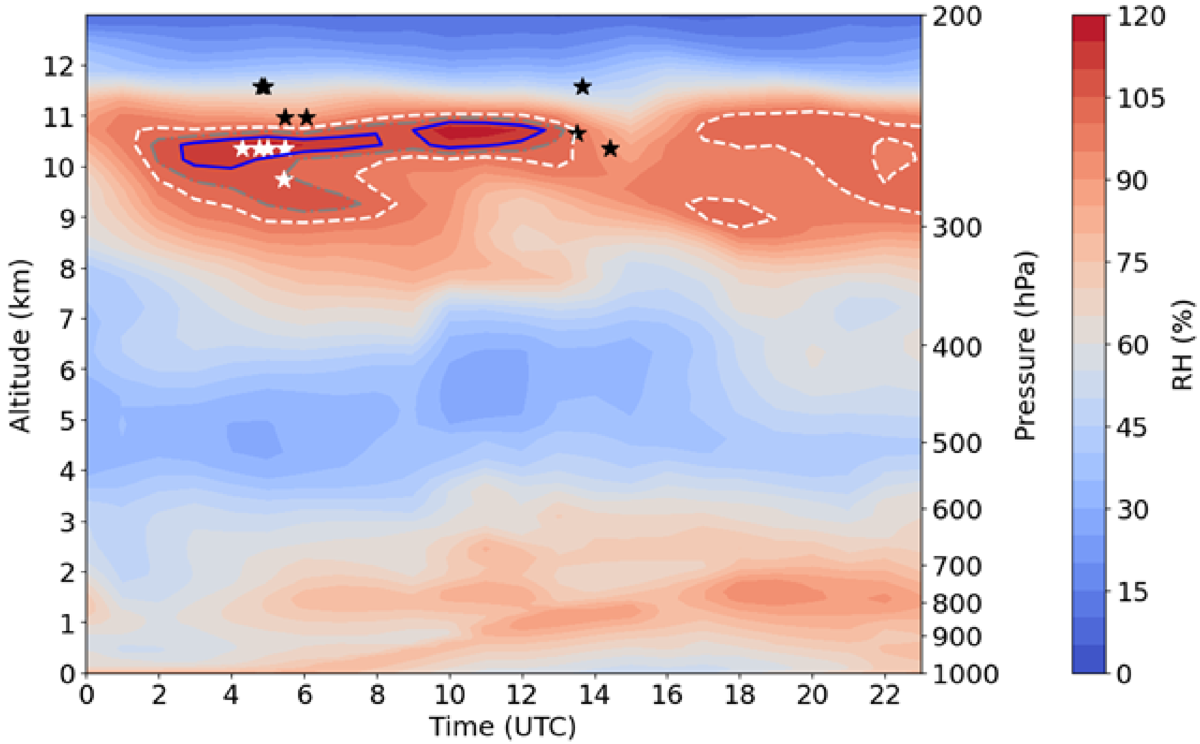

Figure 27. Temporal evolution of the vertical profile of relative humidity as a function of altitude and pressure level above the observation point (45.76°N, 3.11°E) on June 2, 2023, between 00:00 and 23:00 UTC. The relative humidity isocontours 100, 105 and 110% are marked by white dotted lines, gray and blue solid lines respectively. White stars are for C1 to C5 persistent contrails while black stars are for non-persistent contrails C6 to C12. The times and altitudes of aircraft that formed persistent contrails are indicated by white stars, the black stars representing those that did not.

The results on the conditions of formation and persistence of contrails observed in the present study show some similarities but also some differences related to the works previously published (Freudenthaler et al., 1995; Poellot et al., 1999; Voigt et al., 2010). The altitudes of the contrails observed here are consistent with those reported by Voigt et al. (2010), who observed contrails forming between 8.5 and 11.6 km at temperatures ranging from 213 to 229 K during the first CONCERT campaign in Europe. In the present study, contrails are observed between 9.7 and 11.6 km, with temperatures ranging from 217 to 223 K. This confirms that in our study, the atmospheric conditions leading to contrail formation are comparable to the typical mid-latitude atmospheric conditions where commercial aircraft commonly operate.
However, some minor differences can be noted. The contrails observed in the present study persisting for less than three minutes form at slightly lower temperatures, around 210 K. Some variability could be linked to local atmospheric conditions and aircraft engine characteristics. Voigt et al. (2010) reported values of RHi predominantly between 75 % and 105 %, with extremes ranging from 55 % to 122 %. Our observations present a similar distribution, with most contrails occurring within an RHi range between 85 % and 115 %. We recorded RHi

This project has received funding from the European Union's Horizon Europe Research and innovation program under Grant Agreement No 101056885

maximum values reaching 120 %, that is slightly lower than those observed by Voigt et al. (2010).

4.5.2. Small-scale variability of atmospheric parameters along the contrail

The analysis of temperature, humidity, and wind fields presented in Section 5.1 reveal distinct atmospheric characteristics in terms of temperature and humidity between flights that produced persistent contrails and those that did not. This section aims to examine in greater detail how thermodynamic parameters evolve during flight, with a specific focus on C1. Figure 7 shows the temporal evolution of these parameters, obtained by interpolating atmospheric data in space and time along the aircraft's trajectory.

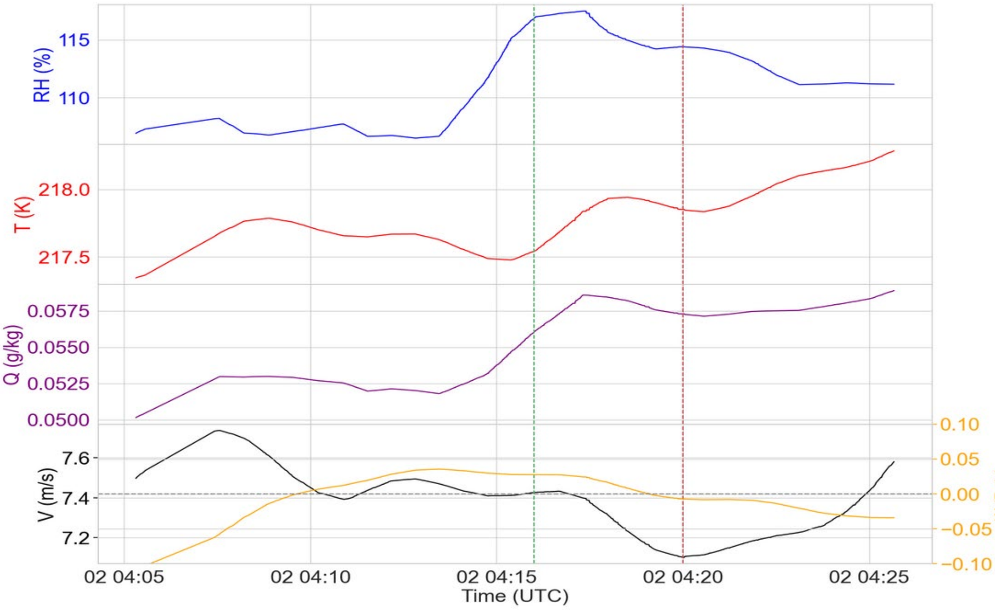

Figure 28. ECMWF-ERA5 atmospheric parameters interpolated along the trajectory of the aircraft which has generated C1. The green vertical line marks the moment when the aircraft first appears on camera (04:16 UTC), while the red vertical line indicates when it exits the camera image (04:20 UTC). This time interval is considered as the contrail formation phase.

The position of the aircraft, a twin-engine Boeing 777-224, was obtained using the ADS-B system. During the period of contrail formation, from 04:16 UTC to 04:20 UTC, the relative humidity peaks at 118 % before rapidly decreasing to 106 %. This decline is associated with downward wind, a decrease in specific humidity, and a slight reduction in horizontal wind speed. Similar variability in thermodynamic parameters is observed for other contrail cases.

4.5.3. Estimation of the spatial extension and optical properties of contrails

This section presents an estimation of the spatial extent of contrails. To assess their vertical extent, we use the scattering ratio of LIDAR signals to identify the contrail base and top. Figure 8 presents the vertical profiles of the aerosol backscatter coefficient, scattering ratio, and volume and particle depolarization ratios between 4:34 and 4:44 UTC for C1, 5:16 to 5:24 UTC for C2, 5:28 to 5:35 UTC for C3, 5:42 to 5:45 UTC for C4 and 5:48 to 5:56 UTC for C5.

This project has received funding from the European Union's Horizon Europe Research and innovation program under Grant Agreement No 101056885

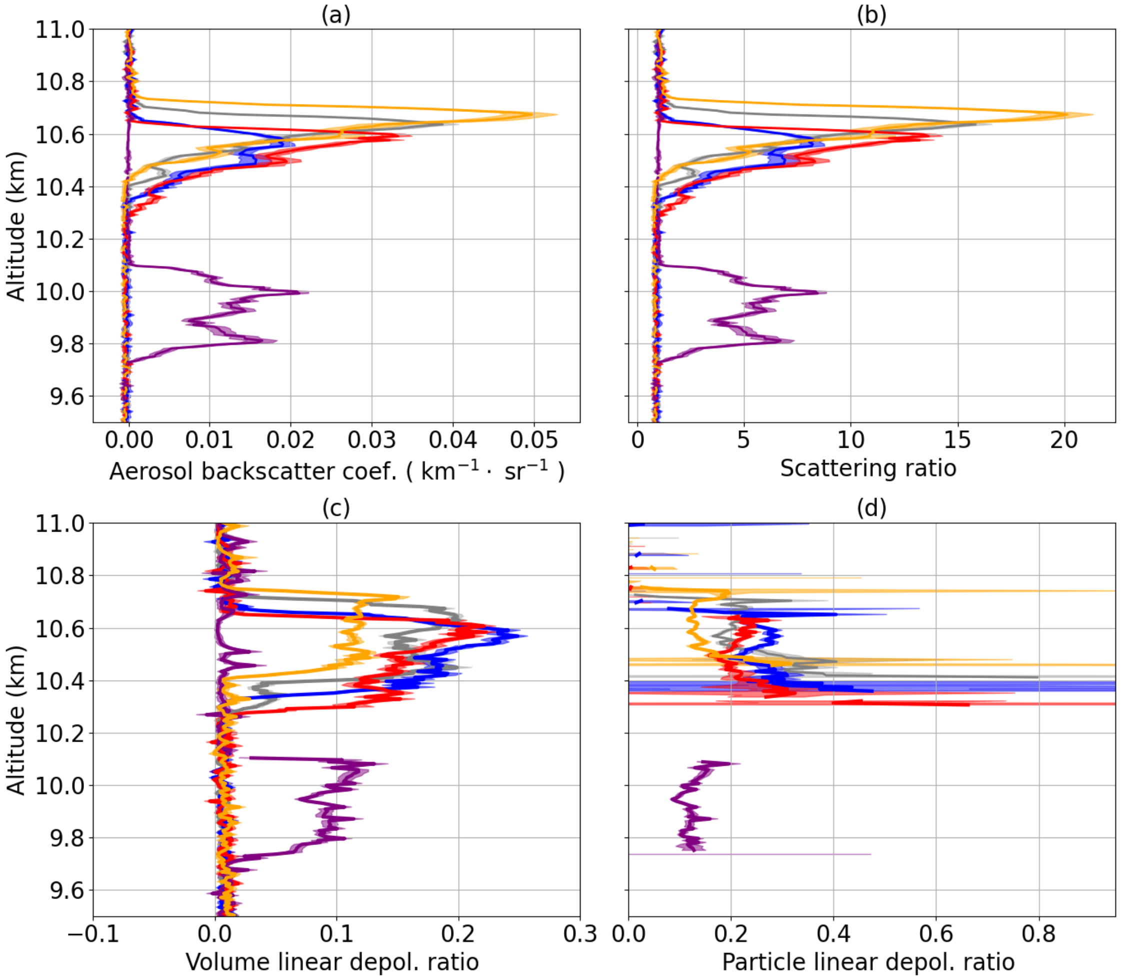

Figure 29. LIDAR parameter profiles during observations of contrails C1 to C5. (a) Aerosol backscatter coefficient, (b) Scattering ratio, (c) volume linear depolarization ratio and (d) particle linear depolarization. The color code is the same as Figure 3 (C1 grey , C2 blue, C3 red, C4 purple, C5 light orange). Statistical errors given by the SCC ELDA module are indicated by shaded areas.

Contrail signatures on lidar profiles are in the altitude range between 9.7 and 10.1 km for C4 and between 10.3 and 10.8 km for the other four contrails. For C1, a main peak appears in the aerosol backscatter coefficient, which reaches the value of 0.004 km^{-1} sr^{-1} at the altitude 10.64 km. This peak is also visible in the scattering ratio, with the highest peak reaching SR = 15.85 (Fig. 7b). The maximum values of aerosol backscatter coefficient and scattering ratio are obtained for contrail C5 and are 0.49 km^{-1} sr^{-1} and 20.13 respectively at the altitude 10.67 km. The signatures associated with the contrail C4 are at a lower altitude, between 9.7 and 10.1 km. The maximum values for volume linear depolarization ratio and particle linear depolarization are between 0.13 and 0.24 and between 0.2 and 0.3 respectively. All values are summarized in Table 2.

Table 3: Maximum values of lidar parameters (Profiles given in Figure 8) associated with contrails C1 to C5 on June 2, 2023.

This project has received funding from the European Union's Horizon Europe Research and innovation program under Grant Agreement No 101056885

Contrail	Backscattered signal (km^{-1} sr^{-1})	Scattering ratio	volume depolarization	particle depolarization
C1	0.038 ± 0,002	15.8 ± 0,8	0,2 0 ± 0,01	0,41± 0.08
C2	0.019 ± 0,001	8.3 ± 0,4	0,24 ± 0,01	0,40± 0.09
C3	0.033 ± 0,002	13.6 ± 0,7	0,23 ± 0,01	0,45± 0.28
C4	0.021 ± 0,001	8.4 ± 0,4	0,13 ± 0,01	0,17± 0,02
C5	0.049 ± 003	20.1 ± 1,2	0,15 ± 0,01	0,32± 0.12

The contrail vertical extent is estimated by the difference between the top and the base altitudes of the contrail. The top altitude is estimated as the first altitude above the peak where the signal decreases below the mean of the 11-12 km scattering ratios (above the contrail). The uncertainty on this altitude is obtained as the first altitude above the peak where the signal decreases below the mean plus two standard deviations of the 11-12 km scattering ratios. The base altitude is obtained in the same manner, with the mean and standard deviation of scattering ratios calculated between 9 and 10 km (below the contrail). For the contrails C1 to C5, the vertical extents vary between 340 ±10 and 440 ±60 m as indicated in Table 3 which presents the spatial extent calculated for all contrails observed on June 2, 2023. The contrails are observed by the lidar between 14 minutes and 32 minutes after their formation. It is observed that older is the contrail, lower is its vertical extent. However, with only 5 cases observed the same morning, it is not enough to draw a conclusion.

The estimation of contrail width is reasonably consistent between the two methods, according to the uncertainties. Using the camera-based approach, the values range from 0.53 km to 1.60 km, while in the lidar-based method the values range from 0.35 km to 1.90 km. Contrail C1 presents the largest width according to lidar observations (1.90 km), whereas contrail C2 is the widest considering the camera estimation (1.60 km). C4 is the least wide contrail for both estimations, although there is a notable discrepancy between the two methods (0.35 km with lidar versus 0.53 km with the camera).

One might expect that a longer time interval between the aircraft's passage and the observation would result in increasing the contrail width. This the case of C2, which has both the largest width estimated with the camera and the longest time elapsed between aircraft passage and observation. Conversely, C4, the narrowest contrail, corresponds to the shortest time interval. However, for the remaining contrails, no clear relationship is observed between the elapsed time and contrail width.

Poellot et al. (1999) have estimated horizontal extents ranging from 100 to 300 m for contrails less than 15 minutes old, while Freudenthaler et al. (1995) reported values between 1 km and 3 km for older contrails, up to 30 minutes old. In this study, the estimated contrail widths are in the same order of magnitude, lower than 2 km for contrails younger than 32 minutes, which is consistent with results of these two publications.

Table 4: Spatial extent estimation of persistent contrails observed on June 2, 2023. The time between the aircraft passage in the camera field and the LIDAR signature was estimated by taking the midpoint of the observation time intervals given in Table 2.

This project has received funding from the European Union's Horizon Europe Research and innovation program under Grant Agreement No 101056885

Contrail	Time between the aircraft passage and the observation of the contrail at zenith (min)	Contrail width calculated from camera (km)	Contrail width calculated from Lidar (km)	vertical extent (m) observed by Lidar
C1	20 ± 2	1.40 ± 0.60	1.90 ± 0.32	390 ± 60
C2	32 ± 2	1.60 ± 0.44	1.56 ± 0.29	340 ± 10
C3	28 ± 2	1.10 ± 0.33	0.94 ± 0.22	370 ± 20
C4	14 ± 2	0.53 ± 0.10	0.35 ± 0.14	440 ± 20
C5	20 ± 2	1.30 ± 0.33	1.08 ± 0.25	400 ± 60

4.5.4. Determination of threshold values for the formation and persistence of contrails

According to Heymsfield et al. (2010), contrails can form when aircraft exhaust gases interact with ambient air exceeding the supersaturation threshold relative to liquid water. However, the environment needs to be supersaturated with regard to ice in order for contrails to persist (Iwabuchi et al., 2012).

To precisely characterize the formation and persistence thresholds of contrails on June 2, 2023, Figure 9 presents the probability density functions of relative humidity and air temperature during the contrail formation period observed. These parameters were obtained through interpolation in latitude, longitude, altitude, and time at aircraft positions using ECMWF-ERA5.

Figure 9 reveals three distinct groups of contrails:

1. Short-lived contrails (lifetime < 1 min) form in an environment with RHi between 45 % and 65 % (Fig. 9a) and temperatures between 210 K and 214.5 K (Fig. 9b) (C6 to C7).
2. Moderately persistent contrails (lifetime < 3 min) are associated with RHi values between 85 % and 100 % (Fig. 9a) and temperatures between 215 K and 216.5 K (Fig. 9b) (C8 to C10)
3. Persistent contrails (C1 to C5), visible for more than two hours before exiting the camera field, form with RHi between 105 % and 120 % (Fig. 9a) and temperatures between 217 K and 218 K, occasionally reaching 223 K (Fig. 9b).

This project has received funding from the European Union's Horizon Europe Research and innovation program under Grant Agreement No 101056885

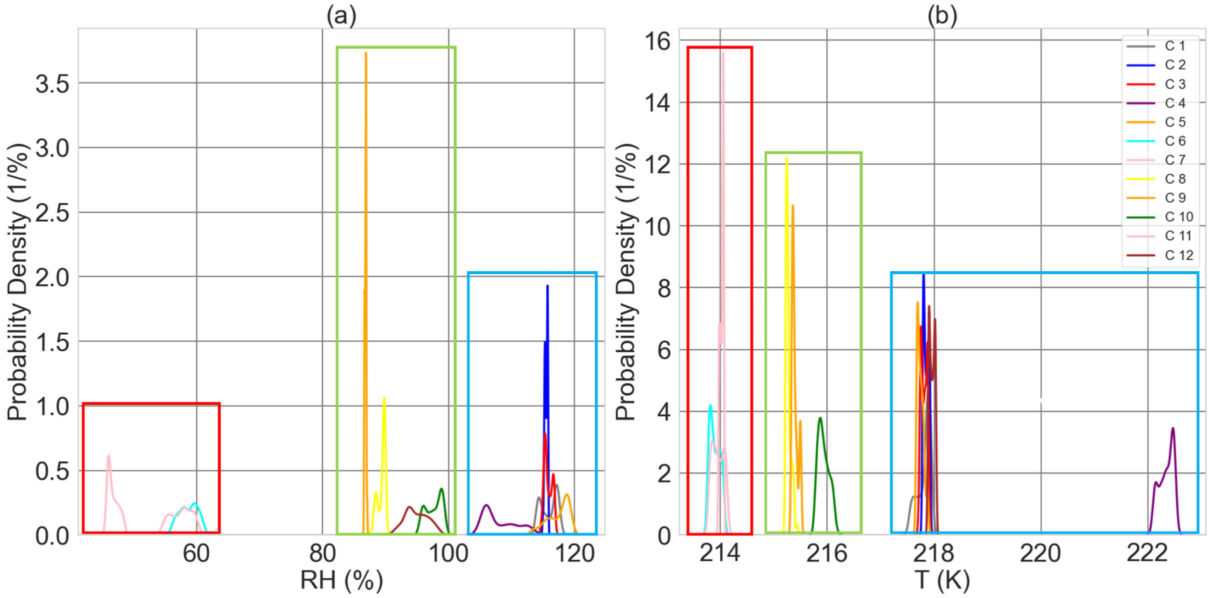

Figure 30. Relative frequency of relative humidity (a) and temperature (b) values along the aircraft path during (4 minutes on average) the observation period. The blue frame indicates contrails persisting for more than 2 hours before leaving the camera's field of view, the green frame indicates contrails persisting for less than 3 minutes before disappearing, and the red frame indicates contrails persisting for less than 1 minute before disappearing.

These observations are consistent with those of Low et al. (2025) who, based on 14 hours of ground-based camera observations of 281 aircraft flights in London, reported that 73.3% of the observed contrails were short-lived (< 2 min) and formed mainly under ice-undersaturated conditions (mean RHi of 81%), 12.5% had a lifetime between 2 and 10 min (with 59% of these formed under conditions under saturation relative to ice) and 14.2% were persistent (> 10 min), with 75% formed under supersaturated conditions (mean RHi of 124%). In addition, our results indicate that contrails can form even when RHi is below 100 %, while 105 % appears to be a critical threshold beyond which contrails persist for over two hours, as observed on June 2, 2023, over Clermont-Ferrand. Furthermore, persistent contrails tend to form in warmer temperature conditions. This suggests that, in this case study, water content could play a more significant role than temperature in contrail formation and persistence.

4.6. Conclusion

In the present study, we have documented the formation and persistence of several contrails, using a complementary data set consisting of an all-sky camera, ADS-B recordings, LIDAR and ERA5 reanalysis data from ECMWF. Our results indicate that contrails primarily form under specific atmospheric conditions, notably ice supersaturation (RHi > 100%) and low temperatures (< 230 K), both of which being critical factors.
Notably, persistent contrails lasting over two hours are observed under conditions of high RHi values (up to 116 %) and temperatures below 222 K, indicating optimal conditions for their longevity. The contrails are categorized into two groups: persistent (lasting more than 2 hours) and non-persistent (lasting less than 3 minutes). Persistent contrails (C1 to C5) exhibit RHi values between 107 and 116%, temperatures ranging from 217 to 223 K, and substantial horizontal extensions (up to 1.9 ±0.32 km). These contrails are associated with twin-engine aircraft, primarily Boeing 777s, and moderate horizontal wind speeds (5 to 7 m s^{-1}).

This project has received funding from the European Union's Horizon Europe Research and innovation program under Grant Agreement No 101056885

Conversely, non-persistent contrails (C6 to C12) are characterized by less favourable atmospheric conditions, with RHi values mostly below 90 %, despite colder temperatures (near 214 K) compared to persistent contrails. These contrails are often linked to both twin- and four-engine aircraft with lower vertical speeds, which limited their development.
The study also reveals periods of undersaturation (RHi < 100 %), during which no persistent contrails formed, highlighting the critical role of environmental factors in contrail dynamics. ECMWF-ERA5 reanalysis shows that the supersaturation zone fluctuates throughout the day, with significant variations in altitude. Persistent contrails with a lifespan exceeding two hours in the camera field of view, as well as those detected above the LIDAR, enabled detailed characterization of their horizontal and vertical extensions. The horizontal extensions of these contrails have been estimated with two independent methods, one based on LIDAR observation duration and wind speed, and another based on all sky camera image analysis. They vary from 0.53 ±0.10 km and 1.60 ±0.44 km and from 0.35 ±0.14 km to 1.90 ±0.32 km with the respective methods. These observations are consistent with previous airborne and satellite studies, supporting the representativity of the case day.
To gain further insight into the microphysical properties of contrails, future studies could focus on a more detailed analysis of LIDAR signals to investigate the influence of wavelength on the depolarization and scattering of light. Such an approach would allow for a better characterization of particle size, shape, and their distribution along the plume, thereby enhancing our understanding of the microphysical processes involved and their relationship to atmospheric conditions and aircraft characteristics responsible for contrail formation.
Further processing of the all-sky camera images could improve estimates of the spatial extent of contrails. Finally, this study was based on a single study day. Extending the investigation over a longer period with more observations would allow for broader climatological conclusions. Such an extended study would significantly enrich our understanding of microphysical processes and their link with atmospheric conditions and aircraft characteristics responsible for the observed contrails. It is also important to indicate that our results are largely based on ECMWF-ERA5 meteorological analyses. While the European analyses correspond to the state of the art about the physical atmospheric descriptions in coupling numerical modelling and data assimilation, water vapor in the upper air remains critical challenges. In a future step, collocated water vapor lidar observations will also be deployed for improving our knowledge of the water vapor spatial and temporal variability.

Data availability
The datasets analysed in this study are available under DOI.

Aknowledgements
We acknowledge EARLINET and ACTRIS aerosol remote sensing teams for the scientific support, thanks to the use of the Single Calculus Chain that was essential for this study. The ERA5 reanalysis data used in this study were provided by ECMWF (https://doi.org/10.24381/cds.adbb2d47 and https://doi.org/10.24381/cds.bd0915c6) and generated using Copernicus Climate Change Service information (C3S).

Financial support
The project BECOM has received funding from the Horizon Europe research and innovation actions program under grant agreement 101056885. CO-PDD is an instrumented site of OPGC observatory and LaMP laboratory, supported by Université Clermont Auvergne (UCA), Centre

National de la Recherche Scientifique (CNRS-INSU) and Centre National d'Etudes Spatiales (CNES).

4.7. References

Baray, J.-L., Deguillaume, L., Colomb, A., Sellegri, K., Freney, E., Rose, C., Van Baelen, J., Pichon, J.-M., Picard, D., Fréville, P., Bouvier, L., Ribeiro, M., Amato, P., Banson, S., Bianco, A., Borbon, A., Bourcier, L., Bras, Y., Brigante, M., Cacault, P., Chauvigné, A., Charbouillot, T., Chaumerliac, N., Delort, A.-M., Delmotte, M., Dupuy, R., Farah, A., Febvre, G., Flossmann, A., Gourbeyre, C., Hervier, C., Hervo, M., Huret, N., Joly, M., Kazan, V., Lopez, M., Mailhot, G., Marinoni, A., Masson, O., Montoux, N., Parazols, M., Peyrin, F., Pointin, Y., Ramonet, M., Rocco, M., Sancelme, M., Sauvage, S., Schmidt, M., Tison, E., Vaïtilingom, M., Villani, P., Wang, M., Yver-Kwok, C., and Laj, P.: Cézeaux-Aulnat-Opme-Puy De Dôme: a multi-site for the long-term survey of the tropospheric composition and climate change, Atmos. Meas. Tech., 13, 3413–3445, https://doi.org/10.5194/amt-13-3413-2020, 2020.

Chauvigné, A., Jourdan, O., Schwarzenboeck, A., Gourbeyre, C., Gayet, J. F., Voigt, C., Schlager, H., Kaufmann, S., Borrmann, S., Molleker, S., Minikin, A., Jurkat, T., and Schumann, U.: Statistical analysis of contrail to cirrus evolution during the Contrail and Cirrus Experiment (CONCERT), Atmos. Chem. Phys., 18, 9803–9822, https://doi.org/10.5194/acp-18-9803-2018, 2018.

D'Amico, G., Amodeo, A., Mattis, I., Freudenthaler, V., and Pappalardo, G.: EARLINET Single Calculus Chain – technical – Part 1: Pre-processing of raw lidar data, Atmos. Meas. Tech., 9, 491–507, https://doi.org/10.5194/amt-9-491-2016, 2016.

Freudenthaler, V., Homburg, F., and Jäger, H.: Contrail observations by ground-based scanning lidar: Cross-sectional growth, Geophysical Research Letters, 22, 3501–3504, https://doi.org/10.1029/95GL03549, 1995.

Fréville, P., Montoux, N., Baray, J.-L., Chauvigné, A., Réveret, F., Hervo, M., Dionisi, D., Payen, G., and Sellegri, K.: LIDAR Developments at Clermont-Ferrand—France for Atmospheric Observation, Sensors, 15, 3041–3069, https://doi.org/10.3390/s150203041, 2015.

Gierens, K. and Brinkop, S.: Dynamical characteristics of ice supersaturated regions, Atmos. Chem. Phys., 12, 11933–11942, https://doi.org/10.5194/acp-12-11933-2012, 2012.

Han, Q., Welch, R., Chou, J., Rossow, W., and White, A.: Validation of Satellite Retrievals of Cloud Microphysics and Liquid Water Path Using Observations from FIRE, J. Atmos. Sci., 52, 4183–4195, https://doi.org/10.1175/1520-0469(1995)052<4183:VOSROC>2.0.CO;2, 1995.

Hersbach, H., Bell, B., Berrisford, P., Hirahara, S., Horányi, A., Muñoz-Sabater, J., Nicolas, J., Peubey, C., Radu, R., Schepers, D., Simmons, A., Soci, C., Abdalla, S., Abellan, X., Balsamo, G., Bechtold, P., Biavati, G., Bidlot, J., Bonavita, M., De Chiara, G., Dahlgren, P., Dee, D., Diamantakis, M., Dragani, R., Flemming, J., Forbes, R., Fuentes, M., Geer, A., Haimberger, L., Healy, S., Hogan, R. J., Hólm, E., Janisková, M., Keeley, S., Laloyaux, P., Lopez, P., Lupu, C., Radnoti, G., De Rosnay, P., Rozum, I., Vamborg, F., Villaume, S., and Thépaut, J.: The ERA5 global reanalysis, Quart J Royal Meteoro Soc, 146, 1999–2049, https://doi.org/10.1002/qj.3803, 2020.

This project has received funding from the European Union's Horizon Europe
Research and innovation program under Grant Agreement No 101056885

Heymsfield, A., Baumgardner, D., DeMott, P., Forster, P., Gierens, K., and Kärcher, B.: Contrail Microphysics, Bull. Amer. Meteor. Soc., 91, 465–472, https://doi.org/10.1175/2009BAMS2839.1, 2010.

Iwabuchi, H., Yang, P., Liou, K. N., and Minnis, P.: Physical and optical properties of persistent contrails: Climatology and interpretation, J. Geophys. Res., 117, 2011JD017020, https://doi.org/10.1029/2011JD017020, 2012.

Jensen, E. J., Toon, O. B., Kinne, S., Sachse, G. W., Anderson, B. E., Chan, K. R., Twohy, C. H., Gandrud, B., Heymsfield, A., and Miake-Lye, R. C.: Environmental conditions required for contrail formation and persistence, J. Geophys. Res., 103, 3929–3936, https://doi.org/10.1029/97JD02808, 1998.

Kärcher, B.: Formation and radiative forcing of contrail cirrus, Nat Commun, 9, 1824, https://doi.org/10.1038/s41467-018-04068-0, 2018.

Keckhut, P., Borchi, F., Bekki, S., Hauchecorne, A., and SiLaouina, M.: Cirrus Classification at Midlatitude from Systematic Lidar Observations, Journal of Applied Meteorology and Climatology, 45, 249–258, https://doi.org/10.1175/JAM2348.1, 2006.

Lee, D. S., Fahey, D. W., Skowron, A., Allen, M. R., Burkhardt, U., Chen, Q., Doherty, S. J., Freeman, S., Forster, P. M., Fuglestvedt, J., Gettelman, A., De León, R. R., Lim, L. L., Lund, M. T., Millar, R. J., Owen, B., Penner, J. E., Pitari, G., Prather, M. J., Sausen, R., and Wilcox, L. J.: The contribution of global aviation to anthropogenic climate forcing for 2000 to 2018, Atmospheric Environment, 244, 117834, https://doi.org/10.1016/j.atmosenv.2020.117834, 2021.

Lewellen, D. C. and Lewellen, W. S.: The Effects of Aircraft Wake Dynamics on Contrail Development, J. Atmos. Sci., 58, 390–406, https://doi.org/10.1175/1520-0469(2001)058<0390:TEOAWD>2.0.CO;2, 2001.

Lothon, M., Barnéoud, P., Gabella, O., Lohou, F., Derrien, S., Rondi, S., Chiriaco, M., Bastin, S., Dupont, J.-C., Haeffelin, M., Badosa, J., Pascal, N., and Montoux, N.: ELIFAN, an algorithm for the estimation of cloud cover from sky imagers, Atmos. Meas. Tech., 12, 5519–5534, https://doi.org/10.5194/amt-12-5519-2019, 2019.

Low, J., Teoh, R., Ponsonby, J., Gryspeerdt, E., Shapiro, M., and Stettler, M. E. J.: Ground-based contrail observations: comparisons with reanalysis weather data and contrail model simulations, Atmos. Meas. Tech., 18, 37–56, https://doi.org/10.5194/amt-18-37-2025, 2025.

Mandija, F., Keckhut, P., Alraddawi, D., Khaykin, S., and Sarkissian, A.: Climatology of Cirrus Clouds over Observatory of Haute-Provence (France) Using Multivariate Analyses on Lidar Profiles, Atmosphere, 15, 1261, https://doi.org/10.3390/atmos15101261, 2024.

Mannstein, H., Brömser, A., and Bugliaro, L.: Ground-based observations for the validation of contrails and cirrus detection in satellite imagery, Atmos. Meas. Tech., 3, 655–669, https://doi.org/10.5194/amt-3-655-2010, 2010.

Mattis, I., D'Amico, G., Baars, H., Amodeo, A., Madonna, F., and Iarlori, M.: EARLINET Single Calculus Chain – technical – Part 2: Calculation of optical products, Atmos. Meas. Tech., 9, 3009–3029, https://doi.org/10.5194/amt-9-3009-2016, 2016.

This project has received funding from the European Union's Horizon Europe Research and innovation program under Grant Agreement No 101056885

Meijer, V. R., Eastham, S. D., Waitz, I. A., and Barrett, S. R. H.: Contrail altitude estimation using GOES-16 ABI data and deep learning, Atmos. Meas. Tech., 17, 6145–6162, https://doi.org/10.5194/amt-17-6145-2024, 2024.

Papagiannopoulos, N., D'Amico, G., Gialitaki, A., Ajtai, N., Alados-Arboledas, L., Amodeo, A., Amiridis, V., Baars, H., Balis, D., Binietoglou, I., Comerón, A., Dionisi, D., Falconieri, A., Fréville, P., Kampouri, A., Mattis, I., Mijić, Z., Molero, F., Papayannis, A., Pappalardo, G., Rodríguez-Gómez, A., Solomos, S., and Mona, L.: An EARLINET early warning system for atmospheric aerosol aviation hazards, Atmos. Chem. Phys., 20, 10775–10789, https://doi.org/10.5194/acp-20-10775-2020, 2020.

Peyrin, F., Fréville, P., Montoux, N., and Baray, J.-L.: Original and Low-Cost ADS-B System to Fulfill Air Traffic Safety Obligations during High Power LIDAR Operation, Sensors, 23, 2899, https://doi.org/10.3390/s23062899, 2023.

Poellot, M. R., Arnott, W. P., and Hallett, J.: In situ observations of contrail microphysics and implications for their radiative impact, J. Geophys. Res., 104, 12077–12084, https://doi.org/10.1029/1999JD900109, 1999.

Rosenow, J., Hospodka, J., Lán, S., and Fricke, H.: Validation of a Contrail Life-Cycle Model in Central Europe, Sustainability, 15, 8669, https://doi.org/10.3390/su15118669, 2023.

Sanogo, S., Boucher, O., Bellouin, N., Borella, A., Wolf, K., and Rohs, S.: Variability in the properties of the distribution of the relative humidity with respect to ice: implications for contrail formation, Atmos. Chem. Phys., 24, 5495–5511, https://doi.org/10.5194/acp-24-5495-2024, 2024.

Sassen, K.: Contrail-Cirrus and Their Potential for Regional Climate Change, Bull. Amer. Meteor. Soc., 78, 1885–1903, https://doi.org/10.1175/1520-0477(1997)078<1885:CCATPF>2.0.CO;2, 1997.

Schumann, U., Hempel, R., Flentje, H., Garhammer, M., Graf, K., Kox, S., Lösslein, H., and Mayer, B.: Contrail study with ground-based cameras, Atmos. Meas. Tech., 6, 3597–3612, https://doi.org/10.5194/amt-6-3597-2013, 2013.

Schumann, U., Bugliaro, L., Dörnbrack, A., Baumann, R., and Voigt, C.: Aviation Contrail Cirrus and Radiative Forcing Over Europe During 6 Months of COVID-19, Geophysical Research Letters, 48, e2021GL092771, https://doi.org/10.1029/2021GL092771, 2021.

Singh, D. K., Sanyal, S., and Wuebbles, D. J.: Understanding the role of contrails and contrail cirrus in climate change: a global perspective, Atmos. Chem. Phys., 24, 9219–9262, https://doi.org/10.5194/acp-24-9219-2024, 2024.

Sun, J. and Roosenbrand, E.: Fast contrail estimation with OpenSky data, JOAS, 1, https://doi.org/10.59490/joas.2023.7264, 2023.

Taylor, J. R.: An introduction to error analysis: the study of uncertainties in physical measurements, 2. ed., University Science Books, Sausalito, Calif, 327 pp., 1997.

Teoh, R., Engberg, Z., Schumann, U., Voigt, C., Shapiro, M., Rohs, S., and Stettler, M. E. J.: Global aviation contrail climate effects from 2019 to 2021, Atmos. Chem. Phys., 24, 6071–6093, https://doi.org/10.5194/acp-24-6071-2024, 2024.

This project has received funding from the European Union's Horizon Europe
Research and innovation program under Grant Agreement No 101056885

Unterstrasser, S., Gierens, K., Sölch, I., and Lainer, M.: Numerical simulations of homogeneously nucleated natural cirrus and contrail-cirrus. Part 1: How different are they?, metz, 26, 621–642, https://doi.org/10.1127/metz/2016/0777, 2017.

Voigt, C., Schumann, U., Jurkat, T., Schäuble, D., Schlager, H., Petzold, A., Gayet, J.-F., Krämer, M., Schneider, J., Borrmann, S., Schmale, J., Jessberger, P., Hamburger, T., Lichtenstern, M., Scheibe, M., Gourbeyre, C., Meyer, J., Kübbeler, M., Frey, W., Kalesse, H., Butler, T., Lawrence, M. G., Holzäpfel, F., Arnold, F., Wendisch, M., Döpelheuer, A., Gottschaldt, K., Baumann, R., Zöger, M., Sölch, I., Rautenhaus, M., and Dörnbrack, A.: In-situ observations of young contrails – overview and selected results from the CONCERT campaign, Atmos. Chem. Phys., 10, 9039–9056, https://doi.org/10.5194/acp-10-9039-2010, 2010.

Voigt, C., Schumann, U., Minikin, A., Abdelmonem, A., Afchine, A., Borrmann, S., Boettcher, M., Buchholz, B., Bugliaro, L., Costa, A., Curtius, J., Dollner, M., Dörnbrack, A., Dreiling, V., Ebert, V., Ehrlich, A., Fix, A., Forster, L., Frank, F., Fütterer, D., Giez, A., Graf, K., Grooß, J.-U., Groß, S., Heimerl, K., Heinold, B., Hüneke, T., Järvinen, E., Jurkat, T., Kaufmann, S., Kenntner, M., Klingebiel, M., Klimach, T., Kohl, R., Krämer, M., Krisna, T. C., Luebke, A., Mayer, B., Mertes, S., Molleker, S., Petzold, A., Pfeilsticker, K., Port, M., Rapp, M., Reutter, P., Rolf, C., Rose, D., Sauer, D., Schäfler, A., Schlage, R., Schnaiter, M., Schneider, J., Spelten, N., Spichtinger, P., Stock, P., Walser, A., Weigel, R., Weinzierl, B., Wendisch, M., Werner, F., Wernli, H., Wirth, M., Zahn, A., Ziereis, H., and Zöger, M.: ML-CIRRUS: The Airborne Experiment on Natural Cirrus and Contrail Cirrus with the High-Altitude Long-Range Research Aircraft HALO, Bulletin of the American Meteorological Society, 98, 271–288, https://doi.org/10.1175/BAMS-D-15-00213.1, 2017.

Wandinger, U., Nicolae, D., Pappalardo, G., Mona, L., and Comerón, A.: ACTRIS and its Aerosol Remote Sensing Component, EPJ Web Conf., 237, 05003, https://doi.org/10.1051/epjconf/202023705003, 2020.

This project has received funding from the European Union's Horizon Europe Research and innovation program under Grant Agreement No 101056885

5. General conclusions of this deliverable

This deliverable consolidates results from three BeCoM milestones, each addressing different but complementary aspects of upper-tropospheric humidity and contrail research. Comparisons of satellite (MLS), reanalysis (ERA5), and radiosonde observations with Raman lidar demonstrate a persistent dry bias at cruise altitudes, both in the tropics and midlatitudes. While MLS underestimates water vapor by up to 30% above 12 km, ERA5 exhibits a systematic bias of 10–20%, partly linked to ice-supersaturation conditions. In contrast, GRUAN-processed radiosondes show the best agreement with lidar (<10% bias), confirming the sensitivity and reliability of Raman lidar as a benchmark for humidity profiling and a promising candidate for future data assimilation.

The TRACIS campaign at SIRTA further reinforced these findings through a comprehensive multi-instrument strategy, including the triple-attelage radiosounding system (M10, M20, RS41) with day and night launches. First results confirm lidar’s ability to capture upper-tropospheric humidity more accurately than other techniques, while also validating retrieval algorithms developed within BeCoM. The campaign provided a unique dataset for evaluating model biases and linking humidity variability to aviation activity in one of Europe’s busiest airspaces. Importantly, nocturnal contrail events detected during TRACIS will be analyzed in the next period to complement the daytime case studies already carried out at Clermont-Ferrand.

The case study over, Clermont-Ferrand demonstrated the value of coordinated ground-based and ancillary measurements for studying contrail formation. Persistent contrails were observed under ice-supersaturated conditions (RHi > 105%) and low temperatures (217–223 K), while non-persistent contrails occurred in drier, colder air. Horizontal and vertical geometries were quantified using lidar and all-sky camera, offering robust metrics for contrail monitoring. These preliminary results highlight the potential of such integrated approaches to constrain contrail growth mechanisms and provide valuable benchmarks for numerical models.
More case studies will be required with as far as possible different meteorological and thermodynamical conditions. The cases reported here are obtained while no natural cirrus clouds were formed and probably thermodynamic conditions during this day were close to the contrail saturation level. Even if this is a rather limited number of cases, these observations could be very valuable and can be investigated in more details by the modeling community, while a lot of information is available to constrain models or compared with numerical outputs.
These observations and conclusions about supersaturation are based on the ECMWF-ERA5 model. We have already reported a deficient some time in water vapor compared with radiosondes and lidar of around 5-10%. If this difference is confirmed, supersaturation threshold could be rather then close to 120%.

Overall, the deliverable introduces a clear progression: from identifying uncertainties in existing datasets, to improving observational capabilities through dedicated field campaigns, to applying these insights in contrail case studies. This integrated framework strengthens the scientific basis for contrail prediction and mitigation strategies and contributes to the broader BeCoM objective of reducing aviation’s climate impact.

This project has received funding from the European Union’s Horizon Europe Research and innovation program under Grant Agreement No 101056885